

AN OPTICAL ATOMIC CLOCK BASED ON FREQUENCY COMB SPECTROSCOPY

by

Seth E. Erickson

---

Copyright © Seth E. Erickson 2024

A Dissertation Submitted to the Faculty of the

JAMES C. WYANT COLLEGE OF OPTICAL SCIENCES

In Partial Fulfillment of the Requirements

For the Degree of

DOCTOR OF PHILOSOPHY

In the Graduate College

THE UNIVERSITY OF ARIZONA

2024

THE UNIVERSITY OF ARIZONA  
GRADUATE COLLEGE

As members of the Dissertation Committee, we certify that we have read the dissertation prepared by **Seth Enoch Erickson**, titled ***An Optical Atomic Clock Based on Frequency Comb Spectroscopy*** and recommend that it be accepted as fulfilling the dissertation requirement for the Degree of Doctor of Philosophy.

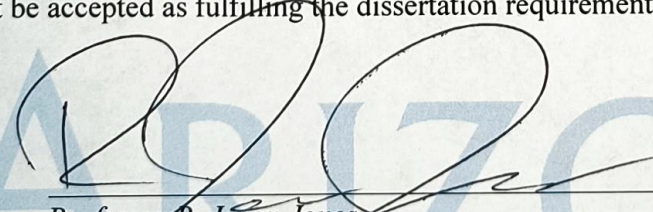
  
\_\_\_\_\_  
Professor *R. Jason Jones* Date: 2/23/2024

  
\_\_\_\_\_  
Professor *Brian P. Anderson* Date: 2/23/2024

  
\_\_\_\_\_  
Professor *Dalziel Wilson* Date: 2/23/2024

Final approval and acceptance of this dissertation is contingent upon the candidate's submission of the final copies of the dissertation to the Graduate College.

I hereby certify that I have read this dissertation prepared under my direction and recommend that it be accepted as fulfilling the dissertation requirement.

  
\_\_\_\_\_  
Professor *R. Jason Jones*  
Dissertation Committee Chair  
Wyant College of Optical Sciences Date: 2/23/2024

## ACKNOWLEDGMENTS

The efforts represented within this dissertation would not have been possible without assistance from a great many sources. First, I must thank my advisor, Professor Jason Jones, who has guided me as I have transferred across three distinct projects over the course of my graduate education. Jason has been a constant source of wisdom and has modelled the combination of competence and humility which I hope to achieve in my career.

I also extend great thanks to the many professors who have sparked my interest in physics and optics. Prof. Chad Hoyt provided me with many semesters of undergraduate research in AMO physics while I still believed I would be a mechanical engineer. Through this research experience I learned the joys (and struggles) of working with lasers and atoms. I would not be pursuing a PhD in Optical Science without his guidance, or without Prof. Richard Peterson bringing me to Prof. Hoyt's attention. Bethel University provided me with an undergraduate education which truly prepared me for my graduate work, in both the classroom and the laboratory, and which developed me as a person – for the many professors there who took a personal interest in my success, I am ever grateful. Many of the professors at University of Arizona have likewise encouraged my growth as a scientist, but I especially thank the two other members of my dissertation committee, Profs. Brian Anderson and Dalziel Wilson. Both of them have shared with me many insights into physics, research, and also the human side of science. At the Air Force Research Lab, Nathan Lemke was a wonderful teacher, supplementing my undergraduate education with useful technical experimental knowledge. He, Kyle Martin, Sean Krzyzewski, and John Elgin have been a great support as I considered the professional side of my scientific journey.

The Jones group has been a welcoming home for my graduate studies, thanks to the many wonderful students. Dylan Tooley deserves special shoutout as my lab partner for the direct comb frequency standard work that makes up the bulk of this dissertation. Without Dylan,

this effort would have taken twice as long, the end product would be half as satisfying, and my life expectancy would be significantly diminished. He has been a wonderful colleague and friend. I have had the privilege to see two generations of the Jones group; the one that trained me and the one that will succeed me. Ryan Rhoades, Reagan Weeks, and Kane Zhang formed my experimental mindset and my sense of humor. Their camaraderie and intelligence was often the salve that healed a tough week on the experiment. The scientists that have come to replace them in the group, Dylan Tooley, John McCauley, and Andrew Jarymowycz, are worthy successors, and I look forward to seeing the fruit of their careers.

The scientific effort is a human effort, so those who kept me human deserve extra thanks. Reagan Weeks, Ryan Rhoades, David Melchior, and Dylan Tooley have become dear friends who were always available for watching sumo, getting drinks, and/or eating cheese. Fr. Peter Forbes and Benjamin Miller have come alongside me to offer crucial personal and spiritual counsel through these seven years. My parents, Dean and Janice, have been a source of encouragement from my childhood to today. My son, Dorian, has increased the challenge of this work in some ways, but has brought me joy at the same time. Finally, to my wife Dawn: you have been the safe harbor in my life, a constant source of assurance, and you make me a better man every day.



## DEDICATION

*For my father Dean and my son Dorian, who have together taught me  
that fatherhood is a lifelong effort to be at once teacher and student*

## TABLE OF CONTENTS

<b>LIST OF FIGURES</b> . . . . .	9
<b>LIST OF TABLES</b> . . . . .	15
<b>ABSTRACT</b> . . . . .	16
<b>CHAPTER 1 Introduction</b> . . . . .	17
<b>1.1 Optical Atomic Clocks</b> . . . . .	17
1.1.1 <i>Introduction to Clocks</i> . . . . .	17
1.1.2 <i>Instability Analysis</i> . . . . .	19
<b>1.2 Frequency Combs</b> . . . . .	21
1.2.1 <i>Modelocked Lasers</i> . . . . .	22
1.2.2 <i>Self-Referential <math>f_{CEO}</math> Lock</i> . . . . .	24
1.2.3 <i>Frequency Comb as “gearwork”</i> . . . . .	24
<b>CHAPTER 2 Frequency Comb Spectroscopy</b> . . . . .	26
<b>2.1 Dual Comb Spectroscopy</b> . . . . .	26
2.1.1 <i>Theory</i> . . . . .	26
2.1.2 <i>Experiment</i> . . . . .	28
<b>2.2 Doppler Free Two-Photon Spectroscopy</b> . . . . .	31
2.2.1 <i>Excitation Rate</i> . . . . .	33
2.2.2 <i>fm-Spectroscopy</i> . . . . .	38
<b>2.3 Direct Comb Doppler-Free Two-Photon Spectroscopy</b> . . . . .	38
2.3.1 <i>Excitation Rate</i> . . . . .	40
2.3.2 <i>Residual Doppler Broadening</i> . . . . .	43

2.3.3	<i>Aliasing</i> . . . . .	45
<b>CHAPTER 3</b>	<b>Direct Comb Spectroscopy as an Optical Atomic Clock</b> . . . . .	51
<b>3.1</b>	<b>Advantages of a Direct Comb Reference</b> . . . . .	51
<b>3.2</b>	<b>Sources of Instability</b> . . . . .	52
3.2.1	<i>Shot Noise</i> . . . . .	52
3.2.2	<i>Intermodulation Noise</i> . . . . .	54
3.2.3	<i>Residual Amplitude Modulation</i> . . . . .	55
3.2.4	<i>Pressure Shifts</i> . . . . .	58
3.2.5	<i>ac-Stark Shift</i> . . . . .	59
3.2.6	<i>Residual Stark Shift</i> . . . . .	61
<b>3.3</b>	<b>Isotope/Transition Selection</b> . . . . .	63
<b>CHAPTER 4</b>	<b>Design Considerations and Clock Performance</b> . . . . .	65
<b>4.1</b>	<b>Design</b> . . . . .	65
4.1.1	<i>Laser systems</i> . . . . .	65
4.1.2	<i>Vapor Cell Holder Design</i> . . . . .	68
4.1.3	<i>Cold Point Control</i> . . . . .	71
4.1.4	<i>Probe Geometry</i> . . . . .	72
4.1.5	<i>Pulse Width Considerations</i> . . . . .	75
4.1.6	<i>RAM Stabilization</i> . . . . .	78
<b>4.2</b>	<b>Detection Electronics</b> . . . . .	79
<b>4.3</b>	<b>Phase Noise Measurements</b> . . . . .	81
<b>4.4</b>	<b>Stark Shift Mitigation</b> . . . . .	85
<b>4.5</b>	<b>Overall Clock Performance</b> . . . . .	88
4.5.1	<i>Transition linewidth</i> . . . . .	88
4.5.2	<i>ac-Stark shift sensitivity</i> . . . . .	89
4.5.3	<i>Instability</i> . . . . .	91
4.5.4	<i>Power Dependence of Short-Term Stability</i> . . . . .	93
4.5.5	<i>Thermal Drift</i> . . . . .	94

<b>CHAPTER 5 Conclusion</b> . . . . .	96
<b>GLOSSARY</b> . . . . .	100
<b>REFERENCES</b> . . . . .	101



## LIST OF FIGURES

1.1	Classification of various atomic clocks. RAFS: Rubidium atomic frequency standard. CSAC: Chip scale atomic clock. CBT: Cesium beam tube. H-Maser: Hydrogen Maser. cRb: Cold rubidium standards. O-RAFS: Optical RAFS. I2: Iodine molecular clock. “Direct Comb” refers to the work within this dissertation. H-Maser is an outlier, with the size and stability on the order of the cold-RF or hot-optical clocks. . . . .	18
1.2	Pedagogical model of a frequency comb . . . . .	22
2.1	Frequency domain principle of dual comb spectroscopy, adapted from [29] with permission. . . . .	27
2.2	Schematic of one mode-locked oscillator. The other oscillator is similar, with an EOM inserted between the collimator and focusing lens to enable fast feedback. . . . .	29
2.3	Broadband dual comb spectroscopy of a 4 m air path, showing water absorption around 1450 nm. . . . .	30
2.4	(a) Levels of interest for two-photon spectroscopy of $^{87}\text{Rb}$ . Squiggle-arrows represent spontaneous decay. (b) Energy levels of interest for this toy model, simplified to show relevant parameters for the calculations. . . . .	33
2.5	Populations from the density matrix math, provided an initial intensity of $1\text{E}8 \text{ W/m}^2$ . Note the vanishing population of the intermediate state (blue). . . . .	35
2.6	Steady state population of the excited state, which determines the fluorescence. (a) shows the quadratic dependence of excitation on the incident power at low probe powers. (b) shows the effect of saturation at higher probe powers (above $10^8 \text{ mW/mm}^2$ ). . . . .	37

2.7	Pedagogical picture of direct comb two photon excitation, showing the excitation by symmetric pairs of comb teeth on the left and overlap of pulses in a vapor cell on the right. . . . .	39
2.8	Spatial extent of fluorescence from pulses of different pulse bandwidths, defined as the standard deviation of the gaussian power spectrum. . . . .	41
2.9	The relative level of integrated fluorescence compared to that of a cw probe for a vapor cell of active length 5 mm (black) and 1 mm (red). Bandwidth is reported as the standard deviation of the gaussian power spectrum. . . . .	42
2.10	Fluorescence from a 75 GHz FWHM optical spectrum at different levels of second-order dispersion (GDD). Note that past $\approx 75 \text{ ps}^2$ significant power begins leaving the vapor cell (which extends from $-2.5 \rightarrow 2.5 \text{ mm}$ . . . . .	43
2.11	Fluorescence from a 75 GHz FWHM optical spectrum at different levels of second-order dispersion GDD, integrated along a 5 mm length (black) and a 10 mm length (red). Note the reduction in fluorescence for the 5 mm cell beginning at $75 \text{ ps}^2$ , in agreement with Fig. 2.10. A 10 mm vapor cell can accommodate about twice the chirp. . . . .	44
2.12	Residual Doppler broadening for gaussian input spectra of various $\Delta\nu_{FWHM}$ . . . . .	45
2.13	Stick model of the location for all hyperfine two-photon transitions between $5S_{1/2} \rightarrow 5D_{5/2}$ in rubidium 87, for location of usable frequency comb repetition rates. . . . .	46
2.14	Stick model of the location for all hyperfine two-photon transitions between $5S_{1/2} \rightarrow 5D_{5/2}$ in rubidium 87, for higher repetition rates. The significant increase in space between transitions highlights the advantage of using higher repetition rate frequency combs. . . . .	47
2.15	Stick model of the location for all hyperfine two-photon transitions between $5S_{1/2} \rightarrow 5D_{5/2}$ in both rubidium 87 and 85, for higher repetition rates. Since even isotopically enriched vapor cells may contain small amounts of undesired isotopes, this graph is a better qualifier for a suitable $f_{rep}$ . . . . .	47
2.16	Comparison between theory from Eqn. 2.19 and experiment for our 200 MHz frequency comb. . . . .	48

2.17	Comparison between theory from Eqn. 2.19 and experiment for our 250 MHz frequency comb. . . . .	49
2.18	Small amounts of rubidium 85 can be seen in both vapor cells, identified by the overlap with theoretically predicted rubidium 85 fluorescence locations (shown in red). The clock transition ( $F=2 \rightarrow 4$ ) in rubidium is at 0 MHz in both figures. . . . .	50
3.1	Comparing the SHG conversion efficiency for cw vs. comb in two waveguide periodically poled lithium niobate (PPLN) frequency doublers. The significantly longer Coevision waveguide has a better doubling efficiency than the HCP waveguide (5% vs 1%), but neither approaches the 30% doubling efficiency of a picosecond pulse in a waveguide doubler. . . . .	52
3.2	Theoretically calculated differential polarizability, in units of fractional frequency change per $\text{mW}/\text{mm}^2$ . The location of a cw two-photon transition is shown with the red dashed line, indicating a shift of $2.3 \times 10^{-13} (\text{mW}/\text{mm}^2)^{-1}$ , in agreement with [88] . . . . .	60
3.3	Demonstration of our calculations of residual Stark shift, showing a 75 GHz FWHM gaussian spectrum translating by 5.8 pm, which is approximately the change in center wavelength of our FBG for a $1^\circ\text{C}$ temperature change. . . . .	62
3.4	Residual Stark shift at various spectral bandwidths. Calculated for an incident power of 18 mW with a beam diameter of 250 $\mu\text{m}$ , realistic parameters for our experiment. . . . .	63
4.1	Fiber amplifier chain to produce enough 778 nm power to probe the two-photon transition. FBG: Fiber Bragg Grating, EDFA: Erbium-doped Fiber Amplifier, DC-EDFA: Dual-Clad EDFA, PPLN: Periodically-Poled Lithium Niobate. . . . .	66
4.2	3D model of the vapor cell holder. The shells interlock around the vapor cell to act as an integrating cylinder and provide uniform heating. The cold finger control fits over the fillstem of the vapor cell. . . . .	69

4.3	Modelling of fluorescence collection within the final vapor cell holder design. The shell was modelled as having specular, polarization independent reflectance of 92% or 54% for aluminum or mu-metal construction respectively. All other surfaces were modelled with reflectance of 92%. Collection efficiency is calculated by integrating over the irradiance profile (bottom right) measured at the PMT location. . . . .	70
4.4	Cold point out-of-loop temperature monitor. The Allan deviation shows that at times longer than 3000 s we have temperature fluctuations lower than 1 mK.	71
4.5	Possible schematics for achieving pulse overlap within the rubidium vapor cell. ISM: intensity stabilization module . . . . .	73
4.6	Two-photon spectra recorded from direct comb excitation of a miniaturized vapor cell, with AR/HR coatings depicted in Fig. 4.5b. The experimental direct-comb spectrum well <b>(b)</b> correlates to the theoretical spectrum <b>(a)</b> predicted for natural abundance rubidium, given a repetition rate of 250 MHz. The lack of isotopic enrichment and the $\approx 6$ MHz linewidths make this vapor cell unusable as a frequency reference. <b>(c)</b> shows the same vapor cell probed with a cw laser. . . . .	75
4.7	Detailed schematic of the breadboard spectroscopy setup used for the IMRA system. The Vescent setup is similar with the length between the second lens and translation stage increased to match the smaller $f_{rep}$ . ISM: intensity stabilization module. DMSP1180 and DMLP60 are dichroic mirrors which filter the fundamental 1556 and third harmonic 518 nm light out of the 778 nm probe beam. . . . .	76
4.8	Optical spectra of probe light from IMRA oscillator with three different FBGs. Spectra are shown at centered at 778.1 nm = 385.284 THz. The resolution of the OSA is 0.07 nm = 35 GHz at this wavelength. The “0.3 nm” FBG measures a FWHM at 38.6 GHz, which may be limited by the instrument resolution. . . . .	77
4.9	Setup for comparative measurements between the various fiber bragg gratings.	77



4.10	Comparative measurements between several fiber Bragg gratings, showing increasing fluorescence collection with decreasing bandwidth. (a) All FBG combinations compared to cw measurement on the same spectroscopy setup. (b) Spectra used for excitation with the 0.8 nm FBG. Distortion at the center of the normal dispersion spectrum may explain the outlier in (a). . . . .	78
4.11	RF electronics required to compare the $f_{rep}$ of our three clocks. RIO $f_{rep}$ is actually a tap from the AOSense 160 MHz frequency comb which has a comb tooth phase-locked to the RIO clock laser. All part numbers are from Mini Circuits except DET01CFC (Thorlabs) and MFC2510-1 (Microwave Filter Corp.). The electronic loop circled in blue is the regenerative divider for converting 250 MHz to 125 MHz. . . . .	79
4.12	Measurements between each pair of frequency references, all locked to a common cw reference. This measurement indicates the noise floor of the detection chain diagrammed in Fig. 4.11 . . . . .	80
4.13	Setup for measuring the frequency comb optical frequency noise . . . . .	82
4.14	Relative frequency noise for a beatnote between a RIO Planex laser and the IMRA (blue) and Vescent (orange) frequency combs. The $\beta$ -separation line (green) and level of frequency noise where intermodulation noise limits the one second allan deviation above $10^{-13}$ (magenta) are also shown. The PLL bandwidth limit this measurement to below 1 MHz; this is the source of the large peak at 1.2 MHz and the immediate drop in detected noise beyond the loop bandwidth. . . . .	84
4.15	Frequency noise on $f_{CEO}$ for each oscillator. . . . .	85
4.16	Setup for two color Stark mitigation with active balancing. EOM: electro-optic modulator, VOA: variable optical attenuator. . . . .	87
4.17	Allan deviation from attempted ac-Stark shift mitigation. The “Driven” samples had a sinusoidal modulation with a 20 s period applied to the intensity of the clock laser to simulate instability in intensity. “Mitigation Off” indicates that the mitigation laser was blocked, “Mitigation On” indicates that the mitigation laser was unblocked and the mitigation servo was locked. . . .	88

4.18	Comparative measurement of the linewidth for cw excitation (red) vs direct comb excitation (black). These data were normalized in intensity, since the direct comb excitation at 75 GHz bandwidth produces 25% fluorescence compared to cw. The frequency axis was calibrated via the spacing between the peaks of the $F=2 \rightarrow 4$ and $F=2 \rightarrow 3$ transitions. . . . .	89
4.19	Comparative measurement of the ac-Stark shift for cw excitation (red) vs direct comb excitation (black). The data are shifted up to ensure their linear fit intersects the origin. Error bars indicate the standard deviation of the frequency shift at each power level. . . . .	90
4.20	Measurement of the residual Stark shift via changing the center wavelength of the FBG by changing the FBG temperature. . . . .	91
4.21	Allan deviation comparing two direct-comb rubidium frequency standards. In black is a 5 hour selection from the longer 10 hour run (red). The five hour selection was the portion of the frequency record with the least frequency drift. This measurement is the two-clock relative instability divided by $\sqrt{2}$ to imply single clock instability. . . . .	92
4.22	Three-cornered hat measurement of the three frequency references developed.	93
4.23	Measurement of the one second fractional frequency instability vs. power, to determine the cross-over where probe power no longer limits clock stability. .	94
4.24	Measurement of fluorescence detected on a PMT, room temperature, and clock frequency during an overnight run. The correlation supports the hypothesis that the intensity of our probe is tracking the room temperature due to thermal drifts in the ISM. . . . .	95
5.1	Scan across the two-photon $5S_{1/2} \rightarrow 5D_{5/2}$ transitions in a vapor cell with natural abundance Rb. Narrow Doppler-free peaks can be seen in the experimental data (Black) on top of a Doppler-broadened background (Red). The clock transition in $^{87}\text{Rb}$ is circled in blue. The scan is too fast to resolve the hyperfine excited state splitting. . . . .	97

## LIST OF TABLES

1.1	Source of noise vs. scaling of the frequency noise power spectral density ( $S_f$ ) vs. Allan deviation ( $\sigma_y$ ) vs. modified Allan Deviation (mod $\sigma^y$ ) vs. time deviation ( $\sigma_x$ ) . . . . .	20
3.1	Table of important collisional shift parameters . . . . .	58
3.2	Table of relevant transition characteristics for calculating ac-polarizability, retrieved from [89] . . . . .	61
4.1	Dependence of inherent TIA noise at different trans-impedance gain settings. $\sigma_y$ is a two-clock allan deviation recorded at 1 s with a factor of $\sqrt{2}$ removed to imply the limit to single clock stability. . . . .	81

## ABSTRACT

Doppler free two-photon spectroscopy of  $^{87}\text{Rb}$  is a leading candidate for a portable frequency standard with instability comparable to a hydrogen maser. The required 778 nm light has been achieved through second-harmonic generation of continuous wave (cw) lasers, due to the availability of compact, narrow linewidth, fiber-coupled telecom diodes at 1556 nm. The cw laser was then compared to a frequency comb to convert the optical frequency into a radio frequency. It is alternatively possible to excite the same transition directly with a frequency comb, removing the need for the cw laser and increasing the efficiency of second-harmonic generation. Previous efforts to utilize direct comb spectroscopy as a frequency standard have shown larger instability than their cw counterparts, due in large part to residual Doppler broadening from pulses lasting less than one ps. Herein are discussed the relevant considerations to make direct comb spectroscopy perform equivalently to cw two-photon spectroscopy, most importantly, narrowly filtering the optical bandwidth. The leading sources of instability are explained and methods for compensation are implemented. Features which distinguish direct comb spectroscopy from cw two-photon spectroscopy, such as spectral aliasing, pulse overlap volume, and the residual Stark shift, are evaluated theoretically and experimentally. Direct comb spectroscopy is shown to be capable of resolving the two photon transitions with equivalent linewidth and equivalent ac-Stark shift compared to cw two-photon spectroscopy, with total fluorescence capture of up to 60%. By recording relative frequency deviations between two nearly identical direct comb clocks, instability rivaling the state-of-the-art compact optical frequency standard is shown, with fractional frequency Allan deviation at  $1.7 \times 10^{-13}$  at one second averaging down to  $3 \times 10^{-14}$  at 1000 s before drifting in longer timescales. The drift at times longer than an hour is shown to correlate with room temperature, offering some explanation for its source and solution. Efforts towards miniaturization and packaging and future directions for research are discussed.



## Chapter 1

### Introduction

#### 1.1 Optical Atomic Clocks

##### 1.1.1 Introduction to Clocks

The history of human progress has been intimately tied to the progress of timekeeping. Early calendars helped agrarian societies to anticipate the seasons, Eratosthenes used sundials to calculate the circumference of the earth, the marine chronometer made transcontinental shipping reliable. In the mid nineteenth century, a full hundred years before the adoption of the atomic basis of the SI second, Thomson and Tait predicted the atomic timekeeping revolution:

The time of vibration of a sodium particle corresponding to any one of its modes of vibration, is known to be absolutely independent of its position in the universe, and it will probably remain the same so long as the particle itself exists. The wavelength for that particular ray ... gives a perfectly invariable unit of length ... [1, §15]

The modern world is a product of atomic clocks. Most notably, global navigation satellite systems such as the Global Positioning System (GPS) are based entirely on receiving precise time information from multiple satellites in orbit. The internet and cellular networks multiplex information from millions of devices by precisely timed switching. Very-long-baseline interferometry, which enables the most precise radio telescopes, interferes signals across the globe by synchronization to atomic clocks. Quantum computers rely on precision timing to maintain fidelity in qubit rotation [2, 3].

So what is an atomic clock and why *optical* atomic clocks? A clock is nothing more than

a precision frequency standard with a way to readout the phase, i.e. an oscillator and a counter<sup>1</sup>. Turning first to the oscillator, atomic oscillators can be split into quadrants across the hot vs. cold atom and radio-frequency (RF) vs. optical divides, as shown in Fig. 1.1. All of these clock types base their stability on the principles predicted by Thomson and Tait, that atoms of the same isotope are fundamentally indistinguishable and *mostly* insensitive to their environment. § 3.2 of this dissertation is an evaluation of the breakdown of that insensitivity. A pendulum, spring, or quartz based oscillator are all designed by an engineer to tick at a given frequency, imperfectly manufactured to approximate that frequency, then set in an environment that changes the frequency – an atomic oscillator removes the design and manufacturing errors, such that the only source of error is the environment.

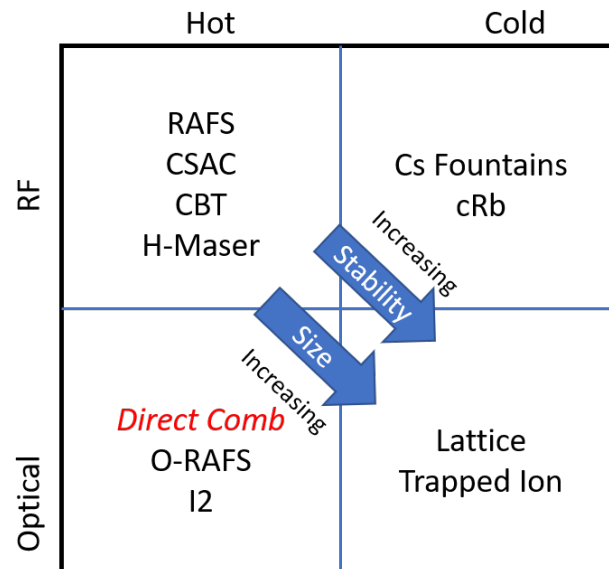


**Figure 1.1:** Classification of various atomic clocks. RAFS: Rubidium atomic frequency standard. CSAC: Chip scale atomic clock. CBT: Cesium beam tube. H-Maser: Hydrogen Maser. cRb: Cold rubidium standards. O-RAFS: Optical RAFS. I2: Iodine molecular clock. “Direct Comb” refers to the work within this dissertation. H-Maser is an outlier, with the size and stability on the order of the cold-RF or hot-optical clocks.

Until very recently, a consumer who wished to purchase frequency stability only had options in the hot-RF portion of Fig. 1.1. For many applications, GPS time, based on RAFS, currently suffices. For applications that needed more precision, the options were a CSAC or CBT, with one second fractional frequency instabilities about  $10^{-10}$  and  $10^{-11}$ , or the

<sup>1</sup>see note in the glossary if you think this describes a frequency reference and not a “clock”

significantly larger and more expensive hydrogen maser, with instability  $< 10^{-13}$  [4]. Much progress has been made in the cold atom/ion optical clock field, where the best instability performance ( $10^{-17}$ ) is possible [5, 6], but these are still prohibitively complex and large for most applications. The past three years have seen many technologies in the cold-RF or hot-optical quadrants come to market, including Vector Atomic’s iodine clock, Infleqtion’s optical rubidium clock, and Spectra Dynamics’ cold rubidium clock. This generation of standards offers maser level stability for applications where maser level cost/complexity was previously prohibitive.

While this new generation of atomic clocks expands many potential applications for precision time-keeping, there is need for further miniaturization if optical atomic clocks are to truly become ubiquitous frequency standards. This dissertation describes our work on one technique (direct comb two-photon spectroscopy) to achieve further miniaturization of optical rubidium clocks without sacrificing stability. To understand how we arrived at this technique, it is worthwhile to better understand how to quantify clock instability.

### 1.1.2 Instability Analysis

The frequency of an oscillator can be characterized as some center frequency with a phase variance thereabout:  $f = f_{center} + \frac{1}{2\pi} \frac{d\phi}{dt}$ . It is often more illuminating to consider fractional frequency variations

$$y_{n,\tau} = \frac{f_{avg}[t_0 + n\tau] - f_{t_0}}{f_{t_0}}.$$

Here  $n$  is a natural number,  $\tau$  is averaging time, and  $f_{avg} = \frac{1}{\tau} \int_{t_0+(n-1)\tau}^{t_0+n\tau} f[t]dt$ . This quantity tells proportionately how much the frequency has changed from some  $f_{t_0}$ . The field of precision time-keeping generally presents the statistics on these fractional frequency variations through the two-sample Allan deviation, defined thus [7]:

$$\sigma_y[\tau] = \sqrt{\frac{1}{2} \langle (y_{n+1,\tau} - y_{n,\tau})^2 \rangle_n}.$$

The Allan deviation and its variants are powerful tools for analyzing sources of instability in an oscillator. For time varying systematic shifts in the clock frequency with a regular

period, this shift will show up in the Allan variance at the  $\tau$  corresponding to half its period. For common noise sources, the power of Allan variance change reveals the nature of the noise source, with white frequency noise averaging down like  $\sigma(\tau) \propto 1/\sqrt{\tau}$  (see Table 1.1).

Noise Type	$S_f \propto f^?$	$\sigma_y \propto \tau^?$	mod $\sigma_y \propto \tau^?$	$\sigma_x \propto \tau^?$
White Phase Noise	2	-1	-3/2	-1/2
Flicker Phase Noise	1	-1	-1	0
White Frequency Noise	0	-1/2	-1/2	1/2
Flicker Frequency Noise	-1	0	0	1
Frequency Random Walk	-2	1/2	1/2	3/2

**Table 1.1:** Source of noise vs. scaling of the frequency noise power spectral density ( $S_f$ ) vs. Allan deviation ( $\sigma_y$ ) vs. modified Allan Deviation (mod  $\sigma^y$ ) vs. time deviation ( $\sigma_x$ )

Often, an oscillator alone does not provide the desired level of instability; thus the oscillator is generally locked to some external resonance. An oscillator tightly locked to a resonance has a fundamental instability limit set by

$$\sigma_y(\tau) \geq \frac{1}{Q \times \text{SNR} \times \sqrt{\tau}}, \quad (1.1)$$

where  $Q = f_0/\Delta f_{FWHM}$  is the “quality factor” of a reference with center frequency  $f_0$  and half-width at half-max linewidth  $\Delta f_{FWHM}$  and SNR is the signal to noise ratio of detecting this resonance. The factor of  $1/\text{SNR}$  reflects that one can split the resonant linewidth by the SNR, resulting in a reference with a higher effective  $Q$ .

In order to reach small ( $< 10^{-13}$ ) fractional frequency stability in a reasonable time, one must select a reference with high  $Q \times \text{SNR}$ . With optical resonances in  $10^{15}$  Hz, possible linewidths below 1 Hz, and the potential for high SNR detection schemes, it is clear why atoms are used as the reference for the most stable clocks in the world. However, as these clocks generally rely on the energy of valence electrons (pending the discovery of the Thorium nuclear clock), these transitions are sensitive to environmental fluctuations, meaning that small changes in temperature, magnetic field, electric field, etc. quickly limit clock stability. These effects, their relative effect on clock stability, and remedies will be explored in § 3.2.

A laser properly locked to a high  $Q \times \text{SNR}$  reference such that it has low  $\sigma_y(\tau)$  is of limited utility as a clock without some way to convert the optical frequencies ( $10^{14} - 10^{15}$  Hz) into frequencies that electronics can easily count ( $< 100$  GHz). This was once a daunting task



requiring a heroic experimental effort, using a ladder of progressively lower frequency lasers, each with its higher harmonics phase-locked to the rung above [8]. With the advent of the optical frequency comb, the conversion of optical to RF has become trivial.

## 1.2 Frequency Combs

A frequency comb is a laser with coherent light at multiple frequencies  $\nu_n$  defined by the characteristic equation:

$$\nu_n = f_{CEO} + n \times f_{rep} \quad (1.2)$$

where  $f_{ceo}$  is referred to as the carrier-envelope offset frequency and  $f_{rep}$  as the repetition rate. Considered more carefully, this means that the electric field from this laser is such:

$$\tilde{E}(\nu) = \tilde{A}(\nu) \times \sum_m \delta(\nu - m f_{rep} - f_{CEO}), \quad (1.3)$$

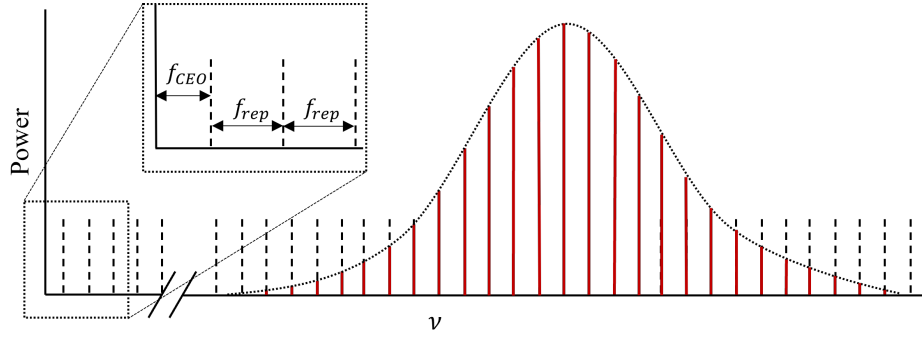
with  $\tilde{A}$  being the spectral envelope of the frequency comb, and the sum of dirac-deltas representing infinitesimally narrow spectral features at the frequencies from Eqn. 1.2. These narrow features are referred to as the ‘‘comb-teeth’’ of the frequency comb. While the comb-teeth of any real frequency comb can never truly be infinitesimally narrow, well stabilized frequency combs have shown comb-tooth relative linewidths below 3  $\mu\text{Hz}$  [9]. Since these negligible linewidths are achievable through control of only the two degrees-of-freedom ( $f_{CEO}$  and  $f_{rep}$ ), it stands to reason that less stabilized frequency combs can be considered as a dirac comb with noise summed onto these two degrees-of-freedom [10].

It is then useful to consider what this frequency comb looks like in time. The frequency-domain dirac comb of repetition rate  $f_{rep}$  Fourier transforms to a time-domain dirac comb of period  $1/f_{rep} = \tau_{rep}$  [11, §10]. Using the convolution theorem of Fourier transforms,

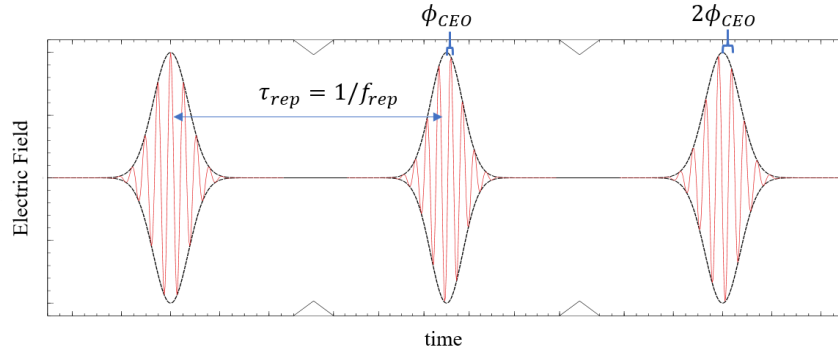
$$E(t) = A(t) * e^{i2\pi f_{CEO}t} \sum_m \delta(t - m\tau_{rep}), \quad (1.4)$$

where  $A(t) = \int_{-\infty}^{\infty} \tilde{A}(\nu) e^{-i2\pi\nu t} d\nu$  describes a pulse which is replicated by the dirac comb into a series of pulses which repeats at period  $\tau_{rep}$ . Since  $\tilde{A}(\nu)$  is centered at some optical frequency  $\nu_c$ ,  $A(t)$  will have a carrier frequency at that same  $\nu_c$ . The term  $e^{i2\pi f_{CEO}t}$  represents

that between two successive pulses, the phase of the carrier frequency slips by a phase  $\phi_{CEO} = 2\pi f_{CEO}\tau_{rep}$ .



(a) Frequency-domain of a frequency comb



(b) Time-domain picture of a frequency comb

**Figure 1.2:** Pedagogical model of a frequency comb

### 1.2.1 Modelocked Lasers

Now that the basic principles of frequency combs are established, it does well to ask “how may one generate such a frequency comb?” There are many methods for producing a frequency comb, including but not limited to external electro-optic modulation [12, 13], internal amplitude or frequency modulation active mode locking [14, §12.9-10], and Kerr microcombs [15]. For the scope of this dissertation, all of the frequency combs are based on passive, saturable absorber based mode locking. Understanding the saturable absorber mode locked laser begins most naturally from the following thought: “Since a frequency comb is equivalent to a series of ultrashort pulses in time, generating a series of regular ultrashort pulses means that I have generated a frequency comb.”

A saturable absorber mode locked laser generates this series of ultrashort pulses through an interplay between the losses of a saturable absorber within a cavity and the natural selection towards low-loss operation of a laser. A saturable absorber is any element within the laser cavity which produces more loss for low intensity light than for high intensity. This can be generated through real absorbers (e.g. carbon-nanotubes or semiconductor saturable absorber mirrors (SESAMs)) or through nonlinearities which result in rejection of light from the laser cavity (e.g. nonlinear polarization evolution or nonlinear optical/amplifying loop mirrors (NOLM/NALM)). Laser light is the result of a buildup of radiation from many round-trips within the cavity; thus on every encounter with a saturable absorber, high intensity pulses are absorbed less than continuous wave (cw) light, with the lowest loss operation achieved via all of the light in the cavity forming a single, short pulse.

This short pulse then circulates that cavity with a regular round-trip repetition period  $\tau_{rep}$ , with a small percentage leaking out of the output coupler each round-trip. On each round-trip, the carrier wave and the pulse may slip away from each other, as a medium with frequency dependent index of refraction  $n(\omega)$  has phase velocity  $c/n(\omega_c)$  and the group velocity  $c/(n(\omega_c) + \omega_c \frac{dn}{d\omega})$  which are not necessarily the same; this is the origin of  $f_{CEO}$ . Hence,  $f_{CEO}$  can be controlled by any mechanism that changes the round-trip dispersion, such as the distance between an intercavity grating pair or, as is common in fiber lasers, the pump power. The pump power changes the round-trip dispersion through a complicated interplay of nonlinear dispersion and spectral shifts [16], but the result is that pump power is an effective actuator for controlling  $f_{CEO}$ .

Control of  $f_{rep}$  is most readily achieved by changes to the cavity round-trip group optical path length  $OPL$ , since  $f_{rep} = c/OPL$ . This can be controlled via piezo-electric (PZT) fiber stretchers, cavity mirror/SESAM placed on a PZT, and/or an intercavity electro-optic modulator (EOM); often multiple of these are combined to achieve fast locks with large slow-time range. In reality, feeding back to either an  $f_{CEO}$  or  $f_{rep}$  actuator has some effect on both degrees of freedom – this is known as the “elastic-tape model” [17], where each actuator stretches the comb modes about a given frequency  $\nu_{fix}$ . A good  $f_{rep}$  actuator has  $\nu_{fix}^{rep} \approx 0$  Hz and a good  $f_{CEO}$  actuator has  $\nu_{fix}^{CEO} \gg \nu_{fix}^{rep}$ ; cavity length and pump current satisfy this respectively.

In order to feed back to these two degrees of freedom, first they must be detected. We will first discuss  $f_{CEO}$  detection and then  $f_{rep}$  detection.

### 1.2.2 Self-Referential $f_{CEO}$ Lock

Although mode-locking was achieved in the mid-1960s [18, 19], the role of  $f_{CEO}$  was not fully appreciated until several decades later [20, 21]. There are several ways to measure  $f_{CEO}$ , but for our purposes we will consider a self-referential “ $f$  to  $2f$ ” phase lock [22]. Consider an “octave-spanning” frequency comb, i.e. a comb with significant power in modes  $\nu_n = f_{ceo} + n \times f_{rep}$  and  $\nu_{2n} = f_{ceo} + 2n \times f_{rep}$ . Such an octave-spanning frequency comb is most often generated via propagation of an amplified ultrashort pulse through a length of highly non-linear fiber, letting self-phase modulation and four-wave mixing stretch the spectral envelope. If the comb tooth at  $\nu_n$  is frequency doubled through second harmonic generation, it then has frequency  $2\nu_n = 2f_{ceo} + 2n \times f_{rep}$ . By spatially overlapping this comb tooth with  $\nu_{2n}$  on a detector, the detected intensity has frequency  $2\nu_n - \nu_{2n} = 2(f_{ceo} + n \times f_{rep}) - (f_{ceo} + 2n \times f_{rep}) = f_{ceo}$ .

This RF must then be phase stabilized to a stable RF reference. In recent years, FPGA-based offset frequency locks have become prevalent [23]. The software that we used for our  $f_{ceo}$  locking is available here (<https://github.com/jddes/Frequency-comb-DPLL>). These FPGA frequency locks benefit from the ability to unwrap phase and track quick deviations with amplitude  $\gg \pi$ , meaning that even a broad  $f_{CEO}$  beatnote can be phase stabilized without dividing the frequency down and losing phase discriminant slope.

### 1.2.3 Frequency Comb as “gearwork”

When considering how to stabilize  $f_{rep}$ , we arrive at the reason that frequency combs are useful in the atomic clock context; frequency combs can be used as gearwork for converting optical frequencies to radio frequencies. If an optical frequency  $\nu_{clock}$  is known very well (to within noise deviations  $\delta\nu_{clock}$ ), it would make a low instability clock, but it is only useful for most clock applications if it can be losslessly downconverted into a radio-frequency  $f_{clock}$ . Consider a frequency comb with  $f_{CEO}$  self-referentially locked as described above, with some noise  $\delta f_{CEO}$ . By phase locking the beatnote between the stable  $\nu_{clock}$  and a given comb tooth

$\nu_n$  to some beat frequency  $f_{beat}$ , the characteristic comb equation (1.2) can be inverted:

$$\nu_n = n \times f_{rep} + f_{CEO} + \delta f_{CEO} = \nu_{clock} + \delta \nu_{clock} + f_{beat} \rightarrow \quad (1.5)$$

$$\rightarrow f_{rep} = \frac{\nu_{clock} + \delta \nu_{clock} + f_{beat} - f_{CEO} - \delta f_{CEO}}{n}. \quad (1.6)$$

Now  $f_{rep}$ , which is a radio frequency easily measured by simply shining the pulse train onto a photodetector, is linked directly to the optical  $\nu_{clock}$ , and the uncertainty is divided by the same factor as the clock frequency. In most cases,  $\delta f_{CEO} \ll \delta \nu_{clock}$ , as it is generally trivial to stabilize  $f_{CEO}$  to less than 1 mHz RMS frequency fluctuations, whereas comparable stabilization of  $\nu_{clock}$  would imply an optical  $\sigma_y \approx 1 \times 10^{-17}$ , which is near state-of-the-art. Given  $\delta f_{CEO} \ll \delta \nu_{clock}$ , the fractional frequency instability on  $f_{rep}$  is the same fractional frequency instability as that on  $\nu_{clock}$  and  $f_{rep}$  is therefore a coherent division of  $\nu_{clock}$ .

## Chapter 2

### Frequency Comb Spectroscopy

#### 2.1 Dual Comb Spectroscopy

The broadband, directional, coherent light from a frequency comb is very appealing as a source for spectroscopy. Indeed, much work has been done using traditional spectroscopy (i.e. using a grating to resolve wavelengths) but with a frequency comb as a source [24, 25]. While this uses the broad bandwidth and directionality of a frequency comb effectively, these techniques are limited by the resolution of a given grating. Meanwhile, the frequency comb is only limited in resolution by comb tooth linewidth, which can be sub-Hertz for a well stabilized frequency comb.

How can one recover the incredible resolution of a frequency comb? One solution is dual-comb spectroscopy [26–28]. Dual-comb spectroscopy (DCS) is a technique by which one may convert every optical comb-tooth into a representative comb tooth in the RF domain. This is done by heterodyne detection of two frequency combs with slightly different  $f_{rep}$ .

##### 2.1.1 Theory

Consider two frequency combs with  $f_{CEO,1(2)}$  and  $f_{rep,1(2)}$ , where  $f_{rep,2} = f_{rep,1} + \Delta f_{rep}$ , and let them possess a mutual comb tooth such that  $\nu_{m,1} = \nu_{n,2}$ . The next comb tooth of increasing frequency will be such that the difference of the frequencies is  $\nu_{n+1,2} - \nu_{m+1,1} = \Delta f_{rep}$ . Indeed, any pair of comb teeth  $\nu_{m+x,1}$  and  $\nu_{n+x,2}$  will have a difference of frequencies  $= x\Delta f_{rep}$ . When these two frequency combs are combined on a photodetector, each pair of comb teeth will generate a beatnote detected as a voltage oscillating at the difference frequency of the comb teeth. Hence, every optical comb tooth will be converted to a unique RF comb tooth with amplitude set by the fields of the corresponding teeth  $V(x\Delta f_{rep}) \propto \tilde{E}_1(\nu_{m+x,1})\tilde{E}_2(\nu_{n+x,2})$ ,

where  $\tilde{E}_{1(2)}$  is the electric field amplitude from frequency comb one or two (see Fig. 2.1). This RF spectrum is thus another frequency comb, down-converted from the optical domain into a domain where digital electronics can directly track. Importantly, absorption of comb teeth in either frequency comb results in corresponding absorption features in this RF comb.

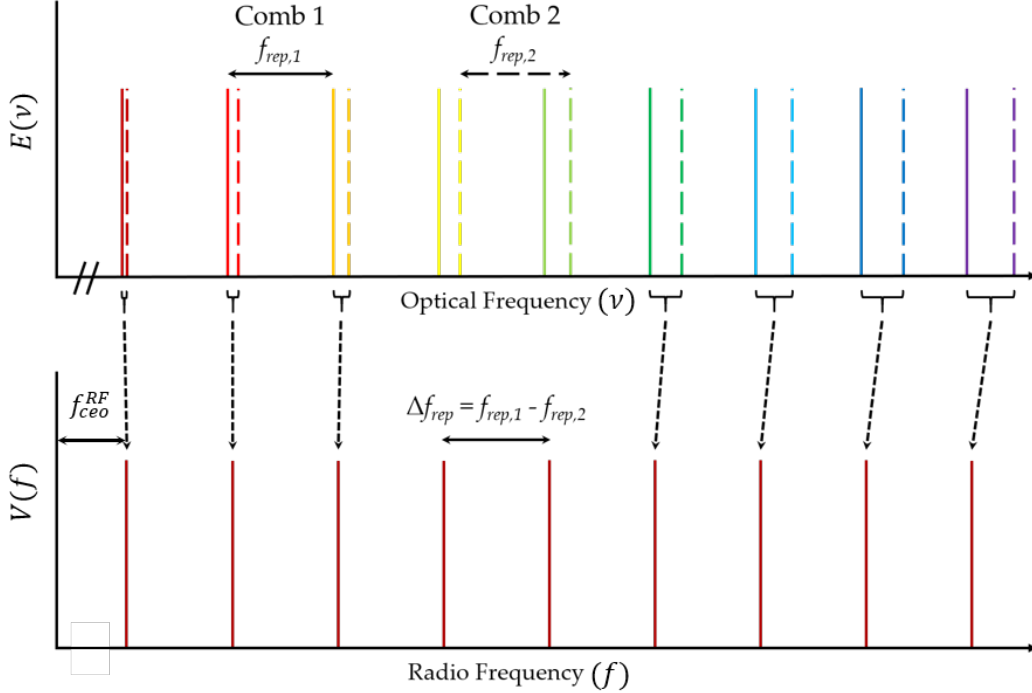


**Figure 2.1:** Frequency domain principle of dual comb spectroscopy, adapted from [29] with permission.

In the time domain, the difference in  $f_{rep}$  between the two frequency combs means that the ultrashort optical pulses walk across each other, with a different pulse-to-pulse delay when each pulse pair arrives. Since optical detectors have response time  $\tau_d$  much longer than the width of the comb pulses, the detector gives a voltage proportional to the time averaged intensity over each pulse pair. The timescale of detector response  $\tau$  is proportional to the pulse-to-pulse delay and the voltage is proportional to the integral  $\int |E_1(t)E_2(t)|^2 dt = \int (|E_1|^2 + |E_2|^2) dt + \int (E_1(t)E_2^*(t) + c.c.) dt$  over a given pulse pair — this detected signal is then a cross-correlation between the frequency comb pulses, known as an interferogram. The convolution theorem of Fourier transforms is that  $f(t) * g(t) = \mathcal{F}^{-1}[\tilde{F}(\nu)\tilde{G}(\nu)]$ ; therefore, taking the Fourier transform of the cross-correlation signal between the two combs yields

the spectrum  $\tilde{E}_1(\nu)\tilde{E}_2^*(\nu) + c.c.$ , scaled by the conversion factor between  $\tau$  and the pulse-to-pulse delay. This scaling factor is  $\frac{f_{rep}}{\Delta f_{rep}}$ , such that an optical frequency scales down to a radio frequency. This time domain picture is similar to the description of Fourier transform spectroscopy, replacing the moving interferometer arm with an auto-scanning pulse delay.

### 2.1.2 Experiment

DCS requires two frequency combs with similar  $f_{rep}$ . There are many methods of generating these two frequency combs – one of the most versatile, compact, and portable methods is the erbium fiber frequency comb. The availability of both normal and anomalous group delay dispersion at the center wavelength of erbium fiber lasers (1550 nm) allows for the construction of all-fiber or nearly all-fiber oscillators. Such lasers can consequently have very small footprint [30] and impressive ruggedness [31]. For use in the experiments described here, I constructed two mode-locked oscillators based on the design from Ref. [30]; the schematic of our version, constructed completely from commercial, off-the-shelf components, is shown in Fig. 2.2. The normal dispersion of the erbium doped fiber partially compensates the anomalous dispersion of the PM1550 passive fiber, leaving the cavity slightly ( $\approx -12,000$  fs<sup>2</sup> per round-trip) anomalously dispersive, leaving this cavity in the soliton regime. This laser is modelocked through a commercially available SESAM (SAM-1550-17-1.5ps-1.3-0). The oscillator consists of entirely polarization maintaining fiber and includes a small PZT behind the SESAM for fast corrections to  $f_{rep}$ , a longer PZT in the translation stage for the collimator for slower  $f_{rep}$  feedback. One comb also included an EOM in the freespace section for even faster corrections to  $f_{rep}$ .

The output of each oscillator was sent partly to an optical beatnote setup (see Ref. [29, p. 2.2.1]) and partly to an erbium doped fiber amplifier (EDFA). The beatnote setup consists of combining each comb with the light from an unstabilized RIO at 1562 nm to generate a beatnote on a photodetector. The first comb had its beatnote stabilized with a Red Pitaya optical phase locked loop [32]. The other comb had its beatnote mixed with the first beatnote and the resulting difference frequency was stabilized with the Red Pitaya. This mixing effectively removes any noise from the RIO and establishes phase coherence between the two frequency combs.



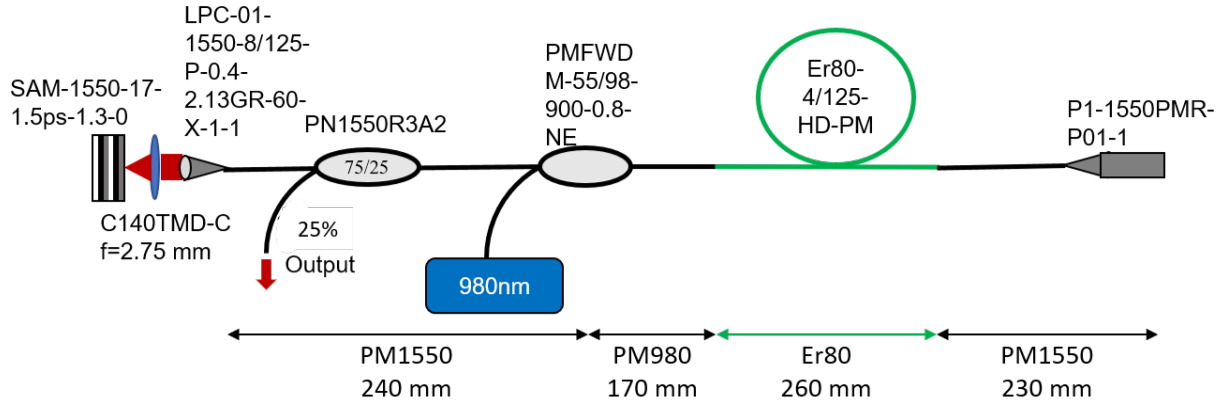


**Figure 2.2:** Schematic of one mode-locked oscillator. The other oscillator is similar, with an EOM inserted between the collimator and focusing lens to enable fast feedback.

The other portion of the oscillator output went to an EDFA constructed from Er80-4/125-HD-PM fiber, normally chirping the pulses and largely avoiding potential nonlinear pulse evolution. The pulses were then recompressed using an appropriate length of PM1550, before being spectrally broadened in 100 mm of highly nonlinear fiber. While the oscillator starts with a 10 dB bandwidth of  $\approx 15$  nm, the spectrally broadened comb stretches from 1300 nm past 1700 nm. This broad output is then coupled into free-space.

Demonstrating the broadband potential for DCS, Fig. 2.3 shows the dual-comb spectrum obtained at the output of the fiber (black) compared to the spectrum after propagating  $\approx 4$  m across the lab (red). Absorption from water vapor in the air can be seen in the circled portion of the spectrum. While this broad bandwidth measurement shows some of the potential of dual comb spectroscopy, most measurements only require a small portion of this bandwidth, and the SNR of a dual comb measurement decreases as the inverse of the number of comb teeth [33], so most experiments utilize narrow spectral filtering about the spectral regions of interest.

Another important feature of dual comb spectroscopy is its time resolution. Since the interferogram contains information about all of the frequency comb colors, and the inteferograms repeat every  $1/\Delta f_{rep}$ , the time required to take a spectrum limited in resolution by the frequency comb  $f_{rep}$  is just  $1/\Delta f_{rep}$ .  $\Delta f_{rep}$  is limited by the desired spectral bandwidth  $\Delta\nu$ , since a the optical spectrum is down-converted to an RF spectrum of bandwidth

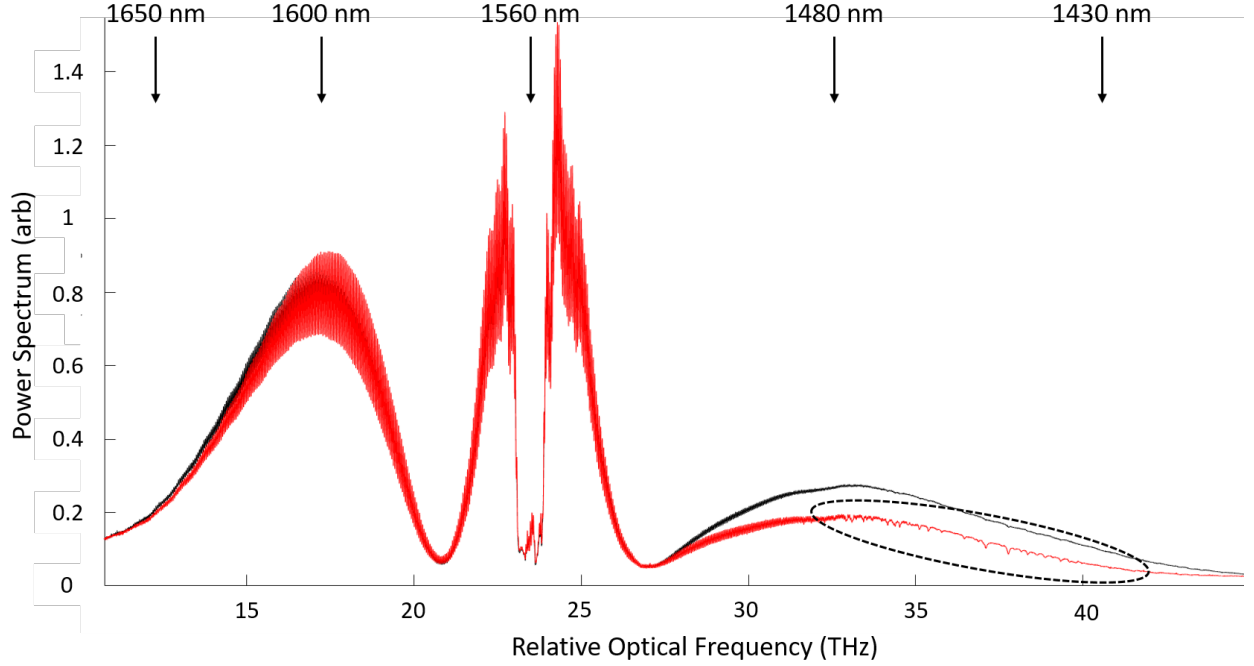


**Figure 2.3:** Broadband dual comb spectroscopy of a 4 m air path, showing water absorption around 1450 nm.

$$\Delta f = \frac{\Delta f_{rep}}{f_{rep}} \Delta \nu. \quad (2.1)$$

Given  $\Delta f^{max} = f_{rep}/2$ , the Nyquist frequency given the discrete sampling of the frequency comb at  $f_{rep}$ ,

$$\Delta f_{rep}^{max} = \frac{f_{rep}^2}{2\Delta \nu}. \quad (2.2)$$

For the realistic parameters  $\Delta \nu = 5$  THz and  $f_{rep} = 100$  MHz, this means it takes 1 ms to record a comb-resolved spectrum. If one instead had an  $f_{rep} = 1$  GHz, it would only take 10  $\mu$ s to record a comb-resolved measurement (but a comb-resolved measurement for this comb is 10x worse resolution). If one desires better time resolution, it is possible to apodize the interferogram and trade spectral resolution for time resolution [29, §1.4.2]. Alternatively, novel techniques may enable even faster time resolution of repeatable phenomena, analogous to step-scan FTS [34].

This fast spectral acquisition time makes DCS ideal for studying dynamic spectral en-

vironments such as laser produced plasmas (LPPs) [29, 35]. By passing the comb pulses through a laser produced plasma before interfering them on a balanced detector, absorption spectra from the hot atoms and ions in the ablation plume can be detected. This is useful for determining elemental and isotopic ratios within a solid sample [36]. Additionally, DCS of LPPs has enabled temperature measurements of the LPPs [37] and oscillator strengths of previously unmapped transitions [38]. While single-shot measurements are of some use, averaging over multiple interferograms can improve the signal-to-noise of these measurements — here that means averaging over many ablation events. The ablation pulses must then be triggered off of the interferogram such that the measurement occurs at the same delay after each ablation. We accomplish this via timing code running on a field programmable gate array (FPGA) as described in Ref. [29, §2.4]. Using the system for DCS of LPPs which I constructed, my colleagues were able to study the molecular formation of CeO within an ablation plume [39].

While DCS is a versatile spectroscopic method for studying atomic vapors and plasmas, these vapors and plasmas limit the measurement resolution via Doppler broadening. A lot of questions can be answered from these Doppler broadened spectra, but there are other questions which will require more resolution. There are some techniques for sub-Doppler DCS [40, 41], but in general studying structure below the Doppler width will require moving away from DCS onto other techniques, such as saturated absorption spectroscopy or Doppler free two-photon spectroscopy.

## 2.2 Doppler Free Two-Photon Spectroscopy

Consider an atom moving with velocity  $\vec{v}$  within an electric field oscillating with angular frequency  $\omega$  in the lab frame. Within the atomic frame of reference, the light has an apparent frequency (from the first order Doppler shift):

$$\omega' = \omega \left( 1 - \frac{\vec{v} \cdot \hat{k}}{c} \right), \quad (2.3)$$

where  $\hat{k}$  is the unit vector in the propagation direction of the light field. Since atoms in a hot vapor have a velocity distribution given by Maxwell-Boltzmann statistics, light on a

transition which is narrow in rest-atoms will interact with this distribution of atoms to have lineshape [14]:

$$S(\omega) = \frac{c}{\omega_0} \sqrt{\frac{m}{2\pi k_B T}} e^{-\frac{mc^2(\omega-\omega_0)^2}{2k_B T \omega_0^2}}. \quad (2.4)$$

This Doppler broadening virtually eliminates the high  $Q$  of atomic references, resulting in hundreds of MHz to GHz linewidths on optical transitions,  $Q \approx 10^3 - 10^4$ . Commonly, this is solved by either cooling the atoms or creating well collimated atomic beams. While these techniques allow state-of-the-art precision, they are both prohibitively complex for many field applications.

A different approach to removing Doppler broadening is known as Doppler free two-photon spectroscopy. If a two-photon transition is probed with two counter-propagating lasers, there is a certain probability of excitation driven by one photon of each laser (this excitation rate is derived in §2.2.1). In the case of both lasers sharing the same frequency (the degenerate case), the Doppler shift on one photon is opposite the Doppler shift from the counter-propagating photon (Eqn. 2.3), regardless of any atom's  $\vec{v}$ . Thus, the sum frequency is the same for any  $\vec{v}$ , and the atoms are excited only if the laser has frequency equal to half the energy separation of the transition, and Doppler broadening has been removed without laser cooling. This is distinct from saturated absorption spectroscopy, where Doppler broadening is removed by selecting only one velocity class; in Doppler free two-photon spectroscopy, all velocities contribute the signal.

This technique was first suggested in 1970 [42] and first observed in 1974 [43, 44] in sodium vapor. It was quickly extended to hydrogen [45] spectroscopy, where it led to orders of magnitude improvement to the measured Rydberg constant and Lamb shift [46]. Other early work utilized Doppler free two-photon spectroscopy to study Rydberg transitions [47], positronium [48], and muonium [49].

The particular two-photon transition of interest for this dissertation is the  $^{87}\text{Rb } 5\text{S}_{1/2} \rightarrow 5\text{D}_{5/2} \text{ F=2} \rightarrow 4$  transition. This transition has a few notable features: it has an intermediate state ( $5\text{P}_{3/2}$ ) near resonant with the half-energy separation, and its wavelength (778 nm) can be conveniently generated by second harmonic generation of a telecom 1556 nm source. The

relevant energy levels are diagrammed in Fig. 2.4a. This transition was first characterized in 1993 [50] and has been considered as a potential optical frequency reference since 1998 [51], with much recent promise [52–54]. The mathematics for the rest of this section are left general, but certain steps will reference this particular transition to inform simplifications.

### 2.2.1 Excitation Rate

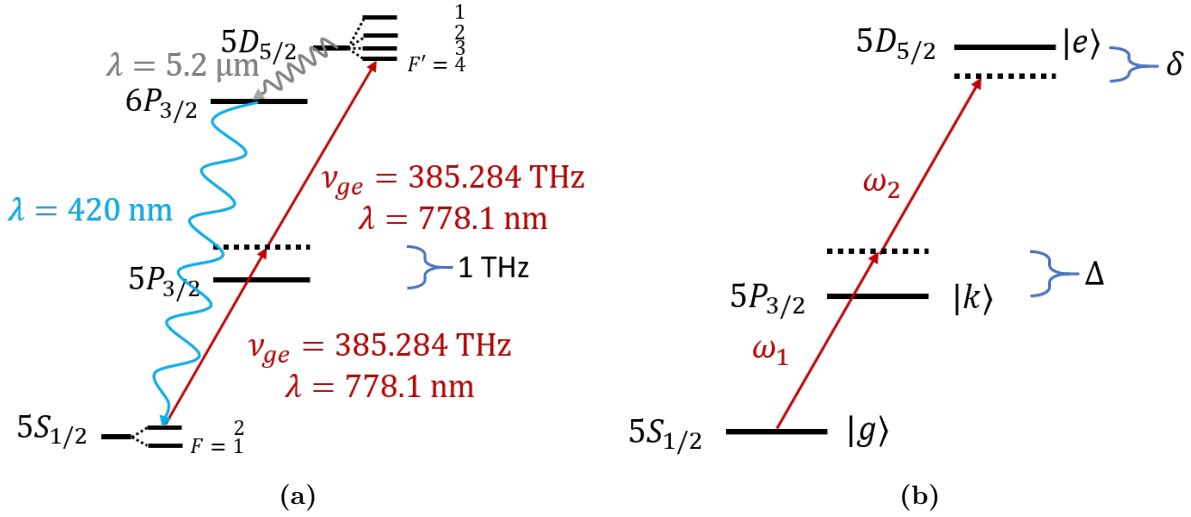


**Figure 2.4:** (a) Levels of interest for two-photon spectroscopy of  $^{87}\text{Rb}$ . Squiggle-arrows represent spontaneous decay. (b) Energy levels of interest for this toy model, simplified to show relevant parameters for the calculations.

Consider an atom with an energy level structure like that diagrammed in Fig. 2.4b. If this atom is in two optical fields  $E_{1(2)} = |E_{1(2)}|e^{i\phi_{1(2)}}(e^{i\omega_{1(2)}t} + e^{-i\omega_{1(2)}t})/2$ . The dipole interaction gives

$$\hat{H} = \hat{H}_0 + e \hat{d} \cdot \vec{E}.$$

For simplicity, we will consider  $\omega_1$  to connect states  $|g\rangle \rightarrow |k\rangle$  and  $\omega_2$  to connect  $|k\rangle \rightarrow |e\rangle$ .

Our system Hamiltonian then becomes

$$\frac{\hat{H}}{\hbar} = \begin{pmatrix} 0 & \chi_1(t) & 0 \\ \chi_1^*(t) & \omega_{gk} & \chi_2(t) \\ 0 & \chi_2^*(t) & \omega_{ge} \end{pmatrix} \quad (2.5)$$

where

$$\begin{aligned}\chi_1(t) &= \langle k|\hat{d}|g\rangle \frac{|E_1|}{\hbar} e^{i\phi_1} \frac{e^{i\omega_1 t} + e^{-i\omega_1 t}}{2} = \chi_1 \frac{e^{i\omega_1 t} + e^{-i\omega_1 t}}{2}, \\ \chi_2(t) &= \langle e|\hat{d}|k\rangle \frac{|E_2|}{\hbar} e^{i\phi_2} \frac{e^{i\omega_2 t} + e^{-i\omega_2 t}}{2} = \chi_2 \frac{e^{i\omega_2 t} + e^{-i\omega_2 t}}{2},\end{aligned}$$

$\omega_{gk} = \langle k|H_0|k\rangle / \hbar$  is the frequency which connects the ground and intermediate state, and  $\omega_{ge} = \langle e|H_0|e\rangle / \hbar$  is the frequency which connects the ground and excited states, setting our ground state energy to zero ( $\langle g|H_0|g\rangle / \hbar = 0$ ).

We plug this into the Schrödinger equation

$$i \begin{pmatrix} \dot{a}_g \\ \dot{a}_k \\ \dot{a}_e \end{pmatrix} = \begin{pmatrix} 0 & \chi_1(t) & 0 \\ \chi_1^*(t) & \omega_{gk} & \chi_2(t) \\ 0 & \chi_2^*(t) & \omega_{ge} \end{pmatrix} \begin{pmatrix} a_g \\ a_k \\ a_e \end{pmatrix} \quad (2.6)$$

then switch into the rotating frame:  $a_g = b_g$ ,  $a_k = b_k e^{-i\bar{\omega}t}$ ,  $a_e = b_e e^{-2i\bar{\omega}t}$ , where  $\bar{\omega} = \frac{\omega_1 + \omega_2}{2}$ . After eliminating any term which oscillates at optical frequencies, we find the following equations

$$\begin{aligned}\dot{b}_g &= -i \frac{\chi_1}{2} e^{-i\sigma t} b_k \\ \dot{b}_k &= -i \frac{\chi_1^*}{2} e^{i\sigma t} b_g - i\Delta b_k - i \frac{\chi_2}{2} e^{i\sigma t} b_e \\ \dot{b}_e &= -i \frac{\chi_2^*}{2} e^{-i\sigma t} b_k - i\delta b_e.\end{aligned} \quad (2.7)$$

Here we've simplified the math by introducing the variables  $\sigma = \frac{\omega_2 - \omega_1}{2}$ ,  $\delta = \omega_{ge} - 2\bar{\omega}$ , and  $\Delta = \omega_{gk} - \bar{\omega}$ . Importantly, we are in a rotating frame that is independent of  $\sigma$ , i.e. this frame will be shared by any  $\omega_{1,2}$  which add to the same  $2\bar{\omega}$ .

Numerically solving the ODEs in Eqn. 2.7 is the most complete approach. First, it is necessary to switch into density matrix formalism to capture the effects of spontaneous decay. This is a process of using the product rule of differentiation ( $\dot{\rho}_{mn} = \dot{b}_m b_n^* + b_m \dot{b}_n^*$ ) and much book-keeping. We accounted for spontaneous decay by the following additional terms:  $\dot{\rho}_{gg} : +\gamma \rho_{ee}$ ,  $\dot{\rho}_{ge} : -\frac{\gamma}{2} \rho_{ge}$ ,  $\dot{\rho}_{ee} : -\gamma \rho_{ee}$ , with  $\gamma = (238.5 \text{ ns})^{-1}$  being the inverse lifetime of the

excited state. An example of this numerical integration is shown in Fig. 2.5.

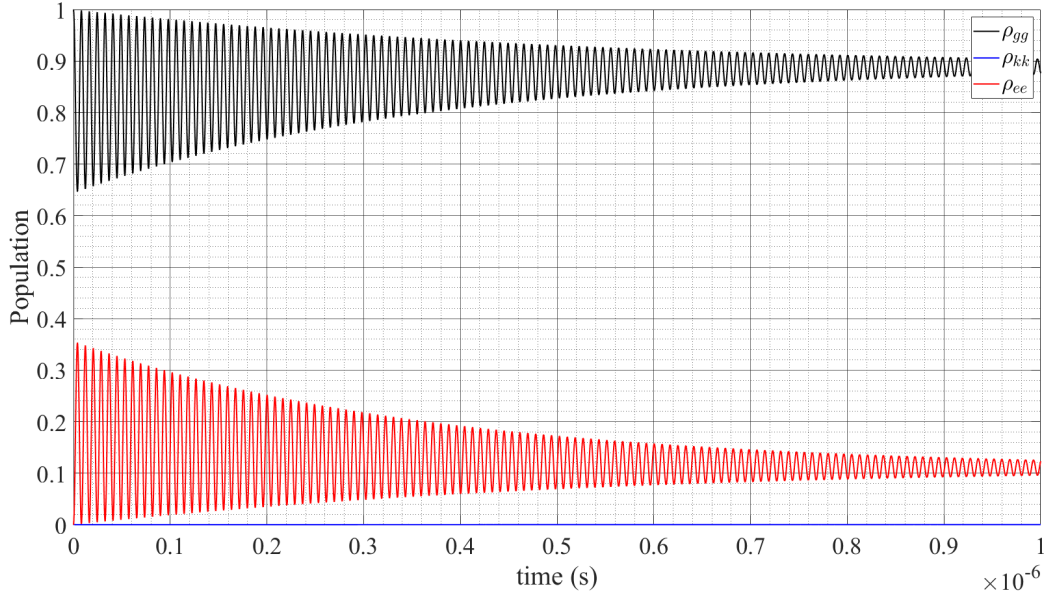


**Figure 2.5:** Populations from the density matrix math, provided an initial intensity of  $1\text{E}8 \text{ W/m}^2$ . Note the vanishing population of the intermediate state (blue).

Some additional insight is available by eliminating  $b_k$  and expressing these equations in terms of  $b_{g,e}$ . For this, we will directly integrate the equation for  $\dot{b}_k$ , first defining  $g(t) = e^{i\sigma t}(\chi_1^* b_g + \chi_2 b_e)$

$$\begin{aligned} \dot{b}_k + i\Delta b &= -ig(t) \rightarrow b_k = -ie^{-i\Delta t} \int_0^t e^{i\Delta t'} g(t') dt' \\ b_k &= -ie^{-i\Delta t} \left( \left[ \frac{e^{i\Delta t'}}{\Delta} g(t') \right]_{t'=0}^{t'=t} - \int_0^t e^{i\Delta t'} \frac{\dot{g}(t')}{\Delta} dt' \right) \end{aligned} \quad (2.8)$$

We know that  $g(t)$  is of the order  $\chi$ , whereas  $\frac{\dot{g}}{\Delta}$  is of the order  $\chi^3/\Delta^2$ . Therefore, if  $\chi^2 \ll \Delta^2$  then we can ignore the second integrand, and we are left with

$$b_k = \frac{1}{\Delta} g(t) - \frac{e^{-i\Delta t}}{\Delta} g(0).$$

In our experiment,  $\chi_1 \approx 7 \times 10^{11} \text{ s}^{-1}$  and  $\Delta \approx 2\pi \times 1 \text{ THz}$ , so  $\chi^2/\Delta^2 \approx 1/100$ , so this elimination is appropriate. Imposing the initial condition  $b_g(0) = 1, b_{k,e}(0) = 0$ ,

$$b_k = \frac{e^{i\sigma t}}{2\Delta}(\chi_1^* b_g + \chi_2 b_e) + \frac{e^{-i\Delta t}}{\Delta} \chi_1^* \approx \frac{e^{i\sigma t}}{2\Delta}(\chi_1^* b_g + \chi_2 b_e).$$

The last approximation only stands if  $\sigma \ll \Delta$ , so that on timescales that we're interested in  $e^{-i\Delta t}$  oscillates quickly enough to average out. For the rubidium transition we are interested in,  $\Delta \approx 2\pi \times 1\text{THz}$  and we will consider  $\sigma \lesssim 100\text{ GHz}$ , so this is a reasonable approximation. Substituting this solution for  $b_k$  back into the Eqn. 2.7

$$\begin{aligned} \dot{b}_g &= -\frac{i|\chi_1|^2}{4\Delta} b_g - \frac{i\chi_1\chi_2}{4\Delta} b_e \\ \dot{b}_e &= -\frac{i\chi_1^*\chi_2^*}{4\Delta} b_g - i\left(\frac{|\chi_2|^2}{4\Delta} + \delta\right) b_e \end{aligned} \quad (2.9)$$

It is from here useful to rotate one more time into  $b_{g,e} = c_{g,e} e^{-\frac{i|\chi_1|^2}{4\Delta} t}$  and define some simplifying variables:

$$\begin{aligned} \chi_{eff} &= \frac{\chi_1\chi_2}{2\Delta} \\ \delta_{eff} &= \delta + \frac{|\chi_1|^2 - |\chi_2|^2}{4\Delta} \\ \Omega &= \sqrt{\delta_{eff}^2 + |\chi_{eff}|^2} \end{aligned}$$

The Schrodinger equation then becomes

$$\begin{aligned} \dot{c}_g &= -i\frac{\chi_{eff}}{2} c_e \\ \dot{c}_e &= -i\frac{\chi_{eff}^*}{2} c_g - i\delta_{eff} c_e. \end{aligned} \quad (2.10)$$

We have recovered the two-level Rabi problem from this more complicated, three level, two field problem. Interestingly, the effective detuning has a contribution from the difference in magnitude of the Rabi frequencies  $\chi_{1,2}$ . Compared to two-level Rabi oscillations, where a  $\pi$  pulse on resonance results in a complete transfer of population from ground to excited



state, this three level Rabi oscillation has a maximum population in the excited state:

$$\rho_{ee}^{max} = \frac{|\chi_{eff}|^2}{\Omega^2} = 1 - \frac{\delta_{eff}^2}{\delta_{eff}^2 + |\chi_{eff}|^2} = 1 - \left( \frac{|\chi_1|^2 - |\chi_2|^2}{|\chi_1|^2 + |\chi_2|^2} \right)^2$$

In order to calculate the saturation intensity of this transition, we first find the steady state  $\rho_{ee}(\infty)$

$$\rho_{ee}(\infty) = \frac{1}{2} \frac{|\chi_{eff}|^2}{|\chi_{eff}|^2 + \Gamma^2 + 4\delta_{eff}^2} \quad (2.11)$$

From this equation, we can model the excited state population as a function of intensity, plotted in Fig. 2.6. Since excited state population will determine the signal-to-noise of the two-photon fluorescence detection, it is important to note that in the small power limit the excited state population increases as  $I^2$ . The effect of saturation becomes pronounced at about  $10^8$  mW/mm<sup>2</sup>, significantly higher than any intensity used in this experiment. This is also the point where  $\chi_1 \approx \Delta$ , so the approximation  $\chi^2 \ll \Delta^2$  used to eliminate the intermediate state breaks down. To truly calculate excitation near that level of saturation would require moving back to the three-level differential equations.

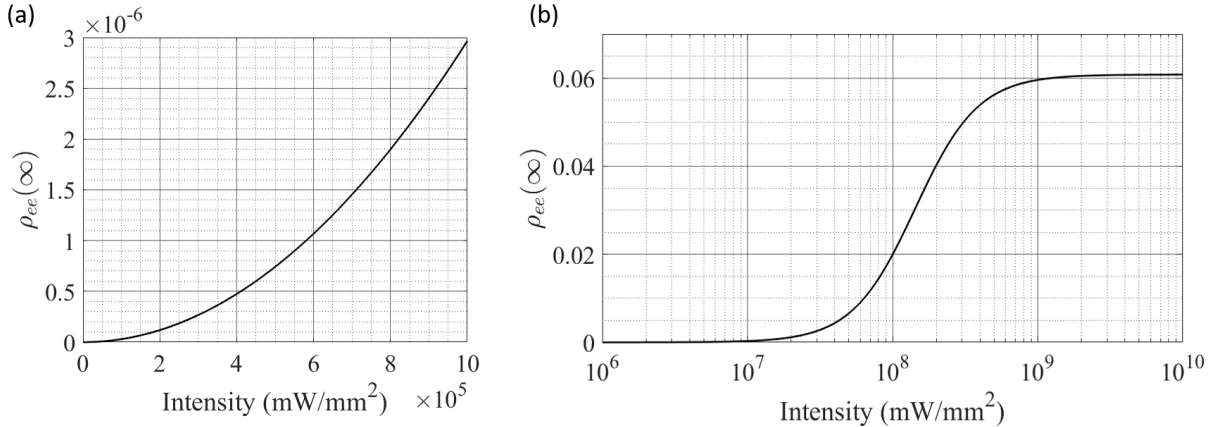


**Figure 2.6:** Steady state population of the excited state, which determines the fluorescence. (a) shows the quadratic dependence of excitation on the incident power at low probe powers. (b) shows the effect of saturation at higher probe powers (above  $10^8$  mW/mm<sup>2</sup>).

### 2.2.2 *fm-Spectroscopy*

While the mechanism for exciting two-photon transitions has been explained, I have yet to explain how one stabilizes a laser to a particular transition. This is achieved through fm-spectroscopy, a close parallel to the Pound-Drever-Hall technique. The traditional treatment of absorption fm-spectroscopy, laid out well in reference [55], has subtle differences when applied to fluorescence fm-spectroscopy. This technique involves frequency modulating the probe laser of frequency  $\omega_c$  with modulation frequency  $\omega_m$ , such that the optical spectrum of said laser becomes

$$E(t) = E_0 \left( -\frac{\beta}{2} e^{-i(\omega_c - \omega_m)t} + e^{-i\omega_c t} + \frac{\beta}{2} e^{-i(\omega_c + \omega_m)t} \right), \quad (2.12)$$

where  $M$  indicates the strength of modulation.

In traditional fm-spectroscopy the laser is then passed through a sample and detected on a photodetector, where one finds the voltage on the detector is proportional to intensity  $I \propto |E|^2$ , and thereby the voltage has some oscillation as  $\omega_m$ . Here, the atoms provide that intensity detection:  $\rho_{ee} \propto |E_{\rightarrow}|^2 |E_{\leftarrow}|^2$ . Since the fluorescence goes as  $|E|^4$  rather than  $|E|^2$ , the math becomes more complicated than the math in Ref. [55] quickly. Additionally, in standard absorption based fm-spectroscopy the frequency modulation can be arbitrarily fast, since the role of the sidebands is to resolve the phase of the carrier via heterodyning on a detector. In fluorescence based fm-spectroscopy, the sidebands modulate the excited state population  $\rho_{ee}$ , and consequently the frequency modulation must be slower than “a few times the decay rate” [56]. However, within that bandwidth limitation the dispersive lineshapes recovered from demodulating the fluorescence at  $\omega_m$  closely match those recovered from absorption fm-spectroscopy.

## 2.3 Direct Comb Doppler-Free Two-Photon Spectroscopy

Before the use of frequency combs as gearwork for optical atomic clocks, a series of experiments were identifying the phenomenon that will define the remainder of this dissertation: two-photon transitions can be excited with ultra-short pulses. First proposed in 1976 [57] and first experimentally demonstrated that same year [58], direct comb excitation of Doppler-free

two-photon transitions has led to many interesting publications [59–64]. Though cw two-photon rubidium clocks have been evaluated as frequency standards since 1998 [51], direct comb excitation had not been evaluated as an atomic clock until 2015 [65], and there it failed to show performance competitive with cw standards. We will more closely examine direct comb excitation in an effort to understand how it can be made competitive with cw excitation.

The basic idea of direct comb excitation is that two-photon transitions do not require two degenerate photons, merely two photons which add to the energy level separation  $\omega_{ge}$ . Combining this with the symmetry of a frequency comb (Eqn. 1.2) means that if a comb tooth  $\nu_n$  is resonant with the transition (i.e.  $2\nu_n = \omega_{ge}/2\pi$ ) then any pair of comb teeth symmetric about  $\nu_n$  can also contribute to excitation  $\nu_{n+x} + \nu_{n-x} = \omega_{ge}/2\pi$ . Additionally, if  $\omega_{ge}/4\pi$  lies directly between two comb teeth, every pair of comb tooth mirrored about that frequency can contribute to excitation. This idea is illustrated in Fig. 2.7. The time domain picture of this process is a pair of pulses with a carrier frequency on resonance with the degenerate two-photon transition which, when they overlap in the vapor cell, lead to two-photon Doppler free excitation. This question of pulse overlap will be explored in the following section.

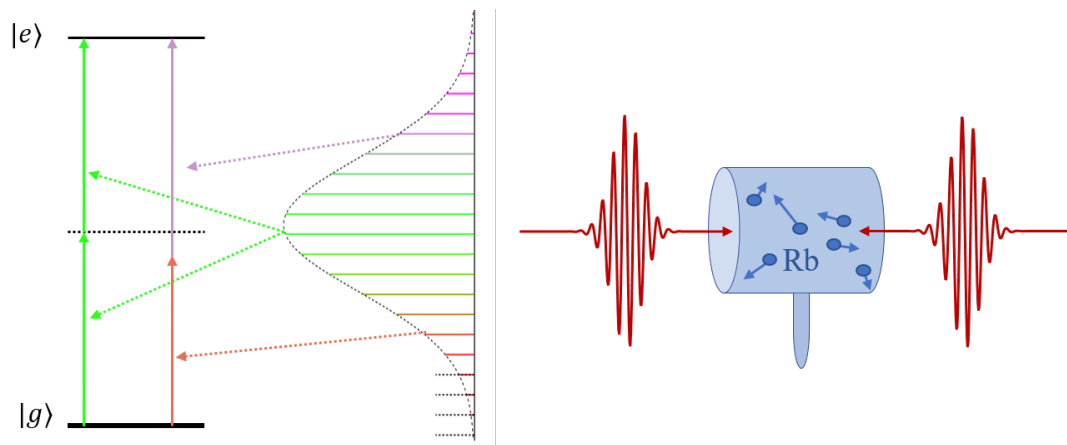


**Figure 2.7:** Pedagogical picture of direct comb two photon excitation, showing the excitation by symmetric pairs of comb teeth on the left and overlap of pulses in a vapor cell on the right.

### 2.3.1 Excitation Rate

We established in the last section the basis for two-photon Doppler-free spectroscopy with two optical fields,  $\omega_1$  and  $\omega_2$ , with some average frequency  $\bar{\omega}$  and a frequency separation  $\sigma$ . Since this derivation was kept independent of  $\sigma$ , the effective Hamiltonians can add in the frame of Eqns. 2.9, accounting for excitation from different pairs of comb teeth. For ease of reference, here is Eqn. 2.9 restated.

$$\begin{pmatrix} \dot{b}_g \\ \dot{b}_e \end{pmatrix} = \begin{pmatrix} -i\frac{|\chi_1|^2}{4\Delta} & -i\frac{\chi_1\chi_2}{4\Delta} \\ -i\frac{\chi_1^*\chi_2^*}{4\Delta} & -i\left(\frac{|\chi_2|^2}{4\Delta} + \delta\right) \end{pmatrix} \begin{pmatrix} b_g \\ b_e \end{pmatrix} \quad (2.13)$$

Calculating the total rate equations for frequency comb excitation amounts to building a total  $|\chi_1|^2$ ,  $\chi_1\chi_2$ , and  $|\chi_2|^2$  by summing over pairs of comb teeth  $E_{\pm m}$  symmetric about  $\omega_{ge}$  (i.e. all with the same  $\Delta$ ), each with its own phase and amplitude.

$$|\chi_1^{tot}|^2 = \left| \frac{\langle k|d|g\rangle}{\hbar} \right|^2 \sum_m |\tilde{E}(\omega_{ge} + m \times f_{rep})|^2 \quad (2.14)$$

$$\chi_1\chi_2 = \frac{\langle k|d|g\rangle \langle e|d|k\rangle}{\hbar^2} \sum_m \tilde{E}(\omega_{ge} + m \times f_{rep}) \times \tilde{E}(\omega_{ge} - m \times f_{rep}) \quad (2.15)$$

$$|\chi_2^{tot}|^2 = \left| \frac{\langle e|d|k\rangle}{\hbar} \right|^2 \sum_m |\tilde{E}(\omega_{ge} + m \times f_{rep})|^2 \quad (2.16)$$

Now we must consider the complex term  $\chi_1\chi_2$  as dependent upon the phase of our frequency comb spectrum. We will have to consider one field as traveling forward and one as traveling backward for Doppler cancellation; let  $\chi_1$  be the forward traveling and  $\chi_2$  be backwards traveling. Any linear phase slope across the spectrum amounts to a translation in time of a given pulse: we will pick a starting time/location such that both pulses overlap at the same location  $t = 0 = z$ . We will also pick the center of the pulse overlap region to have zero phase at  $t=0$  for  $\tilde{E}(\omega_{ge})$ .

The two major phase effects we will consider are 1.) How do the multiple frequencies dephase at a given  $z$  (i.e. what is the spatial extent of the fluorescence) and 2.) What effect does chromatic dispersion have on collected fluorescence? Translating to position  $z$

equates to a phase change on the light field as  $\phi = \pm \frac{2\pi\omega_m}{c}z$  ( $\pm$  to account for forward or backward going beams respectively). Since we care about phase offsets more than global phase, consider rather phase offsets from the phase of the center frequency:  $\Delta\phi = \pm \frac{2\pi\Delta\omega}{c}z$ , where  $\Delta\omega = \omega - \omega_{ge} = m \times f_{rep}$ . Recall that, for Doppler free absorption, only pairs of frequencies with opposite  $m$  add: therefore, any pair of frequencies has total phase on  $\chi_1\chi_2$  of  $\Delta\phi = \frac{4\pi m f_{rep}}{c}z$ . The results of including this in the calculation for steady state excited state population (Eqn. 2.11) are shown in Fig. 2.8

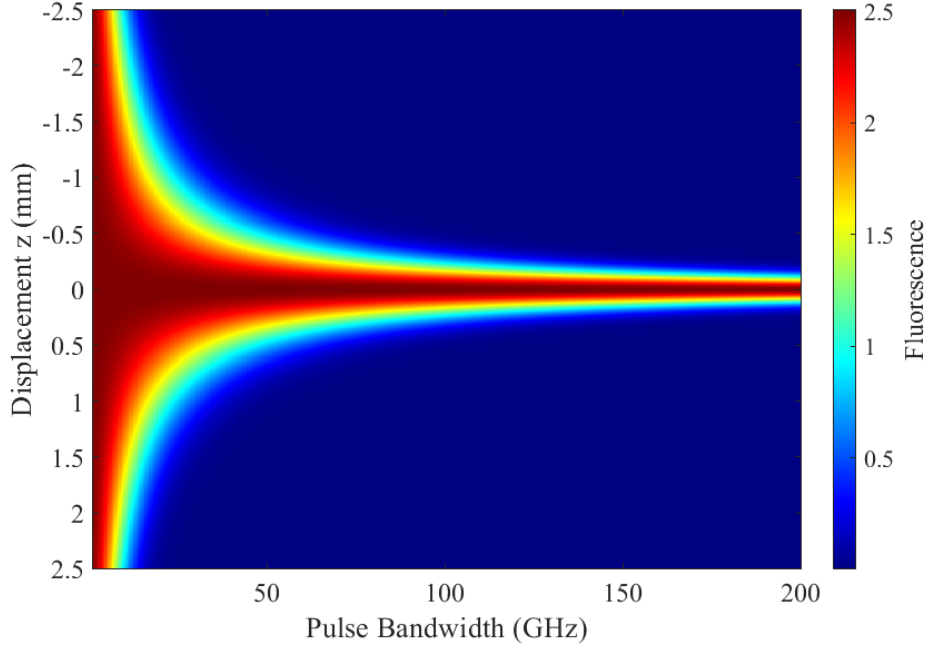


**Figure 2.8:** Spatial extent of fluorescence from pulses of different pulse bandwidths, defined as the standard deviation of the gaussian power spectrum.

Since a well designed fluorescence detection scheme integrates the fluorescence over a wide spread of  $z$ , it is apparent from Fig. 2.8 that a smaller pulse bandwidth ought to result in increased integrated fluorescence. This can also be thought of as a smaller bandwidth increasing the pulse length, thereby increasing the volume where the pulses overlap. Assuming perfect integration over the length of a vapor cell, the total fluorescence compared to cw-excitation is plotted in Fig. 2.9 for two different vapor cell lengths.

Next we must consider the effect of chirp. On the one hand, at  $z = 0$ , chirp intuitively leads to lower fluorescence, as the multiple excitation channels will not add completely in-phase.

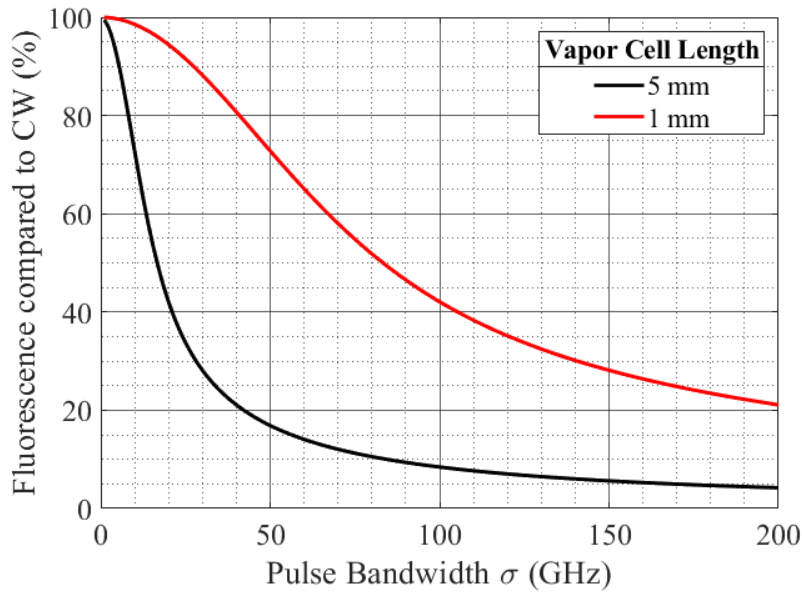


**Figure 2.9:** The relative level of integrated fluorescence compared to that of a cw probe for a vapor cell of active length 5 mm (black) and 1 mm (red). Bandwidth is reported as the standard deviation of the gaussian power spectrum.

However, chirp also leads to pulse broadening, meaning a larger pulse overlap volume. We here examine second-order dispersion (also called “group-delay dispersion”), which is equivalent to multiplying the frequency comb spectrum with a phase mask  $\exp(i\pi k''(\nu - \nu_{ge}))$ . The dual effects of pulse broadening and fluorescence maximum decrease can be visualized by looking at many displacements for different  $k''$  at the same bandwidth (Fig. 2.10).

We see that Fig. 2.10 matches our intuition for spatial broadening of the fluorescence volume accompanied by lower peak fluorescence. By integrating along the length of the vapor cell, we can estimate the total collected fluorescence, shown in Fig. 2.11. We see from this that (assuming efficient fluorescence collection along the entire vapor cell length) group-delay dispersion only begins to negatively effect the total signal strength once the fluorescence orb begins to exceed the length of the vapor cell. This is further highlighted by the increased tolerance to chirp for a 10 mm vapor cell, plotted in red. This is in agreement with the results of Ref. [66].

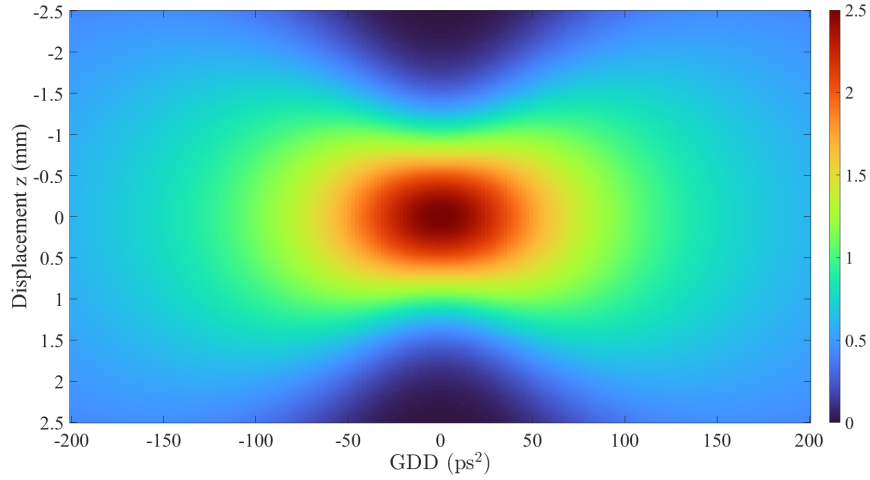


**Figure 2.10:** Fluorescence from a 75 GHz FWHM optical spectrum at different levels of second-order dispersion (GDD). Note that past  $\approx 75 \text{ ps}^2$  significant power begins leaving the vapor cell (which extends from  $-2.5 \rightarrow 2.5 \text{ mm}$ ).

### 2.3.2 Residual Doppler Broadening

Our discussion of Doppler cancellation for two-photon transitions in §2.2 relied on a degenerate frequency for the two photons exciting the transition. Now that we have moved on to direct comb excitation, this is no longer strictly satisfied. Recall from our derivation in §2.2.1 the useful variable  $\sigma = \frac{\omega_2 - \omega_1}{2}$ , which in the direct comb context refers to the spacing of a comb tooth from the half-frequency  $\omega_{ge}/2$ . Thus, pairs of comb teeth with  $\sigma \neq 0$  will have a net Doppler shift dependent on that  $\sigma$ .

The net Doppler shift from the two comb teeth on an atom moving with velocity  $\vec{v}$  is:

$$\omega_{net} - \omega_{ge} = \vec{v} \cdot \hat{k} \left( \frac{\omega_2}{c} - \frac{\omega_1}{c} \right) = v_z \frac{2\sigma}{c}, \quad (2.17)$$

letting the light propagate along  $\pm \hat{z}$ . We want to consider what happens when one sweeps the frequency of both comb teeth together: therefore, we will consider the change of  $\bar{\omega} = \omega_{net}/2$ . Following the derivation from [14, §3.11], we invert this into an equation for  $v = \frac{c}{\sigma} (\bar{\omega} - \frac{\omega_{ge}}{2})$ , and substitute into the one-dimensional Maxwell-Boltzmann distribution  $df(v)dv$ :

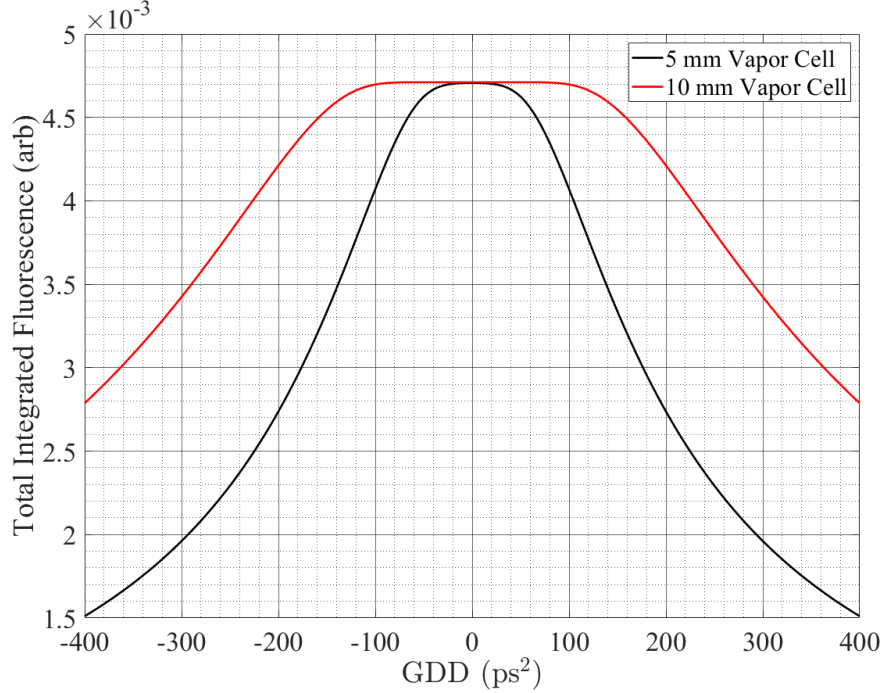


**Figure 2.11:** Fluorescence from a 75 GHz FWHM optical spectrum at different levels of second-order dispersion GDD, integrated along a 5 mm length (black) and a 10 mm length (red). Note the reduction in fluorescence for the 5 mm cell beginning at 75 ps<sup>2</sup>, in agreement with Fig. 2.10. A 10 mm vapor cell can accommodate about twice the chirp.

$$df(v) = \sqrt{\frac{m}{2\pi k_B T}} e^{-mv^2/2k_B T} dv \rightarrow S(\bar{\omega}) = \sqrt{\frac{mc^2}{2\pi k_B T \sigma^2}} e^{-mc^2(\bar{\omega} - \frac{\omega_{ge}}{2})/2k_B T \sigma^2}, \quad (2.18)$$

with  $m$  being the mass of a <sup>87</sup>Rb atom,  $c$  being the speed of light,  $k_B$  as the Boltzmann constant,  $T$  as the absolute temperature.

Equation 2.18 describes the Doppler lineshape of a given pair of comb teeth. To properly predict the total Doppler lineshape, we must add the lineshape from each pair of comb teeth in our spectrum, normalized by the excitation from that pair of comb teeth (i.e. intensity squared). Each lineshape that we add will be generated by the convolution of the lorentzian linewidth (set at 330 kHz) and the residual Doppler gaussian. The results of this simulation are shown in Fig. 2.12. The important takeaway is that for spectral bandwidths below 300 GHz FWHM the residual Doppler broadening is trivial compared to the natural linewidth



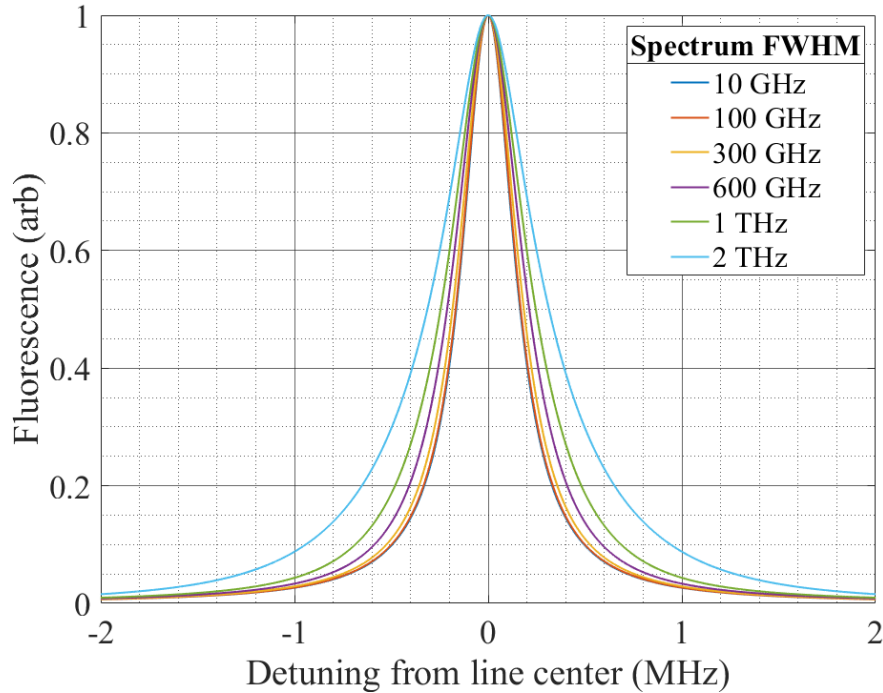


**Figure 2.12:** Residual Doppler broadening for gaussian input spectra of various  $\Delta\nu_{FWHM}$ .

of this transition.

### 2.3.3 Aliasing

One of the major differences between excitation with a frequency comb vs a cw laser is that many transitions may fall under the broad spectrum of the probing radiation. This can result in spectral congestion, where one may excite multiple transitions at a given  $f_{rep}$ , resulting in distorted line shape, line-pulling, frequency lock ambiguities, and generally diminished clock performance. Hence it is necessary to predict for any elements within the vapor cell, what the resonant  $f_{rep}$ s are for any two-photon transition  $\nu_{pq}$  within the bandwidth of the probing frequency comb. Inversely and more intuitively, starting at an  $f_{rep}$  which excites the clock transition, how far would one need to move the optical comb teeth before another transition is excited?

Recall that the resonant condition for direct comb excitation is that a given transition is either coincident with or half-way between two optical comb teeth. This is the same as saying that the transition must be coincident with the teeth of an optical frequency comb

with repetition rate  $f_{rep}/2$ . Then, the answer to our question from the last paragraph is

$$\delta\nu = \frac{\nu_{pq}}{2} - \frac{\nu_{ge}}{2} \pmod{\frac{f_{rep}}{2}}, \quad (2.19)$$

where  $2\pi\hbar\nu_{pq}$  is the energy separation between two atomic energy levels, and  $2\pi\hbar\nu_{ge}$  is the energy separation of the ground and excited states of our clock transition.

With this formulation in hand, one is then able to plot the expected location for any transition given any repetition rate, which is of great help when selecting a frequency comb to use for direct comb excitation. The locations of all the hyperfine transitions of Rb-87 and Rb-85 are plotted in Figs. 2.13, 2.14 and 2.15. The code for generating these plots is located in [67].

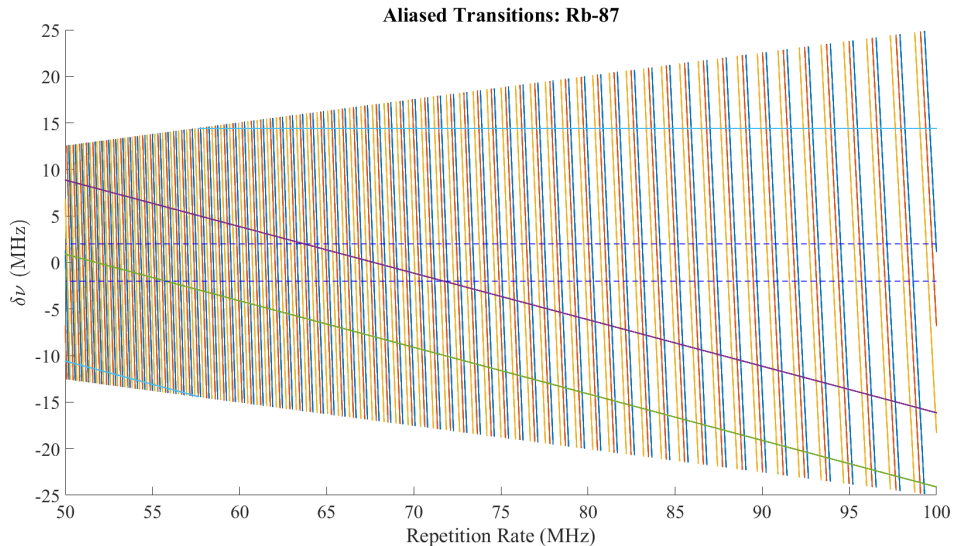


**Figure 2.13:** Stick model of the location for all hyperfine two-photon transitions between  $5S_{1/2} \rightarrow 5D_{5/2}$  in rubidium 87, for location of usable frequency comb repetition rates.

These plots show for a given repetition rate, how far the comb tooth that is resonant with the two-photon clock transition would have to move to excite a different two-photon transition. Hence, it is desirable to select a repetition rate where no transitions are closer to the clock transition than the transition linewidth, indicated by the blue dashed lines. You can see in Fig. 2.13 that there are few repetition rates less than 100 MHz which satisfy this criterion. In contrast, repetition rates 200 MHz and higher (Fig. 2.14) provide a wide range of possible options, even when considering the locations of two-photon transitions in  $^{85}\text{Rb}$

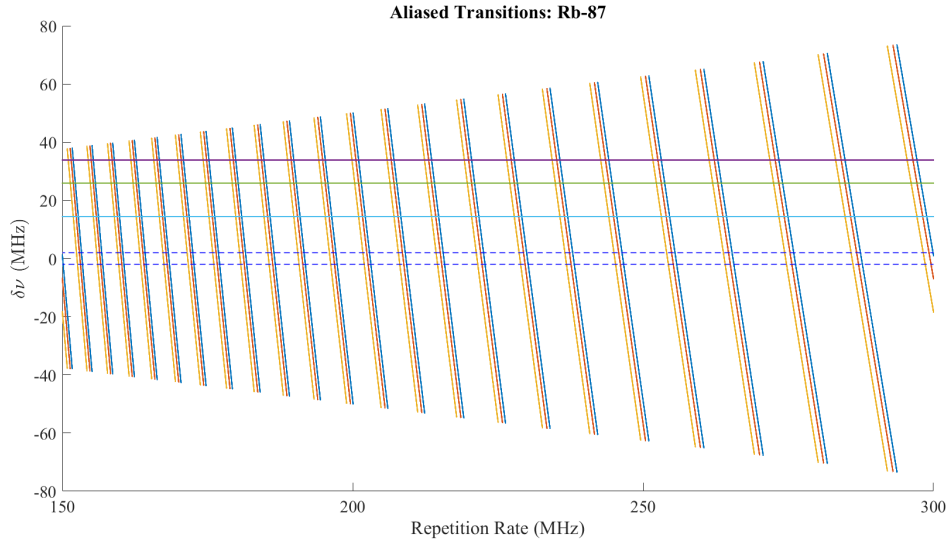


**Figure 2.14:** Stick model of the location for all hyperfine two-photon transitions between  $5S_{1/2} \rightarrow 5D_{5/2}$  in rubidium 87, for higher repetition rates. The significant increase in space between transitions highlights the advantage of using higher repetition rate frequency combs.

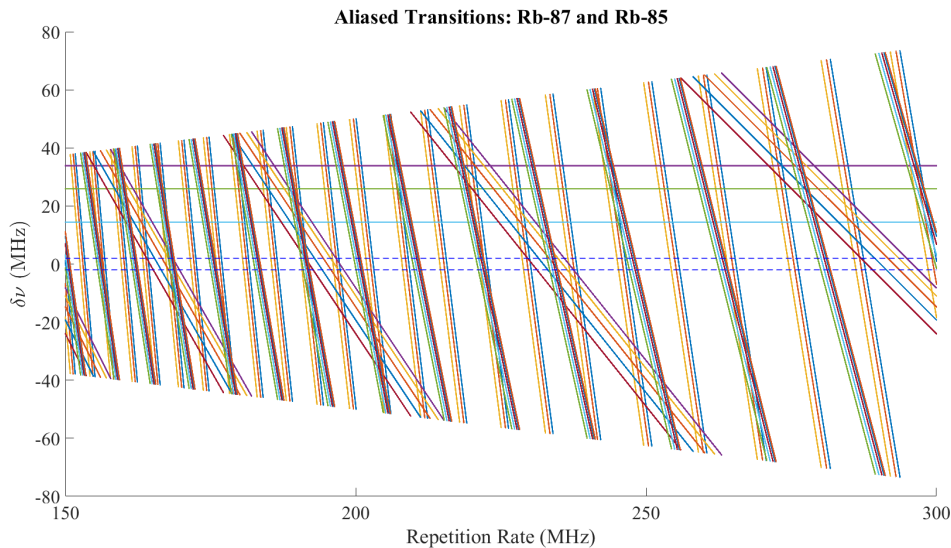


**Figure 2.15:** Stick model of the location for all hyperfine two-photon transitions between  $5S_{1/2} \rightarrow 5D_{5/2}$  in both rubidium 87 and 85, for higher repetition rates. Since even isotopically enriched vapor cells may contain small amounts of undesired isotopes, this graph is a better qualifier for a suitable  $f_{rep}$ .

(Fig. 2.15), which are present even in isotopically enriched vapor cells.

The two frequency combs which we use in this project have repetition rates of 200 MHz and 250 MHz. The expected spectra from Eqn. 2.19, with the transition frequencies and

relative strengths from [50], are plotted against the measured spectra from each frequency comb in Figs. 2.16 and 2.17. Indeed, even some  $^{85}\text{Rb}$  transitions are identifiable in the floor of these measurements (Fig. 2.18). While both the 200 MHz and 250 MHz repetition rates result in a clock transition well isolated from other  $^{87}\text{Rb}$  transitions, only the 250 MHz repetition rate also isolates the clock transition from all  $^{85}\text{Rb}$  transitions.

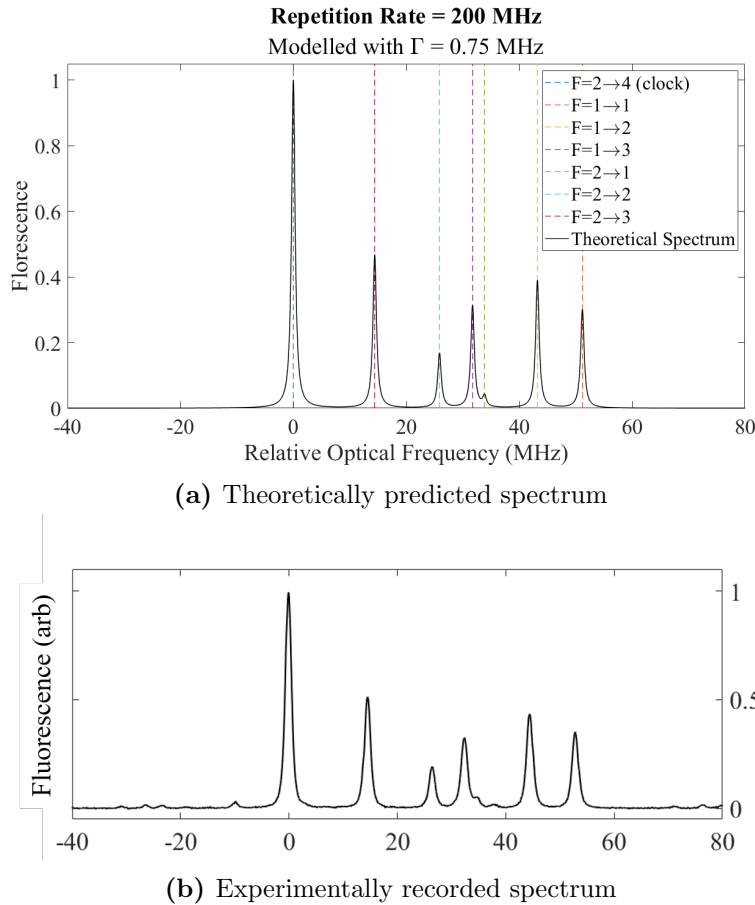


**Figure 2.16:** Comparison between theory from Eqn. 2.19 and experiment for our 200 MHz frequency comb.

This is an important subtlety to direct comb spectroscopy. Not only may transitions from the isotope of interest lead to spectral congestion, but any contaminants with two-photon transitions within the bandwidth of the probe pulses may also be excited, and if they alias into proximity with the clock transition, may be a source of instability. For example, in Fig. 2.18, there is a transition  $\approx 9$  MHz removed from the clock transition at 200 MHz  $f_{rep}$  and  $\approx 12$  MHz removed at 250 MHz  $f_{rep}$  that appears to be neither Rb-87 or Rb-85. This transition has yet to be identified.

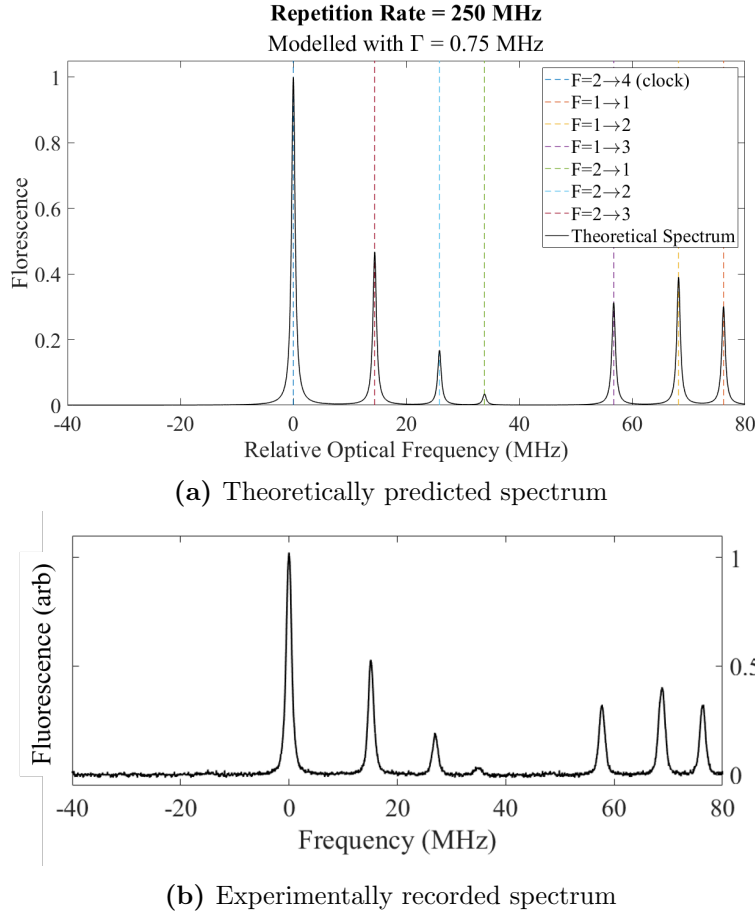


**Figure 2.17:** Comparison between theory from Eqn. 2.19 and experiment for our 250 MHz frequency comb.

One may well ask why spectral congestion is so necessarily avoided in these direct comb clocks. If the clock transition is much stronger than the contaminant lines, or if only the wings of the contaminant lorentzians overlap with the clock transition, surely the effect on the  $Q$  of the transition is negligible, and any line-pulling may be accounted for with a constant calibration factor. The subtlety lies herein: the strength of the obfuscating two-photon transitions is dependent upon the spectral distribution of light in the probe pulse, which may change with time. Hence any two-photon transitions which pull the lock-point away from the true center of the clock transition may become a time varying shift, decreasing the stability of this reference.

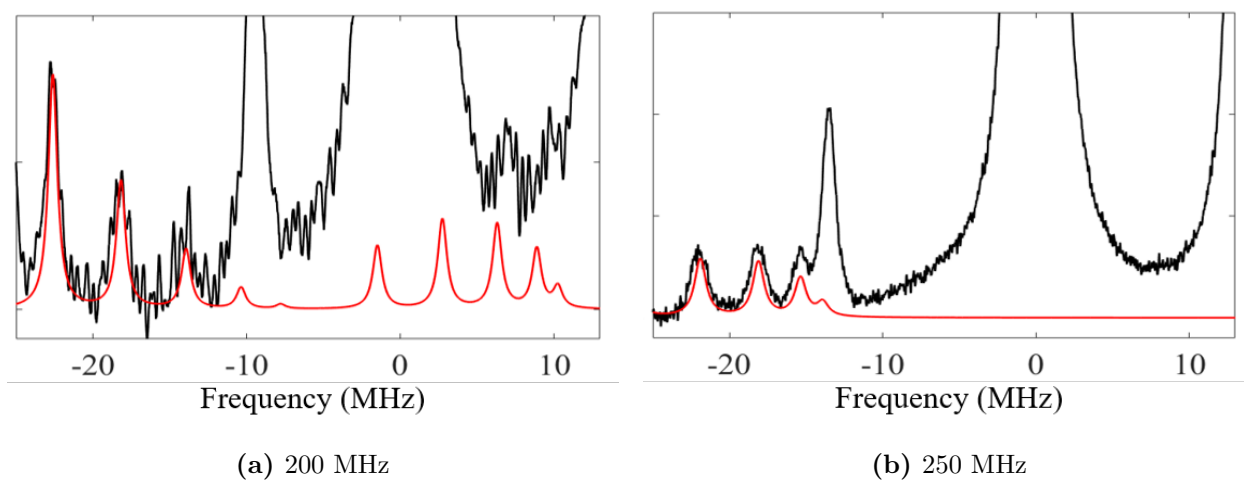


**Figure 2.18:** Small amounts of rubidium 85 can be seen in both vapor cells, identified by the overlap with theoretically predicted rubidium 85 fluorescence locations (shown in red). The clock transition ( $F=2 \rightarrow 4$ ) in rubidium is at 0 MHz in both figures.

## Chapter 3

### Direct Comb Spectroscopy as an Optical Atomic Clock

#### 3.1 Advantages of a Direct Comb Reference

While it stood to be experimentally proven that direct comb excitation is a viable atomic clock platform, it is worthwhile to ask *why* it should be proven. There are several potential benefits from direct comb excitation which can be reduced to two key arguments: reduced system SWaP and availability of multi-wavelength interrogation. The first is applicable in the short-term; the second will be tackled in the conclusion of this dissertation.

Direct comb excitation reduces system SWaP through the reduction of necessary lasers. A frequency comb is necessary in both cw clocks (as gearwork) and direct comb clocks, but direct comb clocks do not require the additional cw probe laser, removing a laser and a phase lock from the overall system budget. In more complicated setups [68], two or more lasers, as well as associated electronics, can be removed by deriving each from the same frequency comb. As two-photon clocks move towards consistently smaller packaging requirements [69], and especially as they are considered for space applications, each laser that can be removed is a significant improvement.

Additionally, as we will discuss in §3.2.2, the stability of these optical references can be limited by frequency noise on the probe laser. Commercially available compact 778 nm lasers tend to have significantly higher phase noise than compact 1556 nm lasers, so the narrow-linewidth 778 nm light is generally generated by second harmonic generation of a 1556 nm laser. Since SHG is a  $\chi^{(2)}$  process, the high peak powers in ultrashort pulses result in frequency doubling with significantly higher efficiency than CW (Fig. 3.1). While this is a particular benefit for rubidium two-photon clocks, there is a much deeper point to be made: the high peak intensities available from frequency combs enable efficient generation of

light at wavelengths which are less accessible by cw lasers. Hence, direct comb excitation is a promising direction for potential frequency references in the ultraviolet, such as hydrogen transitions [64] or thorium transitions [70].

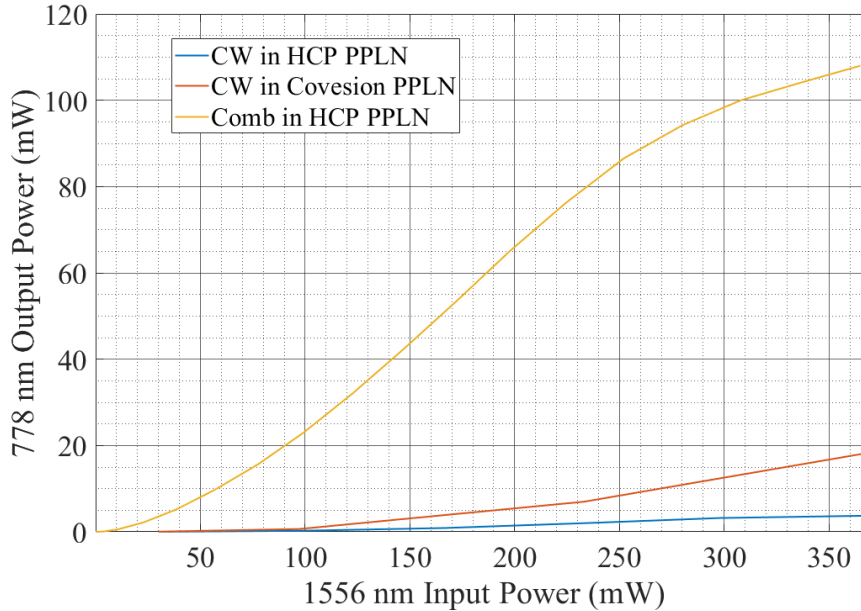


**Figure 3.1:** Comparing the SHG conversion efficiency for cw vs. comb in two waveguide periodically poled lithium niobate (PPLN) frequency doublers. The significantly longer Coversion waveguide has a better doubling efficiency than the HCP waveguide (5% vs 1%), but neither approaches the 30% doubling efficiency of a picosecond pulse in a waveguide doubler.

While a rubidium optical frequency standard based on direct comb excitation has these promising advantages for SWaP, it is necessary to evaluate the expected performance. This will be done by evaluating the most likely sources of instability, some common to cw excitation, and some unique to direct comb excitation.

## 3.2 Sources of Instability

### 3.2.1 Shot Noise

Shot noise is fundamental to any Poissonian process; if the mean number of independent, random events that happen over many time windows of width  $\Delta t$  is  $N$ , then the variance in number of events that will happen in any given time window of the same  $\Delta t$  is  $\sqrt{N}$ . This is, strictly speaking, an approximation which only holds for time windows which include



sufficiently many random events that the discreteness may be approximated by a white-noise distribution. In this experiment, the Poissonian process is the spontaneous decay of a  $^{87}\text{Rb}$  atom in the  $6P_{3/2}$  state down to the ground  $5S_{1/2}$  state, accompanied by the emission of a 420 nm photon. More precisely, it is the detection of said 420 nm photon, determined by the number of fluorescence events ( $\Gamma_{det\rho_{33}}$ ), the collection efficiency of the light collection scheme, and the quantum efficiency of the photomultiplier tube.

How does this random process effect the fractional frequency instability of a clock? This white-noise process is well characterized as  $S_I^{SN} = e \langle I \rangle$  [71, §17.5.3.1], in units [ $A^2/Hz$ ]. This noise spectral density interferes with our intended measurement of fluorescence strength  $\langle I \rangle$ . To convert this to fractional frequency noise, consider that a drift in laser frequency by  $\Delta\nu_{FWHM}/2$  is accompanied by a change in photocurrent of  $\langle I \rangle / 2$ ; therefore  $S_\nu^{SN} \approx S_I^{SN} \times \frac{\Delta\nu_{FWHM}^2}{\langle I \rangle^2}$ . Recall that  $S_y = \frac{S_\nu}{\nu^2}$  and  $\Delta\nu_{FWHM}/\nu = Q$ , therefore  $S_y \approx \frac{S_I^{SN}}{\langle I \rangle^2 Q^2} = \frac{e}{\langle I \rangle Q^2} = \frac{1}{\Gamma Q^2}$ , where  $\Gamma = \frac{\langle I \rangle}{e}$  is the rate of electron generation from the PMT. A white frequency noise power of  $S_y = h$  results in an Allan deviation of  $\sigma_y(\tau) = \sqrt{\frac{h}{2\tau}}$  [72, §1.8]; therefore, shot noise limits the instability of a frequency reference by

$$\sigma_y^{SN}(\tau) \approx \frac{1}{Q\sqrt{2\Gamma}} \frac{1}{\sqrt{\tau}}. \quad (3.1)$$

This is, unfortunately, a simplified and optimistic approach to the theory of shot noise. Since our error signal is generated via fm-spectroscopy (§2.2.2), the signal that is affected by shot noise is not the peak fluorescence, but only the part of the fluorescence signal that demodulates to give an error signal. Thus, it is critical to modulate with the correct modulation depth  $\beta$  and frequency  $\omega_m$  to maximize the fluorescence signal at  $\omega_m$ . More discussion of the theory of shot-noise limited fm-spectroscopy can be found in Ref. [55]. In practice, the optimum modulation depth is found experimentally by increasing the modulation depth until the slope of the error signal ceases to increase; this should be close to maximizing the power in the first sidebands and therefore maximizing the useful signal.

### 3.2.2 Intermodulation Noise

Intermodulation noise is a process by which frequency fluctuations on the probe laser at twice the modulation frequency produce random fluctuations on the zero-crossing of an fm-spectroscopy error signal [73]. While this is a well-known principle, the original derivation requires Taylor expansion in frequency about a dithering center frequency, which is the point where most experimentalists stop paying attention and instead just trust the result without gaining any intuition. I intend, rather, to discuss an intuitive explanation for the source of this frequency noise, then to state the results proven in Ref. [73].

The frequency domain picture of fm-spectroscopy was laid out in §2.2.2; consider now the time domain. In the time domain, frequency modulation looks like dithering the laser frequency such that  $\nu_L(t) = \nu_0 + \Delta + \beta \sin(2\pi f_m t)$ , where  $\nu_0$  is the central laser frequency,  $\Delta$  is the frequency detuning from resonance,  $\beta$  is the modulation depth, and  $f_m$  is the modulation frequency. This dithering frequency sweeps over a fluorescence line with a Voigt lineshape, with lorentzian width set by lifetime broadening and collisional broadening and gaussian width set by transit-time broadening and residual Doppler broadening. However, let us instead consider the approximation that the measured fluorescence is  $V(t) \propto -(\nu_L(t) - \nu_0)^2$ . Near the center of the Voigt lineshape, this is not a bad approximation, and it captures the even symmetry of the real lineshape — this even symmetry is important. The fluorescence signal resulting from this dithering probe is

$$V(t) \propto (\Delta + \beta \sin(2\pi f_m t))^2 = \Delta^2 + 2\Delta\beta \sin(2\pi f_m t) + \beta^2 \sin^2(2\pi f_m t).$$

Locking-in on the modulation frequency  $f_m$  then gives a voltage proportional to  $\Delta$ , and thus we have a zero-crossing error signal. But what if the laser frequency also had another modulation term at  $2f_m$ , with time varying amplitude  $s(t)$  and phase  $\phi(t)$ ?

$$\begin{aligned} V(t) &\propto (\Delta + \beta \sin(2\pi f_m t) + s(t) \sin(2\pi(2f_m)t + \phi(t)))^2 \\ &= (\text{DC terms}) + 2\Delta\beta \sin(\omega_m t) + \beta s(t) \cos(2\pi f_m t + \phi(t)) + (2f_m \& 3f_m \text{ terms}) \end{aligned}$$

Now, locking-in on the modulation frequency gives a voltage determined not only by  $\Delta$ , but also by amplitude and phase of the additional signal at  $2\omega_m$ . Where this becomes important is that every laser has some frequency deviations at  $2f_m$ ; this frequency noise, described by the fractional frequency deviation power spectral density  $S_y(2f_m)$ , thus result in a shifting zero-crossing of the error signal and therefore frequency instability. This sets a limit on the final clock stability referred to as the intermodulation limit [73]:

$$\sigma_y^{IM}(\tau) = \frac{\sqrt{S_y(2f_m)}}{2\sqrt{\tau}} \quad (3.2)$$

### 3.2.3 Residual Amplitude Modulation

Residual amplitude modulation (RAM) is well known to negatively effect the precision of fm-spectroscopy [55]. In time, this effect can be considered as a dither in laser power at the same frequency as the frequency dither, thus resulting in an additional detected signal at that frequency and a shift in the zero-crossing of the fm-spectroscopy error signal. Alternatively, consider the frequency space picture: an ideal frequency modulated laser source with carrier frequency  $\nu_c$  has sidebands at  $\nu_c \pm f_m$  which are equal in power and  $\pi$  out of phase with each other. If anything between the frequency modulation and the atoms results in a breakdown of that anti-symmetry, the beatnote of the  $+f_m$  sideband against the carrier will no longer destructively interfere with the beatnote of the  $-f_m$  sideband against the carrier when the carrier is at the center of a resonance. In either picture, the lock-in amplifier will demodulate this RAM into a shift in the linecenter of the error signal and hence a shift in the clock frequency.

Since RAM can limit the instability of atomic frequency references, several techniques to overcome this limitation a have been developed. One technique requires additional frequency modulation at  $f_m/2$ , such that the second harmonic from the additional modulation cancels the RAM at  $f_m$  [74]. Another technique is to lock-in on higher harmonics of the fm-spectroscopy signal which, when driven with the appropriate modulation strength, respond symmetrically to RAM and result in no line-center shift [75].

The most straightforward approach is to measure and stabilize the RAM through feedback on the phase-modulator bias voltage and/or temperature [76–78]. Waveguide electro-optic

modulators (EOMs), which we use to phase modulate our probe light, generate RAM in many ways, including etaloning and piezoelectric beam-steering; the most significant effect is imperfect polarization matching. Working through the derivation from [76], consider an EOM with an extraordinary axis misaligned from the input beam polarization by angle  $\alpha_{in}$  and misaligned from the output polarizer by angle  $\alpha_{out}$ . The Pockels effect on the EOM crystal turns the ordinary and extraordinary index of refraction  $n_{o,e}$  into a voltage dependent indices of refraction:

$$n_{o,e}(V) = n_{o,e} - \frac{1}{2}n_{o,e}^3 r_{o,e} \frac{V}{d}, \quad (3.3)$$

where  $V$  is the applied voltage across the EOM capacitor plates separated by distance  $d$ . When a laser of wavelength  $\lambda$  propagates through such an EOM of length  $l$ , it picks up phase  $\phi_{o,e}$ :

$$\phi = \frac{2\pi nl}{\lambda} = \frac{2\pi l}{\lambda} n_{o,e} - \frac{\pi l}{\lambda} n_{o,e}^3 r_{o,e} \frac{V}{d} = \phi_{o,e} + \phi_{o,e}^V(V). \quad (3.4)$$

Here all of the voltage dependent phase is grouped into  $\phi_{o,e}^V$ . When light leaves the EOM, it then goes to a polarization selective element (in our case, a PPLN for SHG) and the light on the ordinary and extraordinary axes is projected onto the axes of this crystal with angle mismatch  $\alpha_2$ . The field makes it through this effective polarizer with efficiency  $\eta = \frac{|\vec{E}_{out}|}{|\vec{E}_{in}|}$ , determined by

$$\eta = ae^{i(\phi_o + \phi_o^V)} + be^{i(\phi_e + \phi_e^V)}, \quad (3.5)$$

where  $a = \sin(\alpha_1) \sin(\alpha_2)$  and  $b = \cos(\alpha_1) \cos(\alpha_2)$ . The power that makes it through the polarizer is proportional to  $|E_{out}|^2 \propto |\eta|^2 = a^2 + b^2 + 2ab \cos(\Delta\phi + \Delta\phi^V)$ , where  $\Delta\phi^V = \phi_e^{(V)} - \phi_o^{(V)}$ . Consider now that the applied voltage has both a dc component  $V_{DC}$  and a component at the modulation frequency  $V_{RF} \sin(2\pi f_m t)$ . Then

$$|\eta|^2 = a^2 + b^2 + 2ab \cos(\Delta\phi + \Delta\phi_{DC} + M \sin(2\pi f_m t)) \quad (3.6)$$

$$= a^2 + b^2 + 2ab \sum_{k=-\infty}^{\infty} J_k(M) \cos(\Delta\phi + \Delta\phi_{DC} + 2\pi k f_m t) \quad (3.7)$$

where  $\Delta\phi_{DC} = \frac{\pi l}{\lambda d}(n_e^3 r_e - n_o^3 r_o)V_{DC}$  corresponds to the dc component of  $\Delta\phi^V$  and  $M = \frac{\pi l}{\lambda d}(n_e^3 r_e - n_o^3 r_o)V_{RF}$ , and  $J_k$  is the Bessel function of the first kind. It is the amplitude modulation at  $f_m$  that negatively effects our lock-in detection, so we must consider the terms in Eqn. 3.7 at  $k = \pm 1$ , recalling that  $J_{-1} = -J_1$ :

$$I_{1f} = 2abJ_1(M)(\cos(\Delta\phi + \Delta\phi_{DC} + 2\pi k f_m t) - \cos(\Delta\phi + \Delta\phi_{DC} - 2\pi k f_m t)) \quad (3.8)$$

$$= -4abJ_1(M) \sin(2\pi k f_m t) \sin(\Delta\phi + \Delta\phi_{DC}). \quad (3.9)$$

To eliminate the RAM which comes from this polarization mismatch, one must apply voltage such that  $\Delta\phi_{DC} = -\Delta\phi$ . Moreover, if there is RAM arising elsewhere within the experiment, a different  $V_{DC}$  can be applied to cancel that RAM by generating the opposite RAM from polarization mismatch. Thus, feedback to  $V_{DC}$  can be used to compensate for RAM. This feedback loop is setup by sampling the probe laser intensity as close to the atoms as possible, such that the RAM measured in-loop corresponds to the RAM at the atoms, locking-in on the modulation frequency, and sending the lock-in quadrature with the highest response to a PID servo to control  $V_{DC}$ .

Technically, this only eliminates the RAM that is in-phase with the frequency modulation. If the fm-spectroscopy lock-in is tuned such that it only receives the portion of the atomic response that is in-phase with the frequency modulation drive signal, then only in-phase RAM should effect the atomic lock. If this phase is imperfectly tuned, RAM which is out of phase (“quadrature RAM”) can also lead to clock frequency drifts. As described in Ref. [78], quadrature RAM can be stabilized via temperature feedback in much the same way that in-phase RAM is stabilized via bias voltage feedback.

### 3.2.4 Pressure Shifts

One major source of long-term instability in a hot vapor atomic clock comes from inter-atomic collisions. The most important for our consideration (in a well constructed rubidium vapor cell) are Rb-Rb collisions and Rb-He collisions. The theory for predicting the magnitude of these shifts is beyond the scope of this dissertation, but the important results from [79] are summarized in table 3.1, and the intrepid scholar may find more theory in the following sources [80–82].

Rb-Rb Self Collision Shift [MHz/Torr]	$-27 \pm 2$
Rb-Rb Linewidth Broadening [MHz/Torr]	$79 \pm 6$
Rb-He Shift [MHz/Torr]	$2.06 \pm 0.07$
Rb-He Linewidth Broadening [MHz/Torr]	$51.1 \pm 0.7$

**Table 3.1:** Table of important collisional shift parameters

Helium leakage can lead to linewidth broadening and long-term drift of clock frequency [54]. However, the most interesting platforms (to me) are compact, ground based clocks and satellite-borne clocks; the former will slowly equilibriate to a steady-state helium pressure, the latter will equilibriate to zero helium pressure. As such, we did not pursue mitigation of helium collision shifts. Best practice for future/commercial efforts would be to fabricate vapor cells out of aluminosilicate glass, which boasts orders of magnitude lower helium permeability than standard glass [83].

Rb-Rb self collision shifts are much more significant for our purposes, as the vapor pressure of Rb within the vapor cell is dependent not on slow diffusion from the environment, but rather from the much faster changes to the temperature of the vapor cell. From [84], we can expect the rubidium 87 pressure within the vapor cell to scale approximately as  $12.4 \mu\text{Torr}/\text{K}$  near  $100 \text{ }^\circ\text{C}$ . Given the Rb-Rb self-collision shift from [79], this means a  $330 \text{ Hz}$  shift per Kelvin, which is approximately  $1 \times 10^{-12}$  fractional frequency per Kelvin. Based on this slope, it would take an absolute temperature stability at the cold-point of our vapor cell of  $1 \text{ mK}$  to achieve a long-term fractional frequency stability of  $1 \times 10^{-15}$

### 3.2.5 *ac-Stark Shift*

The ac-Stark shift is one of the most pernicious effects on long-term stability of two-photon clocks. Since excitation of these transitions generally involves higher intensity than single-photon transitions, and (for this transition) the light involved is near-resonant to a single-photon transition ( $5S_{1/2} \rightarrow 5P_{3/2}$ ) to exploit near-resonant enhancement, the probe light which excites the clock transition has a measurable effect on the clock frequency [68, 85].

Consider, as our starting point, the well known result of the energy shift  $\Delta E$  for dressed states of a two-level Rabi oscillation [71, §7.7][86, §1.2.1]:

$$\Delta E = \frac{\hbar|\Omega|^2}{4\Delta} = \frac{|\langle 1|d|2\rangle|^2|E_0|^2}{4\hbar(\omega - \omega_0)} \quad (3.10)$$

for a light field  $E_0 \cos(\omega t)$  and two states  $|1\rangle, |2\rangle$  separated by energy  $\hbar\omega_0$ . This well known result is arrived at after taking a rotating wave approximation that will obfuscate matters for us. The more complete form of this equation is:

$$\Delta E = \frac{\omega_0|\langle 1|d|2\rangle|^2|E_0|^2}{2\hbar(\omega^2 - \omega_0^2)}. \quad (3.11)$$

For the purposes of calculating the shift on the energy levels of our clock transitions, it is necessary to consider fine splitting of the relevant energy levels; since our detuning from the closest state (1 THz) is much larger than any hyperfine splitting in rubidium-87, we will consider the hyperfine states as degenerate and only discuss shifts on states defined by  $|nlj\rangle$ . With the atomic fine states as our states of interest, the equation then becomes [87, §2.B.][88, §2.6.5]:

$$\Delta E_J = \frac{2}{3\hbar(2J+1)} \frac{\omega_0|\langle J|d|J'\rangle|^2|E_0|^2}{\omega^2 - \omega_0^2} = \alpha_J \frac{|E_0|^2}{4} = \alpha_J \frac{I}{2c\epsilon_0}, \quad (3.12)$$

where  $\alpha_J$  is defined as the ac-polarizability of the state  $|nlj\rangle \leftrightarrow |J\rangle$ ,  $J$  is the total electron angular momentum quantum number,  $I$  is the intensity of the optical field,  $c$  is the speed of light, and  $\epsilon_0$  is the permittivity of free space. This ac-polarizability is additive; if the state of interest  $|J\rangle$  couples to many different states  $|J'\rangle$ , the total polarizability is:

$$\alpha_J = \frac{2}{3\hbar(2J+1)} \sum_{J'} \frac{\omega_0 |\langle J|d|J'\rangle|^2}{\omega^2 - \omega_0^2} \quad (3.13)$$

For the purpose of a frequency standard, only the differential energy shift between the ground and excited state matters. Thus, the differential polarizability  $\Delta\alpha = \alpha_e - \alpha_g$  that determines the total energy shift

$$\Delta E = \frac{\Delta\alpha I}{2c\epsilon_0}. \quad (3.14)$$

We simulated the effective energy shift per  $\frac{\text{mW}}{\text{mm}^2}$  at various probe wavelengths, and plotted the results in Fig. 3.2. The transitions used to calculate this differential polarizability are listed in table 3.2

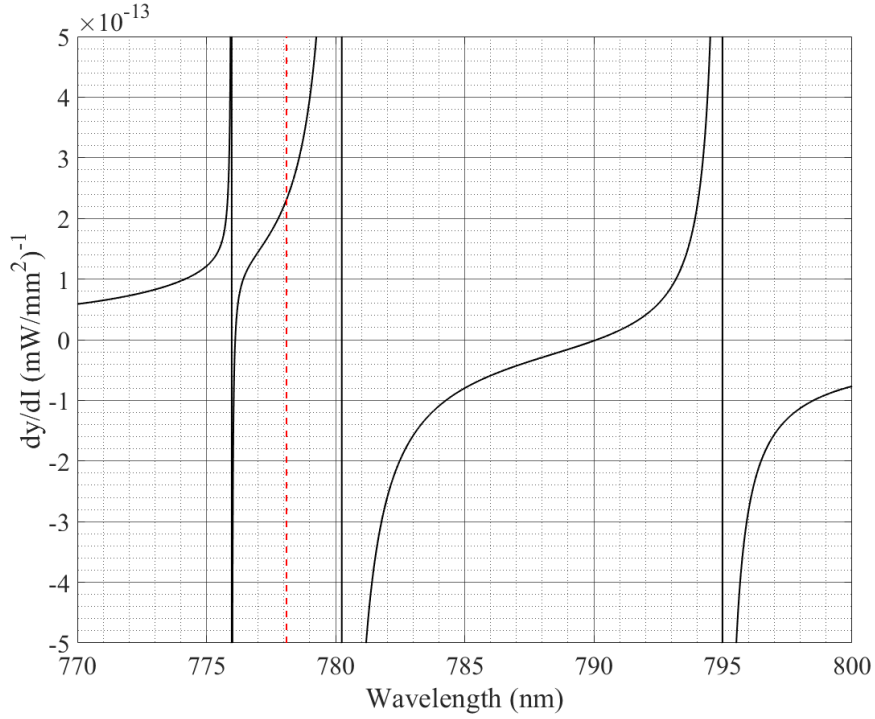


**Figure 3.2:** Theoretically calculated differential polarizability, in units of fractional frequency change per  $\text{mW}/\text{mm}^2$ . The location of a cw two-photon transition is shown with the red dashed line, indicating a shift of  $2.3 \times 10^{-13} (\text{mW}/\text{mm}^2)^{-1}$ , in agreement with [88]



Transition	Wavelength (nm)	$\langle J'   d   J \rangle$ (a.u.)
$5S_{1/2} \rightarrow 5P_{3/2}$	780.2415	5.978
$5S_{1/2} \rightarrow 5P_{1/2}$	794.9789	4.231
$5D_{5/2} \rightarrow 5P_{3/2}$	775.9786	1.98

**Table 3.2:** Table of relevant transition characteristics for calculating ac-polarizability, retrieved from [89]

### 3.2.6 Residual Stark Shift

From this simulation of wavelength dependent differential polarizability, an additional effect becomes apparent: if the center wavelength of our comb pulses drifts, so does the ac-Stark shift. This is not a factor for cw excitation, since being on resonance with the two-photon transition places a strict constraint on the laser frequency. For direct comb excitation, many different spectra can drive this transition, and those spectra may result in different ac-Stark shifts. This would mean a fluctuation in the Stark shift even for a constant intensity, even for a constant amount of fluorescence, so feeding back using either a photodiode or the PMT signal would not compensate for this “residual” Stark shift.

The most straight-forward way that this residual Stark shift may show up in our system would be in a drift of the center wavelength of our filtering fiber bragg grating. We measured a temperature coefficient of 5.8 pm/°C for our 75 GHz FWHM FBG. We then simulated the Stark shift for our frequency comb spectrum  $I(\omega)$ :

$$\delta\nu = \int \frac{\Delta\alpha(\omega)I(\omega)}{2c\epsilon_0} d\omega. \quad (3.15)$$

This calculation is represented visually in Fig. 3.3. To the best of my knowledge, this is the first description of such an effect, which could become a limiting instability in direct comb excitation based frequency standards. While we calculated based on a shift in the central wavelength of the spectrum equivalent to a change in temperature of our FBG, this residual Stark shift would also arise from a change in spectral shape, even if the center wavelength stays the same. A significantly different central wavelength or spectral distribution could also lead to decreased fluorescence which, if any offsets are present in the fm-spectroscopy locks, could also lead to clock shifts. However, the effect of changing fluorescence level on

clock frequency was measured to be orders of magnitude smaller than the predicted residual stark shift.

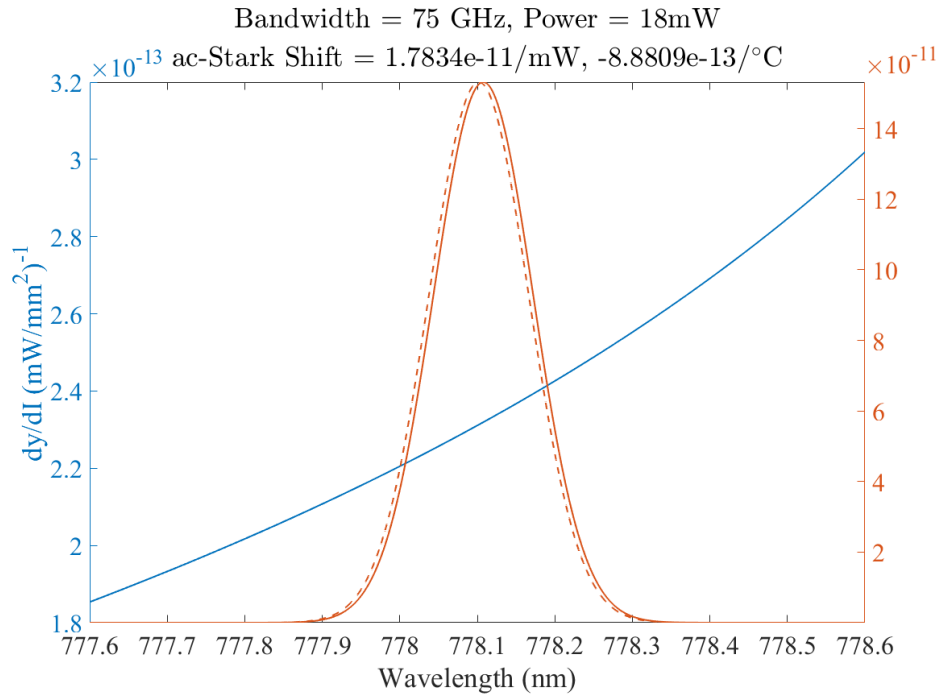


**Figure 3.3:** Demonstration of our calculations of residual Stark shift, showing a 75 GHz FWHM gaussian spectrum translating by 5.8 pm, which is approximately the change in center wavelength of our FBG for a 1°C temperature change.

Towards the question of reducing the effect of this residual Stark shift, we examined the effect of different spectral shapes and bandwidths, looking in each case at a change in central wavelength of 5.8 pm. The results for a gaussian spectrum and a square spectrum are shown in Figs. 3.4a and 3.4b respectively. The take-away from these plots is that increasing the bandwidth does not significantly decrease the residual Stark shift until the bandwidth is  $\gtrsim$  1 THz, which is about the detuning from the real intermediate states. Going to spectral bandwidths this large would have other undesirable effects on fluorescence volume §2.3.1 and residual Doppler broadening §2.3.2, so this is not a solution for us. Residual Stark shifts would be properly addressed by novel Stark mitigation techniques which we will discuss in the conclusion. Since miniaturized clocks may require these Stark mitigation techniques anyhow, this residual Stark shift may prove to be no real limitation, but in the meantime it is an effect worth characterizing.

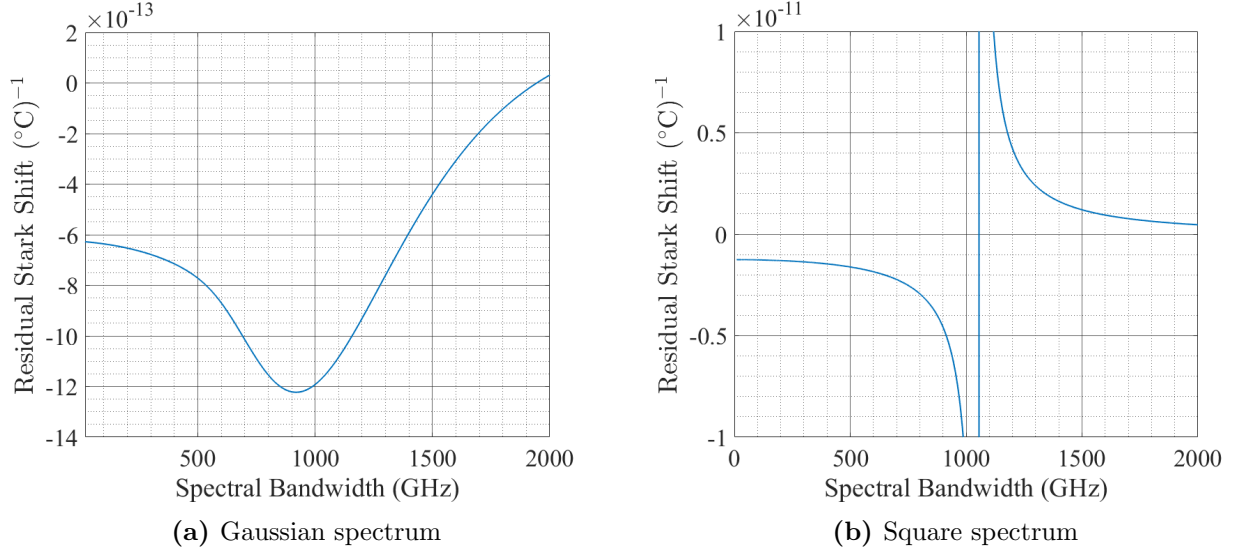


**Figure 3.4:** Residual Stark shift at various spectral bandwidths. Calculated for an incident power of 18 mW with a beam diameter of 250  $\mu\text{m}$ , realistic parameters for our experiment.

### 3.3 Isotope/Transition Selection

Before leaving the theoretical discussion and entering the practical clock design, there are a few more relevant notes; particularly, why choose  $^{87}\text{Rb}$  rather than  $^{85}\text{Rb}$ ? First, according to [50], the  $F=2\rightarrow 4$  transition in  $^{87}\text{Rb}$  has a higher line intensity than the most intense  $^{85}\text{Rb}$  transition ( $F=3\rightarrow 5$ ). Second, according to the calculations in [88, §2.3],  $^{85}\text{Rb}$  is about four times more sensitive to the second-order Zeeman shift than  $^{87}\text{Rb}$ .

What about the  $5S_{1/2} \rightarrow 7S_{1/2}$  transitions in rubidium 87? There would be some benefits to probing this transition over the  $5S_{1/2} \rightarrow 5D_{5/2}$  transition. By probing this transition with  $\sigma_+\sigma_-$  light, only states of equal  $m_F$  would be connected; this paired with the equal  $g_F$  of the ground and excited states results in zero first-order differential Zeeman shift. Additionally, only absorption of two counter-propagating photons will result in excitation, as parity selection rules forbid two  $\sigma_+$  or two  $\sigma_-$  photons from exciting this transition [43]. This removes the broadband Doppler background which contributes to the shot-noise in two-photon clocks.

The main reason that we have used the  $5D_{5/2}$  excited state instead of the  $7S_{1/2}$  is because the S-S transition has significantly lower near-resonant enhancement. The S-S transition requires two photons of 760 nm, which is about 10 THz detuned from the intermediate

$5P_{3/2}$  state, compared to the 1 THz detuning in the S-D transition. In the low excitation limit, fluorescence is quadratically proportional to both intensity and detuning (Eqn. 2.11); therefore, ten times more detuning means ten times the incident power to recover the same excitation level. For our experiment, this would mean generating over 200 mW of 778 nm light, which would require peak powers at 1556 nm that would threaten degradation of our waveguide SHG module and potentially result in nonlinear spectral broadening within our amplifiers. On the other hand, the ac-Stark shift is linearly dependent on intensity and quadratically dependent on detuning, so it may be worthwhile in the future to consider two-photon clocks with larger intermediate state detuning.

## Chapter 4

### Design Considerations and Clock Performance

#### 4.1 Design

Having (finally) established a sufficient theoretical background, now we shall turn to the practical, experimental overview. This explanation will be complicated by the fact that we built three separate frequency standards, each with its own idiosyncrasies. The reason for this is well summarized by Segal’s law: “A man with one watch knows what time it is. A man with two watches is never sure.” This is to say, any characterization of a clock must be a characterization relative to another clock. This can be expanded to more descriptive laws: “A man with one clock knows nothing about it. A man with two clocks knows how bad the worst clock is, but not which clock is the worst. A man with three clocks can tell you which is the worst and how bad it is.” This is a summary of the principle of the “three-cornered hat” method [7, §10.14] which we utilized to track down and eliminate sources of instability in each clock.

##### 4.1.1 *Laser systems*

The three systems described here will be labelled by their oscillators: the IMRA, the Vescent, and the RIO. The IMRA LH-250 erbium fiber frequency comb is a 250 MHz repetition rate figure-9 type oscillator. The Vescent FFC-CM erbium fiber frequency comb is a 200 MHz repetition rate oscillator, based on a linear cavity with semiconductor saturable absorber mirror (SESAM). The RIO PLANEX is our lone cw oscillator, a narrow-linewidth, single frequency diode laser. Since we wish to compare these clocks in the RF, another frequency comb with  $f_{rep} = 160$  MHz has a comb tooth phase-locked to the RIO, matching the conventional “gearwork” picture of a frequency comb (§1.2.3).

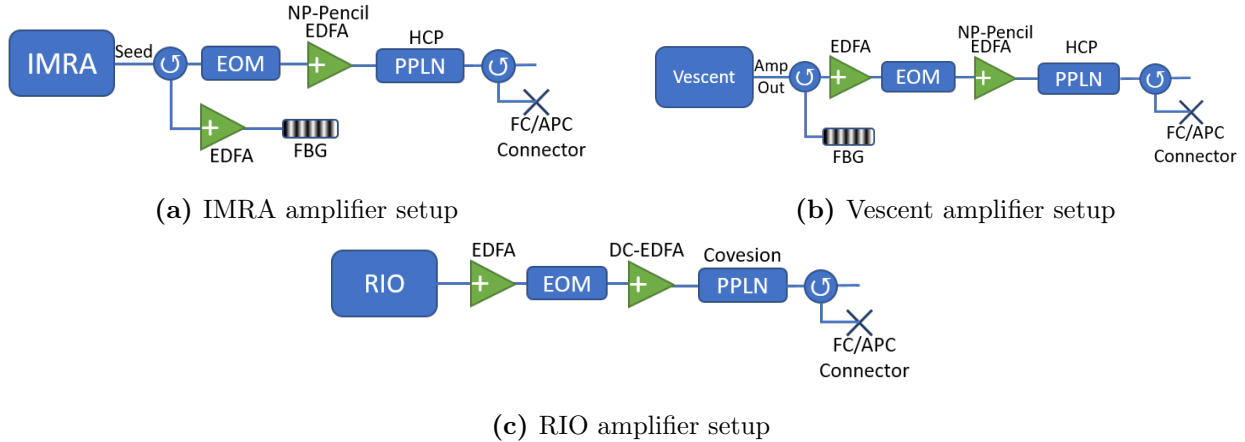


**Figure 4.1:** Fiber amplifier chain to produce enough 778 nm power to probe the two-photon transition. FBG: Fiber Bragg Grating, EDFA: Erbium-doped Fiber Amplifier, DC-EDFA: Dual-Clad EDFA, PPLN: Periodically-Poled Lithium Niobate.

Since all of these oscillators produce too little power for efficient second harmonic generation, they are all followed by a sequence of amplifiers. This setup is diagrammed in Fig. 4.1. A couple of details deserve special note. Each homebuilt erbium-doped fiber amplifier (EDFA) was constructed with IXF-EDF-HD-PM fiber, which is doped such that it absorbs 81 dB/m of 1530 nm light. This fiber was selected because it has normal dispersion ( $\approx 28,000 \text{ fs}^2/\text{m}$ ) and high gain. The normal dispersion helps to counter the anomalous dispersion of the passive PM-1550 fiber in the rest of the 1550 nm portion of the fiber setup. The high-gain helps to keep these gain sections short, which can minimize the nonlinear pulse evolution in the smaller core of the gain fiber.

In Fig. 4.1a, the first stage of amplification is double passed, with the FBG filtering before the second pass. The FBG is used to select a narrow portion of the frequency comb spectrum to avoid residual Doppler broadening and increase the fluorescence volume. Since amplified spontaneous emission within an amplifier can add significant frequency noise to a laser [90], it is important to properly saturate each amplifier in our setup – however, the light reflected from a narrow  $\approx 1 \text{ nm}$  FBG may lead to underseeding. Double-passing this amplifier ensures that the gain is always saturated, since the more intense unfiltered light makes the first pass. The second pass is seeded with the once-amplified filtered portion, which is then further amplified. This double-pass approach was not used on the Vescent system Fig. 4.1b, as the output of the oscillator provided enough power that, after filtering with the FBG, the first

EDFA was still seeded with about 150  $\mu\text{W}$ , which should be sufficient to seed this backwards pumped preamplifier.

The second EDFA in Figs. 4.1a and 4.1b is a high gain, short length, ‘‘Pencil Amplifier’’ designed by NP-Photonics. The theory was that the high peak powers after a second stage of amplification could lead to nonlinear effects (e.g. self-phase modulation and four-wave mixing) which might change the optical bandwidth and chirp in unintentional ways. Using a short-length amplifier immediately followed by second harmonic generation should limit the buildup of these nonlinear effects. If we were using femtosecond pulses, the common way to avoid such nonlinear effects is chirped pulse amplification (CPA) [91]. However, our 75 GHz FWHM bandwidth pulses with time duration  $\approx 6$  ps would require propagation through over 500 m of PM-1550 fiber (or total GDD of about 12 ps<sup>2</sup>) to significantly broaden the pulse duration, based on gaussian pulse propagation [92, §2.5]

$$\frac{\tau_p(L)}{\tau_p(0)} = \sqrt{1 + \left( \frac{4 \ln 2 \frac{\partial^2 k}{\partial \omega^2} L}{\tau_p(0)^2} \right)^2}. \quad (4.1)$$

Using either a long fiber amplifier or a long fiber to pre/post chirp the pulses would come with many potential negative effects, including polarization degradation, loss, accumulation of nonlinear effects, higher order dispersion, pulse-breakup, etc. While it would also be possible to achieve large pre/post chirps for CPA with a grating pair or chirped fiber-bragg grating, these each add some complexity at the miniaturization stage.

Our solution to this potential problem was to keep the amplifier and passive fiber length after amplification short. This is why we utilized the ‘‘pencil’’ amplifier, which provides all of the necessary gain within 0.3 m, and followed the amplifier immediately with the PPLN. We also tested a conventional amplifier made of 1 m of IXF-EDF-HD-PM erbium doped fiber and saw minimal spectral broadening up to 300 mW of average power at 1550 nm, so for the pulse-width and power used within the majority of this project, the pencil amplifiers may not be necessary. For future projects requiring higher peak power, the considerations above may prove to be of critical importance.

#### 4.1.2 Vapor Cell Holder Design

At the heart of this frequency reference is a  $^{87}\text{Rb}$  vapor cell. For this frequency reference to achieve comparable performance to a maser, a lot of consideration must go into the packaging of this vapor cell. The desiderata for a vapor cell holder are:

1. A precisely controlled cold point in the cell, with precision  $\leq 1$  mK
2. Uniform heating of the cell body to 100 °C
3. Magnetic shielding to  $\approx 1$  mG background magnetic field
4. Efficient collection of fluorescence photons onto a photomultiplier tube (PMT)
5. Small enough to share a shoe box with the other optics in our free-space section

To satisfy the first conditions, we utilized a vapor cell with a long fill-stem (1/2" diameter cell, 1/2" length fill-stem, 5 mm active length, from Precision Glassblowing) to enable separate control of the fill-stem as a cold point. To satisfy the other conditions, we settled upon a metal shell encasing the entirety of the vapor cell (excepting the fill-stem), with small holes for the counterpropagating probe beams, and a perpendicular hole for collecting fluorescence (Fig. 4.2). The small holes for the probe beams were off-center from the vapor cell windows by 4.5 mm, moved away from the fillstem and towards the collection hole to increase the solid angle of fluorescence collected. This shell was heated via flexible polyimide heaters, which were taped in a double layer, attempting anti-parallel flow of current through each heater and therefore minimal induced magnetic field. The shell and taped-on heaters were then wrapped in aerogel fabric to minimize convective temperature fluctuations.

If the reader considers designing their own two-photon, fluorescence based frequency standard, this is my biggest piece of advice regarding physics package design: get the bigger PMT. Months were spent with a 1x3 mm active area PMT, heads were scratched working out which large numerical aperture lenses would allow us to collect as much emitted light as possible, and steady hands spent hours optimizing throughput of collected light through this 1 mm aperture. Over a year into the project, we switched to a Hamamatsu H10721-110 PMT with an 8 mm diameter aperture and we measured over 200x increase in measured



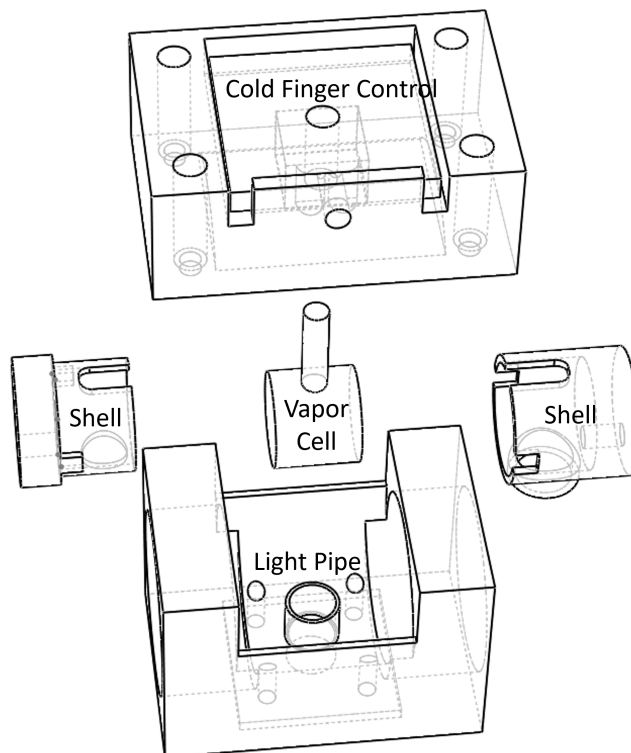


**Figure 4.2:** 3D model of the vapor cell holder. The shells interlock around the vapor cell to act as an integrating cylinder and provide uniform heating. The cold finger control fits over the fillstem of the vapor cell.

fluorescence. This PMT is also “blind” to the probe wavelength, with less than 100x the sensitivity at 778 nm than at 420 nm, allowing us to remove the 420 nm bandpass filter previously required before the PMT, allowing for more flexibility in design.

With this increased flexibility, we moved away from high NA lenses and toward light pipes. Aluminum has an unpolarized reflectance at 420 nm of  $>89\%$  for any angle of incidence, meaning an aluminum vapor cell shell makes an effective integrating cylinder, and an aluminum pipe makes an effective light pipe. We mated the 6 mm $\varnothing$  fluorescence capture aperture on the shell to a 7 mm $\varnothing$  aluminum pipe, which directs the light onto our 8 mm $\varnothing$  PMT.

To analyze this light collection scheme, we utilized FRED, a software for non-sequential ray tracing. We uploaded the 3D model of our vapor cell holder, modelled the fluorescence as a Lambertian source on the surface of an ellipsoid of length 0.74 mm (about the full width

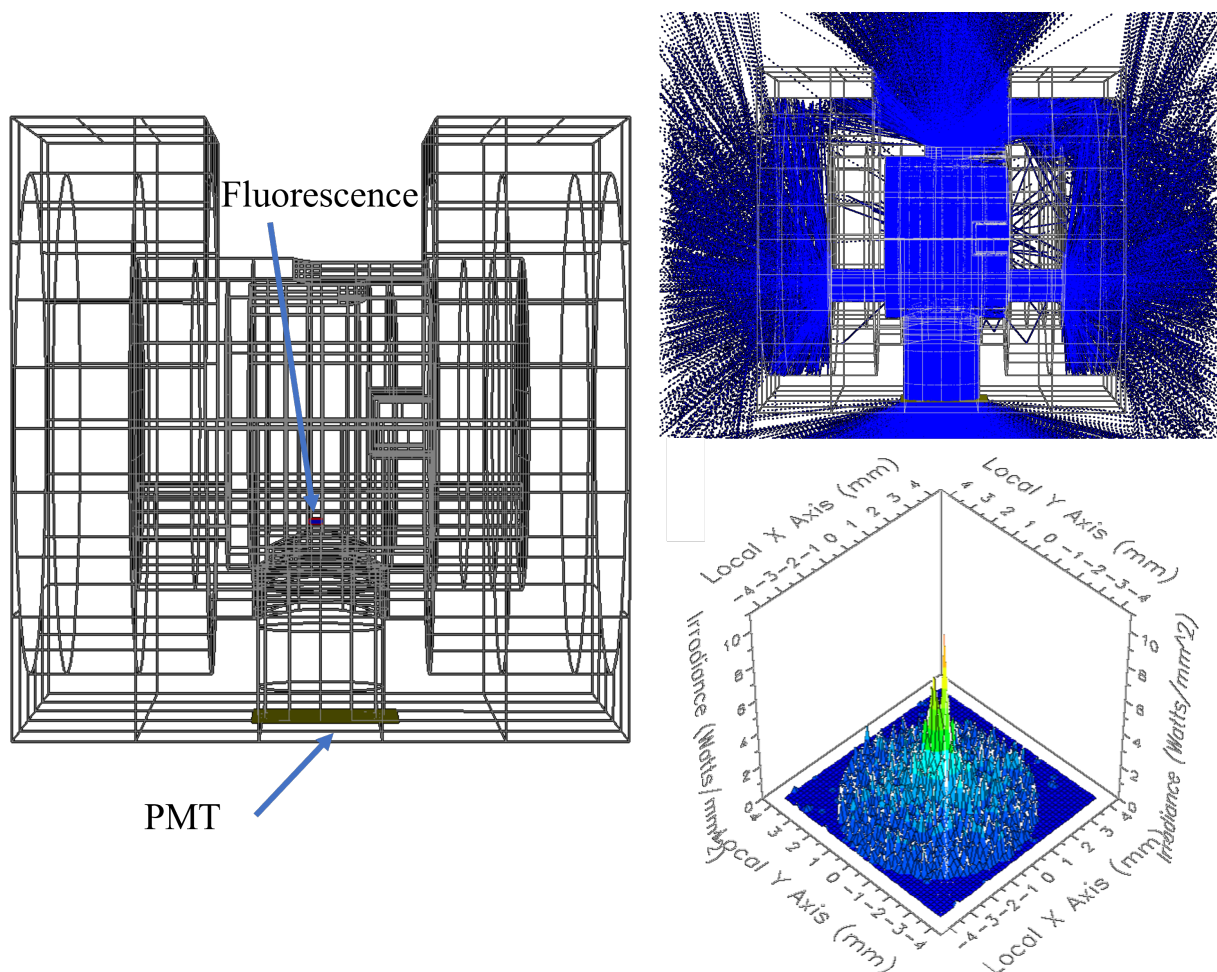


**Figure 4.3:** Modelling of fluorescence collection within the final vapor cell holder design. The shell was modelled as having specular, polarization independent reflectance of 92% or 54% for aluminum or mu-metal construction respectively. All other surfaces were modelled with reflectance of 92%. Collection efficiency is calculated by integrating over the irradiance profile (bottom right) measured at the PMT location.

at half max of a 75 GHz bandwidth pulse), and placed an analysis surface at the location of our PMT (see Fig. 4.3). We then traced 10,000 rays and evaluated the fraction of the power that arrived at the analysis surface. For an aluminum shell with an aluminum light pipe, 41.8% of the light emitted from the fluorescence orb was collected at the PMT. For a shell made of nickel (our analog for  $\mu$ -metal) with an aluminum light pipe, only 28% of the light was collected on the PMT, demonstrating that the aluminum shell has been acting somewhat as an integrating cylinder.

For all of the data within this dissertation, the approach has been to use an aluminum shell, for ease of prototyping and increased collection efficiency. Since this does very little by

way of dc magnetic field attenuation, we place the entire vapor cell holder and PMT within a 0.75 mm thick  $\mu$ -metal box. This is effective to reduce the magnetic field below the point where we see linewidth broadening ( $<100$  mG [88, §2.3]), but it is unclear how much the residual magnetic fields are affecting the long-term stability. To reduce this uncertainty, the next generation of this standard is replacing the aluminum shell with  $\mu$ -metal, and placing the entire assembly within a 1.5 mm thick welded  $\mu$ -metal box. The reduction in collection efficiency is a worthwhile trade-off to achieve certainty on magnetic shielding, especially as we seek to package this system in proximity to electronics which generate their own magnetic fields. For a future version, one could coat the inside of the  $\mu$ -metal shell with aluminum or silver to regain the benefits of higher reflectivity.

#### 4.1.3 Cold Point Control

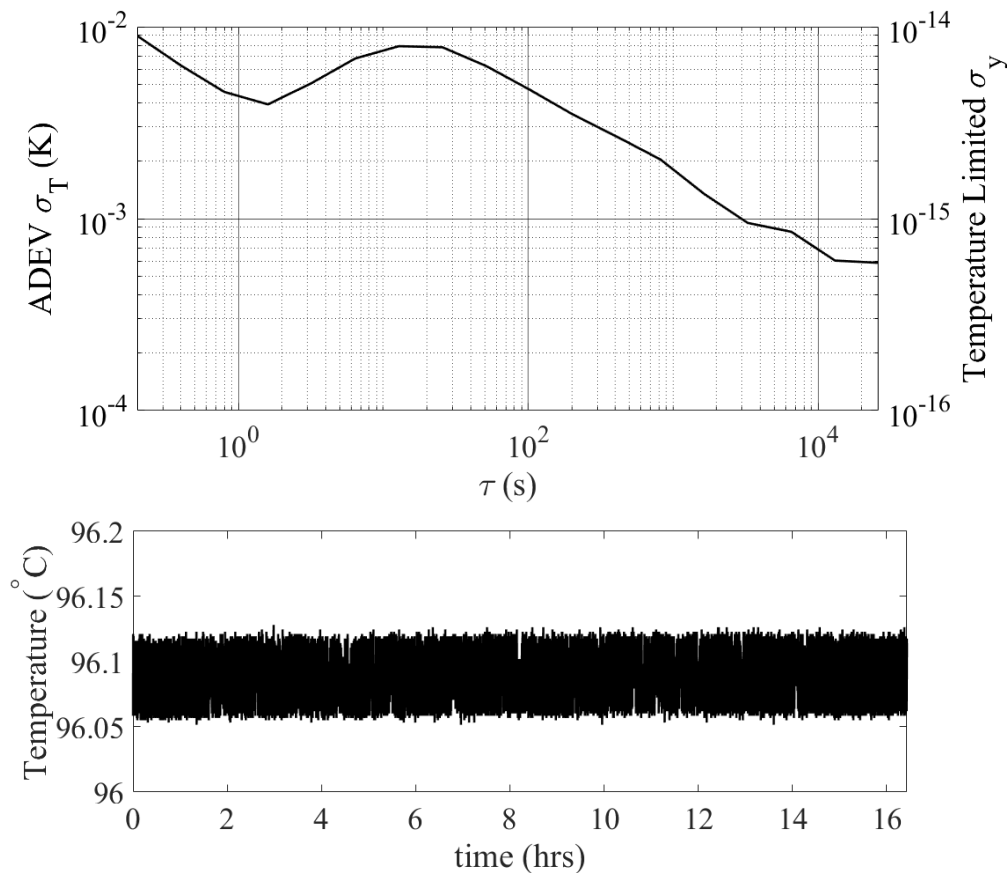


**Figure 4.4:** Cold point out-of-loop temperature monitor. The Allan deviation shows that at times longer than 3000 s we have temperature fluctuations lower than 1 mK.

To achieve cold point control, we machined a copper block to fit over the fillstem of the vapor cell. To hold this in place without placing strain on the delicate fillstem, we 3D-printed an adapter out of high-temperature resin, which is secured to the light-pipe assembly. We planted two 10k thermistors within the copper block, near the fill-stem hole, and a double coiled length of enamelled, small gauge wire on top of the copper block for resistive heating. We stabilize the cold-point temperature via a Wavelength Electronics HTC3000, and we monitor the out-of-loop thermistor for verification of thermal stability. The out-of-loop temperature stability we recorded in an overnight run gives us the temperature Allan deviation shown in Fig. 4.4. This temperature variance places a limit to the fractional frequency stability below  $10^{-14}$  at all times and below  $10^{-15}$  at times longer than one hour, based on the theory from §3.2.4.

The vapor cell holder for the cw reference is an earlier version, described here for completeness and not as a recommendation. It is an aluminum cylinder machined to hold the vapor cell, a lens, and two windows. The windows which are parallel to the input and output face of our vapor cell serve to trap heat, so that these faces of the vapor cell do not become the cold point of the cell. The lens helps to collect the fluorescence onto a PMT. These goals are better achieved by direct fillstem control and light pipes respectively. Although this design is not as good as the design described above, it has still enabled reasonable three-cornered hat measurements described in §4.5.3.

#### 4.1.4 Probe Geometry

Overlapping counterpropagating pulses in a hot rubidium vapor can be done through various optical setups. The simplest techniques are delayed pulse retroreflection, split pulse retroreflection, and Sagnac interferometry. A simplified schematic of each technique is shown in Fig. 4.5; the benefits, drawbacks, and some notes on each technique are discussed below.

Delayed pulse retroreflection is the most power-economical approach presented here. Every pulse contributes to fluorescence twice, as it passes once forwards and once backwards through the vapor. The drawback is that the delay arm must be  $c/2f_{rep}$  long (750 and 600 mm for 200 and 250 MHz  $f_{rep}$  respectively). This propagation length increases the potential for alignment induced instability [85, 88]. Any drift in delay arm length changes the posi-

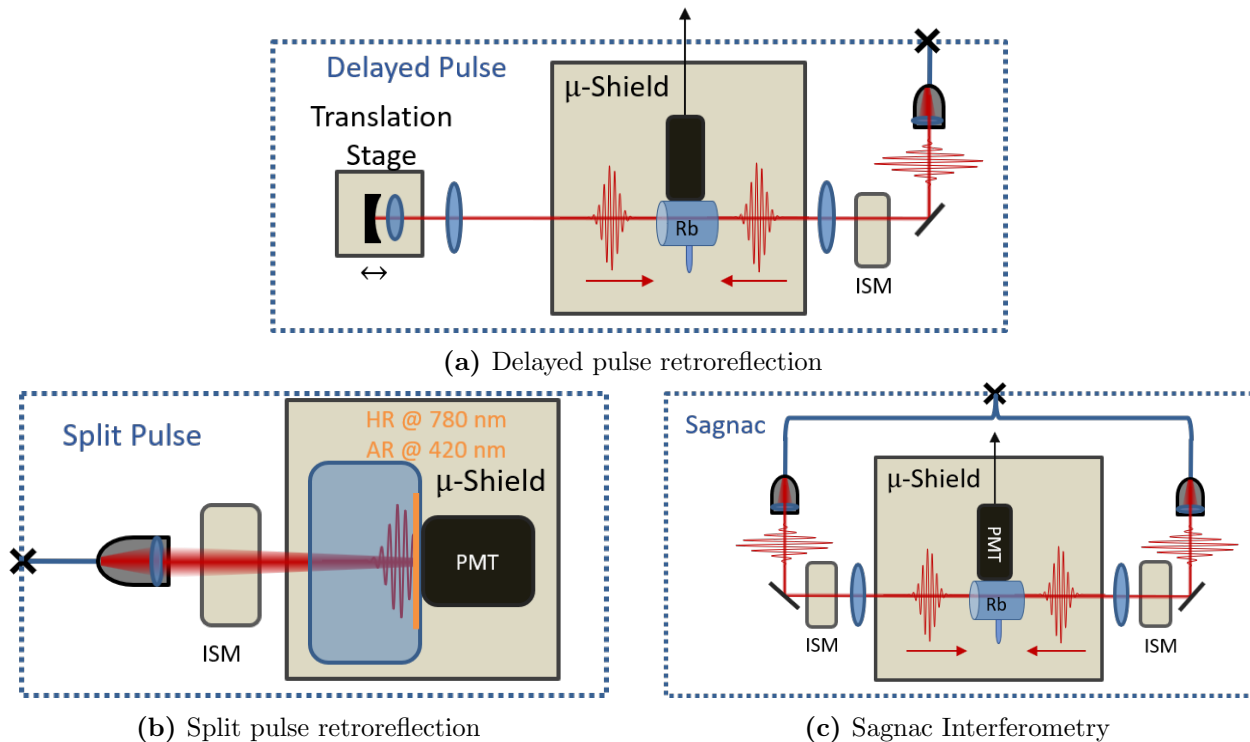


**Figure 4.5:** Possible schematics for achieving pulse overlap within the rubidium vapor cell. ISM: intensity stabilization module

tion of pulse overlap, which may decrease collected fluorescence or shift the overlap position away from the focus, which increases the transit time broadening from curved wavefronts [93, §3.4]. The large footprint is also a deal-breaker for miniaturization.

Split pulse retroreflection is the most compact approach. By retroreflecting off of the inside of the vapor cell, the only components necessary in the free space optical path are a fiber-optic focuser and the vapor cell, enabling spectroscopy setups as small as  $35 \text{ cm}^3$  [94]. This short free-space section reduces the sensitivity to alignment based drifts [88, §2.6.5]. The simplest setup consists of overlapping the front of an incoming pulse with the tail of the same pulse, but splitting the pulse into a dichroic pulse pair also presents interesting potential research directions (§5). The fundamental downside is a reduction in fluorescence for the same input power: this can be pictured as the retroreflector bisecting the fluorescence volume. This reduction in fluorescence is not, however, accompanied by a reduction in ac-Stark shift, meaning that a given shot-noise limited short-term instability will require proportionately tighter intensity control to achieve the same long-term performance.

A more practical note on split pulse retroreflection: this requires a rubidium vapor cell with an internal coating that is high-reflectance for 778 nm and low reflectance for 420 nm. There are currently no market options for purchasing such a vapor cell, although this is a rapidly developing marketplace. We worked with a company (Vapor Cell Technologies) developing this technology and acquired prototype vapor cells with the appropriate coatings. We were able to see the two-photon transitions resulting from direct comb excitation; however, the vapor cells had natural isotopic abundance and produced linewidths of  $\approx 6$  MHz with lower signal level than our standard vapor cells (Fig. 4.6).

The Sagnac interferometer is the *via media*; more compact than the delayed pulse approach, but not requiring internal dichroic coatings of the split pulse approach. Since this approach captures the whole fluorescence volume, it will share the shot-noise vs. Stark shift curve with delayed pulse, not the worse split pulse. The free-space section in this setup need only include two fiber focusers, with the vapor cell at the mutual focus, so there is good miniaturization potential. The drawback is the relative complexity of two input pulses: intensity fluctuations or RAM might not be equivalent between the two arms, so for completeness one should detect and stabilize the intensity and RAM for each arm independently. We constructed and characterized such a setup for a more commercialized, packaged system. We utilized two matched fiber focusers, which give a beam diameter of 200  $\mu\text{m}$  at 66 mm working distance. Early results with this spectroscopy setup are competitive with our larger breadboard design.

For most of this project and all of the relevant results, we utilized the delayed pulse approach. This approach made it easy to change experimental parameters (i.e. beam size, power stabilization method, vapor cell packaging) without major redesigns. A more complete schematic with notated lengths and part numbers is shown in Fig. 4.7. Using gaussian beam propagation from the collimator (beam diameter = 0.98 mm) through the first focusing lens, we expect a beam diameter at focus of 200  $\mu\text{m}$ . We also measured this with a translated razor edge, which resulted in  $250 \pm 50$   $\mu\text{m}$  beam diameter.

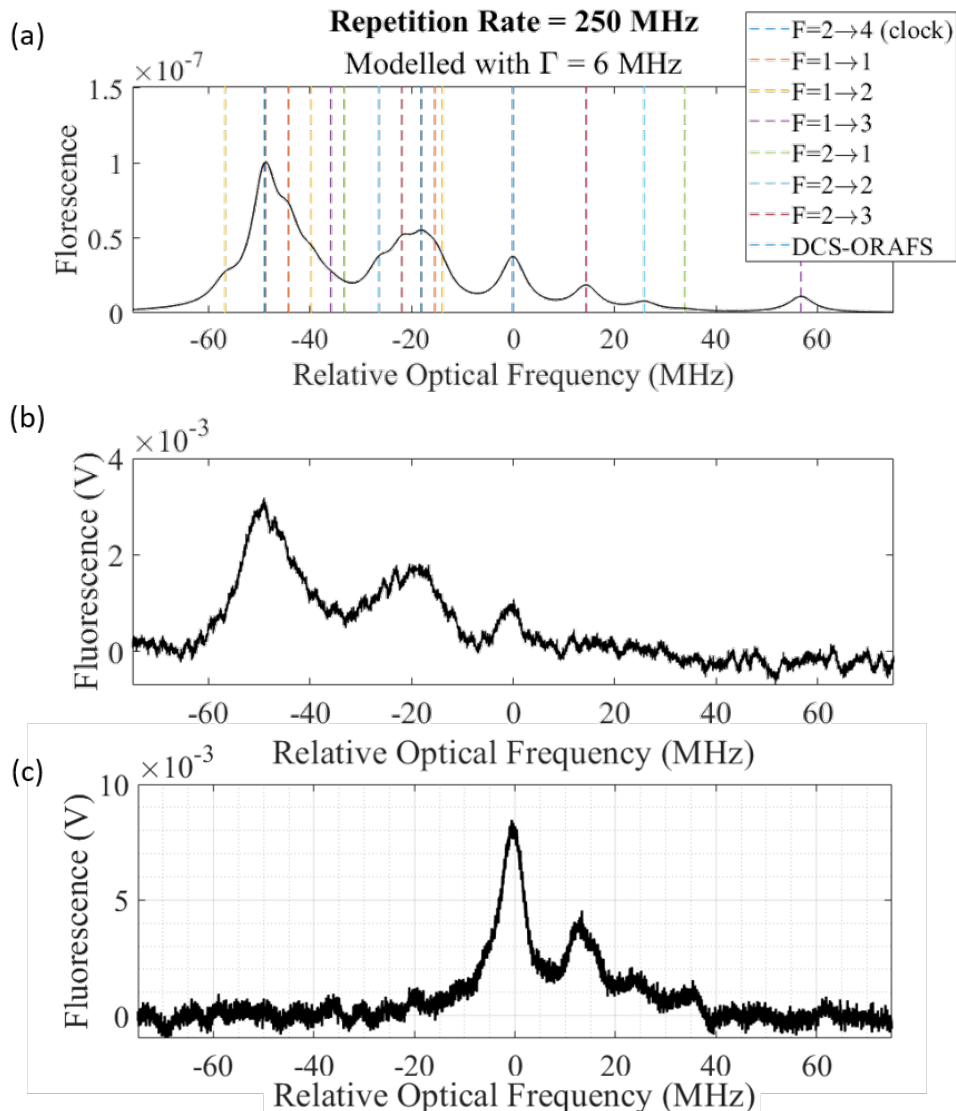


**Figure 4.6:** Two-photon spectra recorded from direct comb excitation of a miniaturized vapor cell, with AR/HR coatings depicted in Fig. 4.5b. The experimental direct-comb spectrum well (b) correlates to the theoretical spectrum (a) predicted for natural abundance rubidium, given a repetition rate of 250 MHz. The lack of isotopic enrichment and the  $\approx 6$  MHz linewidths make this vapor cell unusable as a frequency reference. (c) shows the same vapor cell probed with a cw laser.

#### 4.1.5 Pulse Width Considerations

We showed in §2.3.1 that longer pulses result in a lower shot-noise limit for the same probe power; therefore, it is critical to choose the correct optical filtering for this clock. At first glance, the answer seems to be “filter as tightly as possible”. Tight filtering not

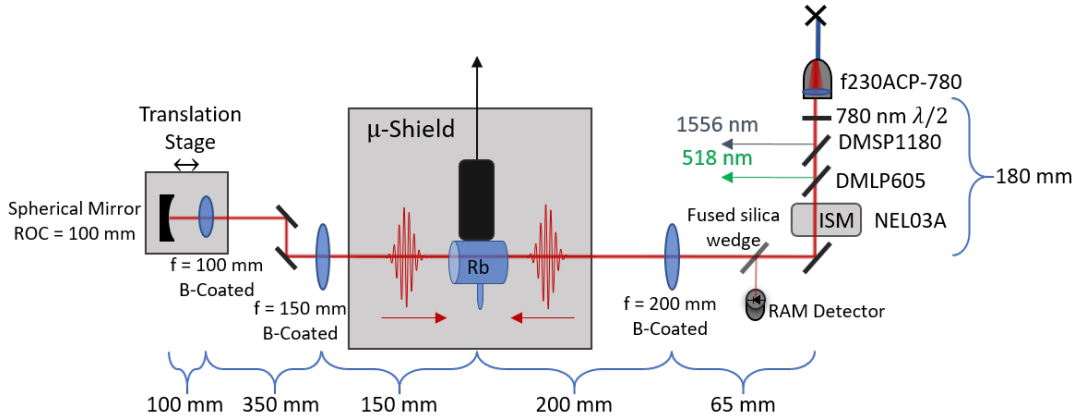


**Figure 4.7:** Detailed schematic of the breadboard spectroscopy setup used for the IMRA system. The Vescent setup is similar with the length between the second lens and translation stage increased to match the smaller  $f_{rep}$ . ISM: intensity stabilization module. DMSPP1180 and DMLP60 are dichroic mirrors which filter the fundamental 1556 and third harmonic 518 nm light out of the 778 nm probe beam.

only increases the excitation volume in the vapor cell, it also lessens sensitivity to chirp and nonlinear effects in the amplifiers, and reduces the residual Doppler broadening. There are, however, two main reasons that this cannot be our answer: 1. Narrow spectral filtering requires precise control of the filters 2. SHG is less efficient for a narrower spectrum.

We used three different fiber bragg gratings at different phases of this project, which had a FWHM bandwidth at 1556 nm of 1.6 nm, 0.8 nm, and 0.3 nm. These resulted in spectra at 778 nm with FWHM bandwidths of 249.8, 76.4, and 38.6 GHz respectively, shown in Fig. 4.8. The 1.6 nm bandwidth gratings were athermally packaged, quoted to 0.5 pm/K temperature sensitivity. The 0.8 nm and 0.3 nm FBGs were unpackaged, taped to a Peltier cooler covered in a silicon thermally conductive pad, and covered in aerogel insulation fabric to minimize sensitivity to room temperature.

To determine the best fiber bragg grating for our use, we compared the fluorescence collection efficiency for each FBG. We additionally tested the effect of adding dispersion via a chirped FBG with GDD 78.47 ps/nm =  $-1 \times 10^8$  fs<sup>2</sup> at 1556 nm, and a FWHM bandwidth of 1.6 nm. For the 0.3 and 0.8 nm measurements, this meant using a four-port circulator in the IMRA setup, as shown in Fig. 4.9, switching between the uniform 1.6 nm FBG and the chirped 1.6 nm FBG (reversing the direction of the chirped FBG to record both



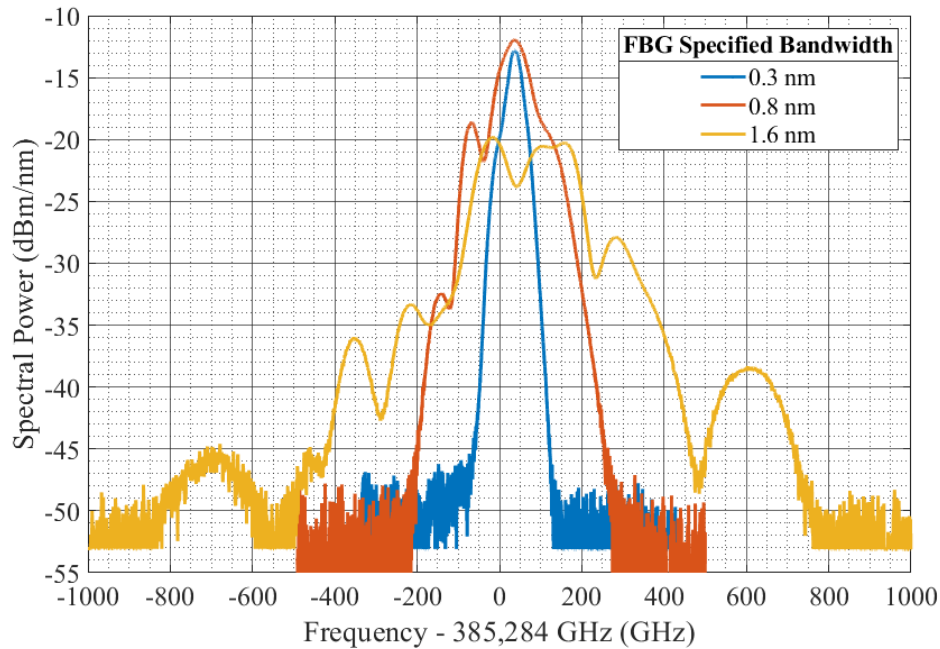


**Figure 4.8:** Optical spectra of probe light from IMRA oscillator with three different FBGs. Spectra are shown at centered at 778.1 nm = 385.284 THz. The resolution of the OSA is 0.07 nm = 35 GHz at this wavelength. The “0.3 nm” FBG measures a FWHM at 38.6 GHz, which may be limited by the instrument resolution.

normal and anomalous added chirp). For the 1.6 nm measurement, we used a three-port circulator as in Fig. 4.1a.

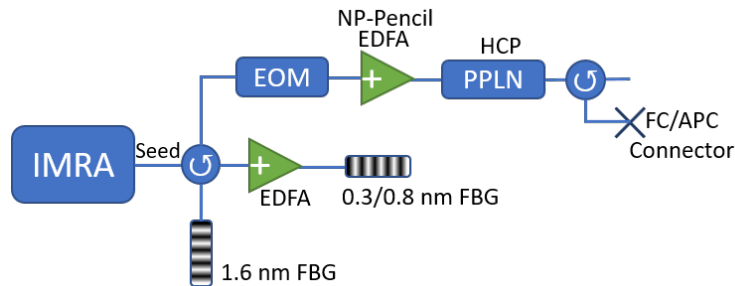


**Figure 4.9:** Setup for comparative measurements between the various fiber bragg gratings.

We measured a comparison between direct comb excitation and cw excitation for uniform, normal, and anomalous additional dispersion for each FBG bandwidth. The results of these nine measurements are shown in Fig. 4.10a. This confirms the conclusion from §2.3.1 that narrower FBGs result in larger fluorescence volume and therefore fluorescence detection

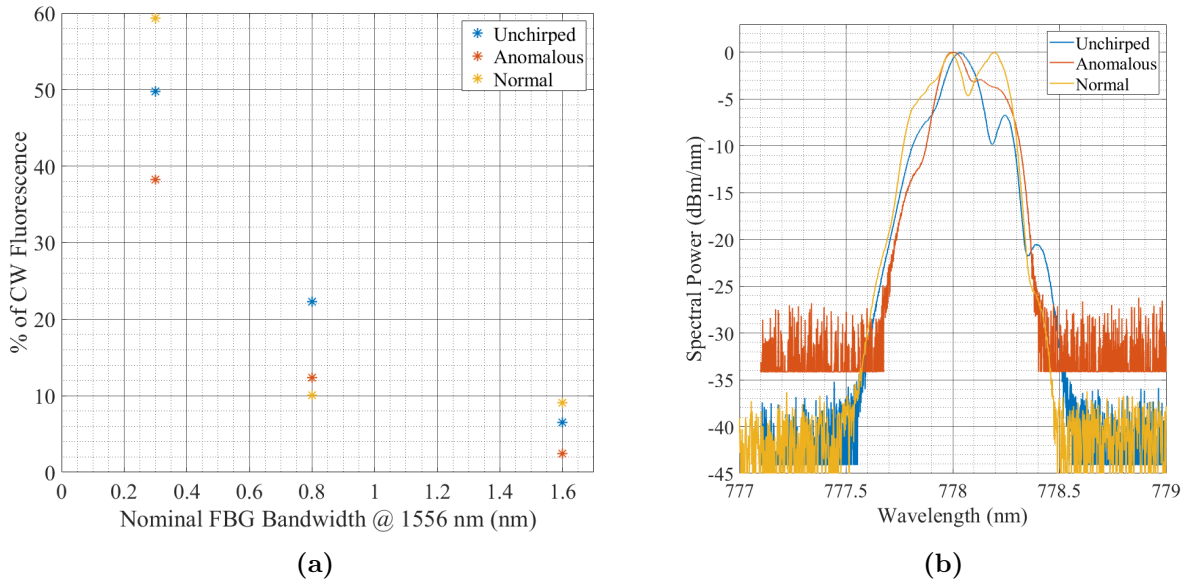


**Figure 4.10:** Comparative measurements between several fiber Bragg gratings, showing increasing fluorescence collection with decreasing bandwidth. (a) All FBG combinations compared to cw measurement on the same spectroscopy setup. (b) Spectra used for excitation with the 0.8 nm FBG. Distortion at the center of the normal dispersion spectrum may explain the outlier in (a).

which is more comparable to cw. In both the 0.3 nm and 1.6 nm cases, the normal dispersion produced the most excitation, potentially indicating a net anomalous dispersion in the rest of the amplifier chain. The low fluorescence in the normal dispersion 0.8 nm FBG may arise from the dip in the spectrum shown in Fig. 4.10b. The most efficient excitation was from the normally chirped 0.3 nm FBG, resulting in almost 60% of the cw fluorescence at the same average power.

#### 4.1.6 RAM Stabilization

Throughout the course of this experiment, we actively stabilized in-phase RAM via feedback to the bias voltage on the waveguide EOM as described in §3.2.3. For all of the results in §4.5.3, this was accomplished by introducing a glass wedge directly before the first lens and directing one of the reflections onto a photodiode. This photodiode had its response dc-blocked, amplified, and lock-in detected by the same fpga based lock-in/servo used for the atomic lock. For the packaged, compact, Sagnac setup, we dissected the intensity stabilization module (ISM) (Thorlabs NEL03A) and placed an additional photodiode opposite of

the internal photodiode. This additional photodiode measures the sampled beam that enters through the “output” port of the ISM; the current is trans-impedance amplified before being sent to the same lock-in/servo. We have seen comparable results between these two methods.

We passively stabilized the quadrature RAM via keeping the temperature on the EOM stable. Future work may benefit from active feedback to remove quadrature RAM.

## 4.2 Detection Electronics

Once two frequency combs have  $f_{rep}$  stabilized to their respective atomic references and  $f_{CEO}$  stabilized with an f-2f lock, stability analysis should be a simple matter of detecting  $f_{rep}$  and feeding it into a phase noise analyzer with a suitably low noise floor. The reality is, of course, never that simple. Our phase noise analyzer (Microsemi 53100a) requires a signal at -5 to +15 dBm, between 1 and 200 MHz. For analyzing the Vescent oscillator ( $f_{rep}=200$  MHz) or our cw oscillator (locked to a comb with  $f_{rep}=160$  MHz), this simply required a sequence of low noise amplifiers and filters. Our IMRA oscillator ( $f_{rep}=250$  MHz), on the other hand, required external frequency conversion.

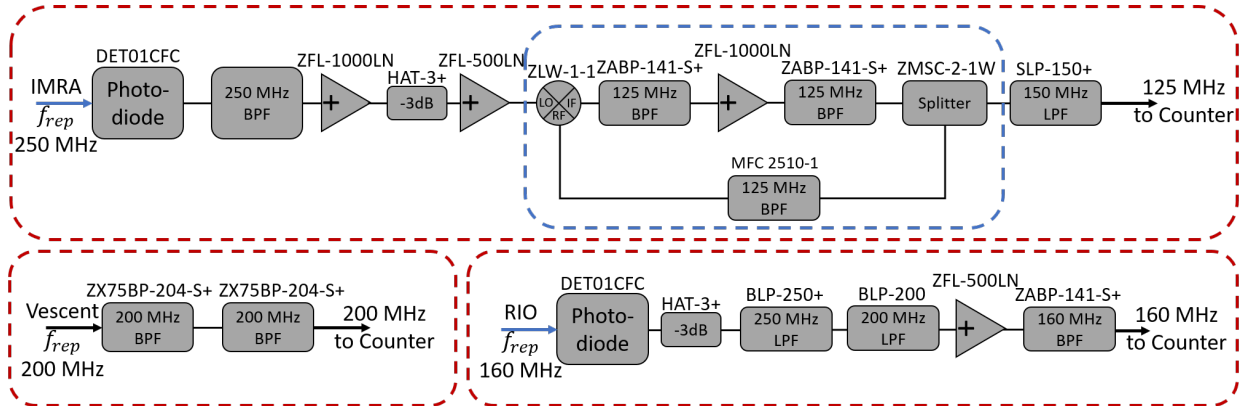


**Figure 4.11:** RF electronics required to compare the  $f_{rep}$  of our three clocks. RIO  $f_{rep}$  is actually a tap from the AOSense 160 MHz frequency comb which has a comb tooth phase-locked to the RIO clock laser. All part numbers are from Mini Circuits except DET01CFC (Thorlabs) and MFC2510-1 (Microwave Filter Corp.). The electronic loop circled in blue is the regenerative divider for converting 250 MHz to 125 MHz.

While digital frequency division is trivial, digitizing the  $f_{rep}$  signal in such a way that

digitization jitter does not significantly degrade the instability of this clock signal is less trivial. For that reason, we built an analog regenerative divider, per Ref. [95]. The full detection chain is represented in Fig. 4.11. It was of critical importance that each component utilizes SMA connectors properly torqued; a similar chain constructed with BNC connectors was mechanically sensitive, turning any movement of the cables into a source of frequency instability.

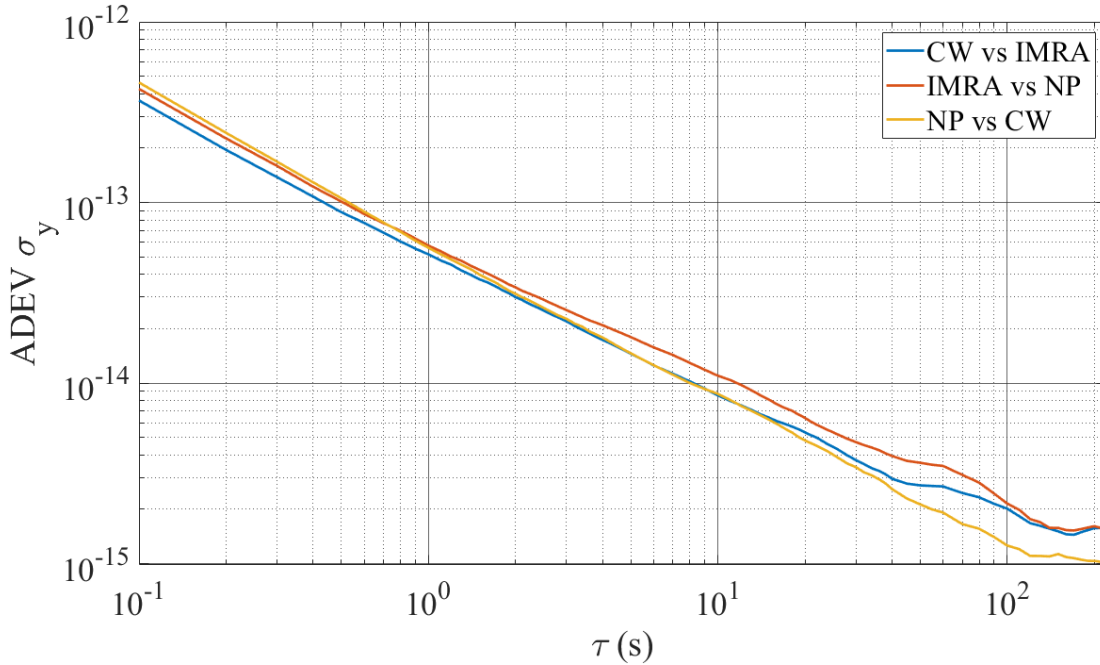


**Figure 4.12:** Measurements between each pair of frequency references, all locked to a common cw reference. This measurement indicates the noise floor of the detection chain diagrammed in Fig. 4.11

To test the detection limited instability, we locked both the 200 MHz Vescent oscillator and the 250 MHz IMRA oscillator to the same cw laser. With  $f_{CEO}$  of each oscillator locked, any drift in the common cw laser will turn into drift on the  $f_{rep}$  of the two combs (see Eqn. 1.6); however, this drift will be proportional between the two combs and therefore will not be measured if we use one  $f_{rep}$  as a reference to track the phase of the other  $f_{rep}$ . Thus, only the difference in the two detection chains should show up as instability in such a measurement. This was then used to optimize the selection of the RF electronics that became Fig. 4.11 and the resulting detection noise floor is shown in Fig. 4.12. This detection

noise floor should not interfere with measuring our homebuilt clocks, where our goal is for  $\sigma_y \approx 1 \times 10^{-13}$  at 1 second.

Another important variable is the inherent noise of the trans-impedance amplifier (TIA) for converting the small current from the PMT into a useful voltage. For much of this project, the TIAs we used were the DLPCA-200 and DHPKA-200 by FEMTO. Both provided enough bandwidth for locking in on the first harmonic when modulating at 200 kHz, where we minimize the intermodulation noise §3.2.2. There is a trade-space between current amplification within the PMT, which can be adjusted by changing the dynode voltage, and trans-impedance amplification at the TIA, which has switchable gain. We found the important figure-of-merit to be the voltage equivalent noise (VEN), found by multiplying the current noise spectral density [A/ $\sqrt{\text{Hz}}$ ] by the trans-impedance gain [V/A]. By switching the gain settings on the FEMTO DHPKA and compensating with dynode voltage to keep the lock-in signal the same size, we measured the dependence on VEN shown in table 4.1. This test showed a significant increase in instability for an increase from 18 to 48 nV/ $\sqrt{\text{Hz}}$ . Thankfully, the Koheron TIA100 has VEN of 10 nV/ $\sqrt{\text{Hz}}$  in a small package, and we saw no change in 1 s allan deviation changing from the FEMTO DLPCA-200 to the TIA100. Because of the smaller form factor and smaller VEN, the Koheron TIA100 is our current choice of TIA. If future efforts attempt to push this clock beyond  $\sigma_y = 1 \times 10^{-13}$  at 1 second, a lower VEN TIA may be necessary.

TIA Gain	$10^4$	$10^5$	$10^6$
VEN [nV/ $\sqrt{\text{Hz}}$ ]	18	48	140
$\sigma_y(1 \text{ s}) \times 10^{13}$	1.59	2.00	2.63

**Table 4.1:** Dependence of inherent TIA noise at different trans-impedance gain settings.  $\sigma_y$  is a two-clock allan deviation recorded at 1 s with a factor of  $\sqrt{2}$  removed to imply the limit to single clock stability.

### 4.3 Phase Noise Measurements

Since intermodulation noise (§3.2.2) can place a fundamental limitation on the stability of a continuously probed frequency standard, it is worthwhile to measure the frequency noise of our probing frequency combs. As established in Eqn. 1.2, a frequency comb has two degrees

of freedom:  $f_{CEO}$  and  $f_{rep}$ . Which of these is the relevant frequency noise to consider for intermodulation noise? Interestingly, neither; the relevant frequency noise is  $S_\nu(\nu_n)$ , the frequency deviations on the optical comb teeth which excite the transition.

Measuring  $S_\nu(\nu_n)$  requires a frequency discriminator to convert optical frequency fluctuations to voltage fluctuations which can be more easily measured with laboratory electronics. One common method for this is through Pound-Drever-Hall locking to an optical cavity [96]. For measuring an optical frequency comb, this is potentially complicated by the difference between the free-spectral range of the reference cavity  $\Delta\nu_{FSR}$  and the repetition rate of the frequency comb  $f_{rep}$ . If either  $f_{rep} = \Delta\nu_{FSR}/n$  (every comb mode corresponds to a cavity mode) or  $\Delta\nu_{FSR} = f_{rep}/n$  (every cavity mode corresponds to a comb mode), then the Pound-Drever-Hall error signal works very similar to the cw case. However, if such a cavity that matches the comb  $f_{rep}$  is unavailable, the resultant error signal is potentially much more complicated.

An alternative is to use the atomic fm-spectroscopy error signal as our discriminator. This is a natural approach, as our atomic lock is already based on turning frequency deviations of the probing comb teeth into a voltage with linear, zero-crossing slope about the line center. The problem with this technique is that the shot noise from 420 nm detection also shows up on the discriminator signal, often obscuring the laser phase noise in frequencies of interest.

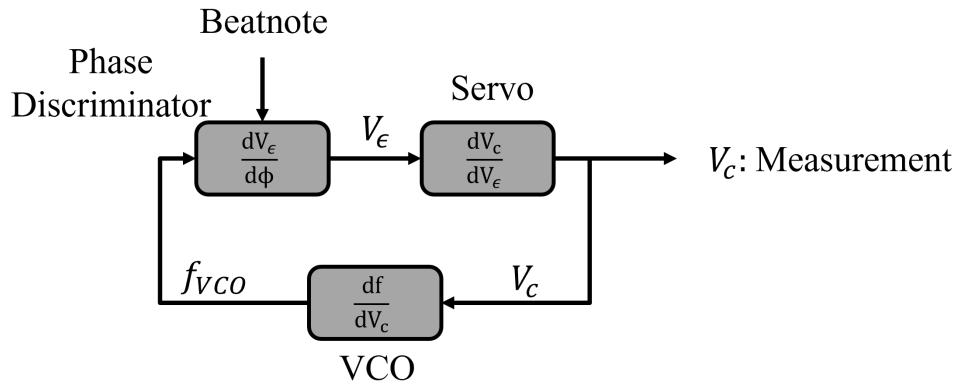


**Figure 4.13:** Setup for measuring the frequency comb optical frequency noise

Our eventual frequency noise discriminator was the actuator voltage on a phase locked loop (PLL), as described in reference [97], diagrammed in Fig. 4.13. This technique requires

a beatnote between the frequency comb and a cw laser, and consequently measures the relative frequency noise between these lasers. Ideally, this measurement would utilize a cw laser with significantly smaller frequency noise than the comb under test, such as a cavity prestabilized laser, such that the relative frequency noise measures the comb predominantly. Our measurement used the 1556 nm lasers that we had on hand, i.e. a RIO Planex laser and an NP-Photonics Rock. Both of these lasers should be intrinsically lower frequency noise than either frequency comb, so the measurement should be dominated by frequency fluctuations of the latter.

The measurement technique is to phase-lock a voltage controlled oscillator (VCO) to the beatnote between these two lasers, then look at the steering voltage of the VCO multiplied by the actuator slope [Hz/V] to capture the frequency deviations that the VCO is tracking. A Vescent D2-135 contains the VCO, servo, and phase discriminator required for this setup, and allowed lock bandwidths over 1 MHz.

Both to prevent the frequency noise from diverging at very low frequencies and to stay within a linearly calibrated actuator slope on the VCO, we used a Red Pitaya phase lock [32] feeding back to a given frequency comb's  $f_{rep}$  to keep the beatnote frequency constant. We recorded the phase noise with this Red Pitaya lock as a single integrator with a 10 Hz zero crossing, a 1 kHz zero crossing, and with enough PI<sup>2</sup> gain to achieve a sub-radian phase lock. By comparing these results for a given comb, we could see the effect of this first phase lock on the measured phase noise. For the results displayed here, we utilized proportional and integral gain, with the PI corner set to 100 Hz, and the proportional gain lowered until the measured noise level at frequencies higher than 1 kHz did not change (i.e. the phase lock is not effecting our measurement of phase noise).

The results of these measurements are shown in Fig. 4.14. By integrating all frequency noise from 20 Hz to the  $\beta$ -separation line crossing [98], we find the full-width at half max (FWHM) linewidths of the IMRA and Vescent to be 7.5 kHz and 13.7 kHz respectively. The intermodulation limited instability §3.2.2 in this setup is

$$\sigma_{IM} = \frac{\sqrt{S_y^{778}}}{2\sqrt{\tau}} = \frac{\sqrt{S_\nu^{1556}}}{\nu^{778}\sqrt{\tau}}, \quad (4.2)$$

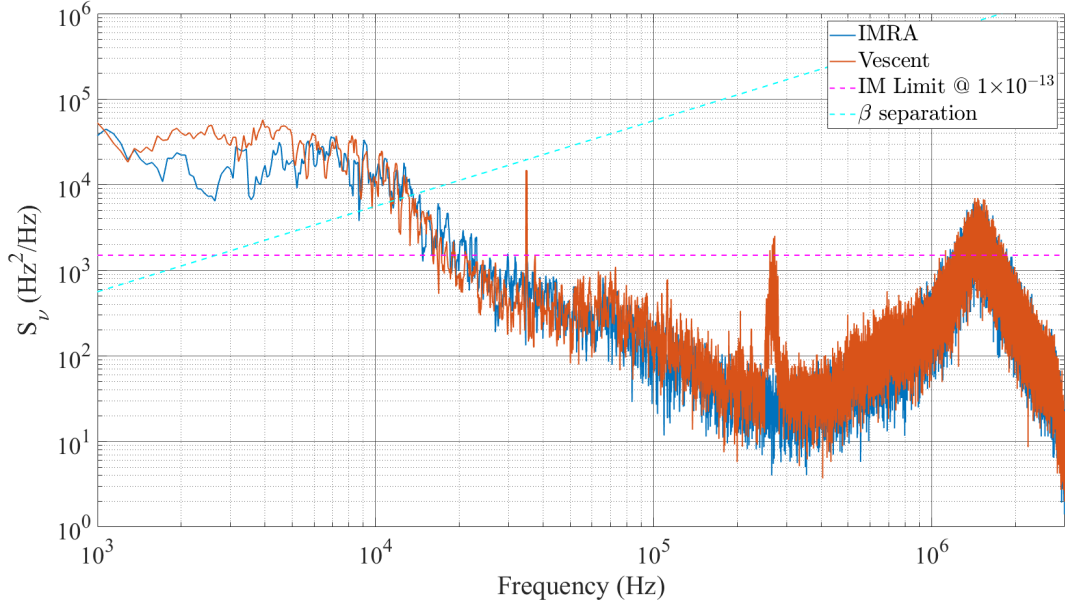


**Figure 4.14:** Relative frequency noise for a beatnote between a RIO Planex laser and the IMRA (blue) and Vescent (orange) frequency combs. The  $\beta$ -separation line (green) and level of frequency noise where intermodulation noise limits the one second allan deviation above  $10^{-13}$  (magenta) are also shown. The PLL bandwidth limit this measurement to below 1 MHz; this is the source of the large peak at 1.2 MHz and the immediate drop in detected noise beyond the loop bandwidth.

arrived at via the relationship  $S_y = S_\nu/\nu^2$  and recognizing that the frequency noise amplitude at the SHG 778 nm will be double what we measured at 1556 ( $S_\nu^{778} = 4 \times S_\nu^{1556}$ ). The most important thing to note is that above 100 kHz, both lasers have frequency noise at  $\approx 2 \times 10^3$  Hz<sup>2</sup>/Hz, which corresponds to an intermodulation limit of about  $1.2 \times 10^{-13}$  at 1 s. We modulate at about 200 kHz, which means we benefit from low frequency noise at 400 kHz on both oscillators. The large spikes on the Vescent oscillator appear to be from acoustic noise.

Interestingly, these oscillators have very different  $f_{CEO}$  linewidths and corresponding frequency noise  $S_\nu^{CEO}$  (Fig. 4.15). These measurements were made while locked with a 10 Hz integrator and no proportional gain; this integrator kept the measurements within range without suppressing any phase noise in the frequencies we are measuring. We measure a linewidth (defined by integrating the frequency noise above the  $\beta$ -separation line [98]) of 7.5 kHz for the IMRA oscillator and 85 kHz for the Vescent oscillator. This makes sense, as the instantaneous virtual saturable absorber of the non-linear phase shift in a figure-9 laser like the IMRA should result in a narrower  $f_{CEO}$  linewidth than the slower real SESAM in the



Vescent oscillator [10]. However, the broader linewidth of the Vescent  $f_{CEO}$  does not result in higher phase noise of the optical comb tooth, and these oscillators should have similar intermodulation limited instability.

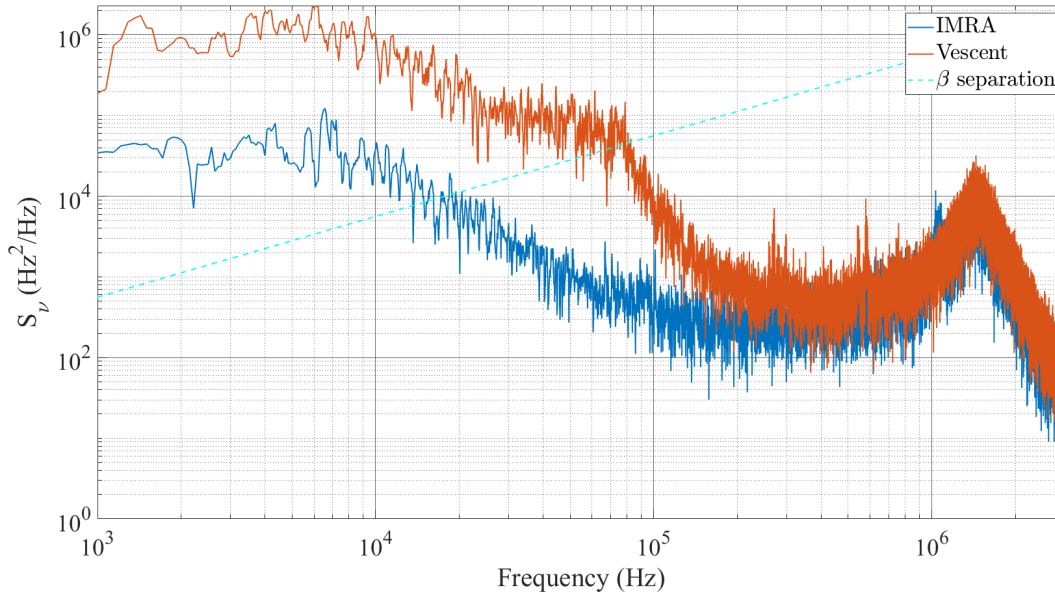


**Figure 4.15:** Frequency noise on  $f_{CEO}$  for each oscillator.

There are several potential approaches to lowering this intermodulation limit. In recent years the passive frequency noise performance of commercially available telecom lasers has dramatically improved. For example, the Thorlabs ULN15TK would enable an intermodulation limit at  $2 \times 10^{-14}/\sqrt{\tau}$  (assuming frequency modulation at 50 kHz). Compact Brillouin lasers have been made which would enable an intermodulation limit at  $5 \times 10^{-15}/\sqrt{\tau}$  [99–101]. The stability of these cw lasers can be transferred to frequency comb tooth stability through tight phase-locking (with a servo bandwidth greater than twice the modulation frequency), using the narrow-linewidth laser as the pump for an electro-optic frequency comb, or through Kerr-induced synchronization of a micro-comb [102].

#### 4.4 Stark Shift Mitigation

Since the ac-Stark shift (§3.2.5) can result in frequency instability, it is critical to long-term clock performance to mitigate this shift. The most straight-forward approach is simply

to stabilize the intensity of the probe light. Indeed, this is the approach which we used for the majority of this work, and for all of the data presented in our results §4.5.3. We utilized packaged intensity stabilization modules (ISMs) (Thorlabs NEL03A) to minimize the experimental footprint - additionally, in our packaged clock, these ISMs will benefit from the temperature stabilization of the entire physics package. Alternatively, the detected fluorescence on the PMT can be stabilized. Either approach suffers from drifts in the responsivity of the detector and the voltage reference, as well as alignment induced Stark shift [85] and residual Stark shift (§3.2.6). As miniaturized clocks require ever smaller fluorescence volumes and consequently higher intensity, all of these sensitivities will be increasingly detrimental to clock performance.

This has led to a desire for a more sophisticated approach to stabilizing the ac-Stark shift. One approach [103] involves varying the probe laser intensity and using the resulting variation in clock frequency to stabilize the total ac-Stark shift. This has considerable appeal but has yet to be experimentally implemented in a hot vapor cell atomic clock. Another approach utilizes two colors with differential polarizabilities of different sign, such that a proper balancing eliminates the Stark shift. This has been suggested as either probing with two colors which add to the energy level spacing  $\hbar\nu_{ge}$  [68] or using one probe laser at  $\nu = \nu_{ge}/2$  and one “mitigation” laser at a proper wavelength (such as 785 nm) [85].

We attempted a combination of the mitigation laser approach with the co-modulation technique from [68], diagrammed in Fig. 4.16. Since 785 nm “mitigation” light shifts the clock frequency in the opposite direction of the 778 nm clock laser, cancelling the Stark shift is a matter of ensuring that there is  $\approx 2.9$  times as much 785 nm light as 778 nm light at the atoms. To determine whether we have the proper level of mitigation light, we modulated the attenuation of both the mitigation and the clock light at a frequency  $f_{VOA} \ll f_m$  through a common variable optical attenuator (VOA). If the level of mitigation light is proper to cancel the ac-Stark shift, this mutual intensity modulation will result in no shift in clock frequency. If the mitigation light intensity is not correct, the transition frequency will be modulated at  $f_{VOA}$  and the servo will apply a correction voltage to the probe laser to track with this moving transition frequency. Thus, by locking-in on the clock servo output at  $f_{VOA}$ , the mitigation laser intensity can be stabilized to cancel the total ac-Stark shift.

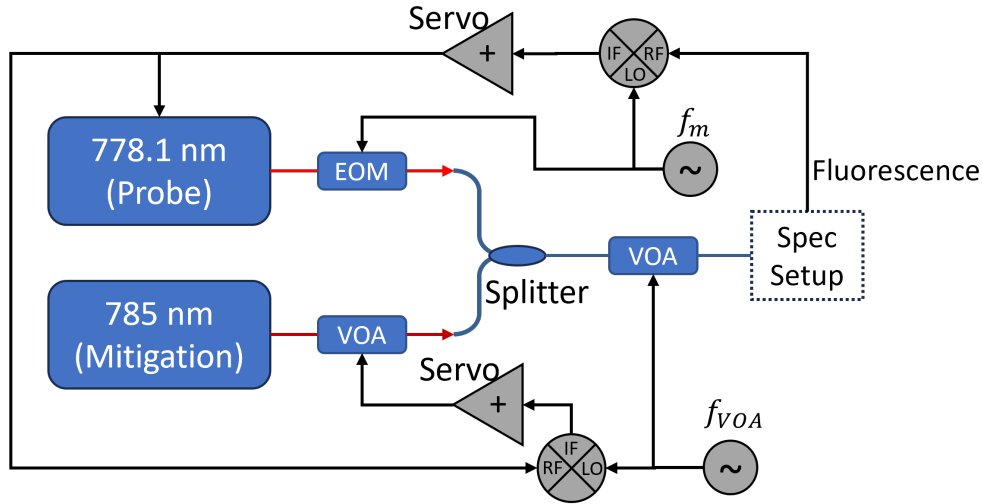


**Figure 4.16:** Setup for two color Stark mitigation with active balancing. EOM: electro-optic modulator, VOA: variable optical attenuator.

The beauty of this mitigation scheme is its autobalancing nature. It is always a direct measurement of the total ac-Stark shift from both lasers. This method is agnostic to the wavelength of the mitigation laser, the shape of the probe spectrum (i.e. residual Stark shift), or (if both lasers are pulsed) the overlap of probe and mitigation pulses. Additionally, since it sets the ac-Stark shift to zero, alignment based Stark shifts [85, §II-B] are also nullified.

We attempted a proof-of-principle implementation of this mitigation scheme with some promising first results. This experiment was performed with a cw probe and cw mitigation laser, probing a small vapor cell with 30 mW of 778 nm light. Due to the limited power for our mitigation laser, we tuned to 780.5 nm, where the required mitigation power is 12% of the probe power. Since the timescale for detrimental drifts in the locked ac-Stark shift is generally greater than  $10^3$  s, which requires multi-day recording, we applied a pseudo-drift by modulating the clock laser intensity with a period of 20 s. We recorded the clock instability with this driving field on or off and the mitigation laser on and locked or off (Fig. 4.17). We see at the antinodes of the applied modulation (10 s, 30 s, and 50 s) that the mitigation servo (purple) is suppressing the effect of the 50 mHz intensity modulation (orange).

Unfortunately, having the mitigation laser on increased the 1 s instability from  $1.6 \times 10^{-12}$  to  $1.1 \times 10^{-11}$ . The source of this increase in instability is currently unclear. Having

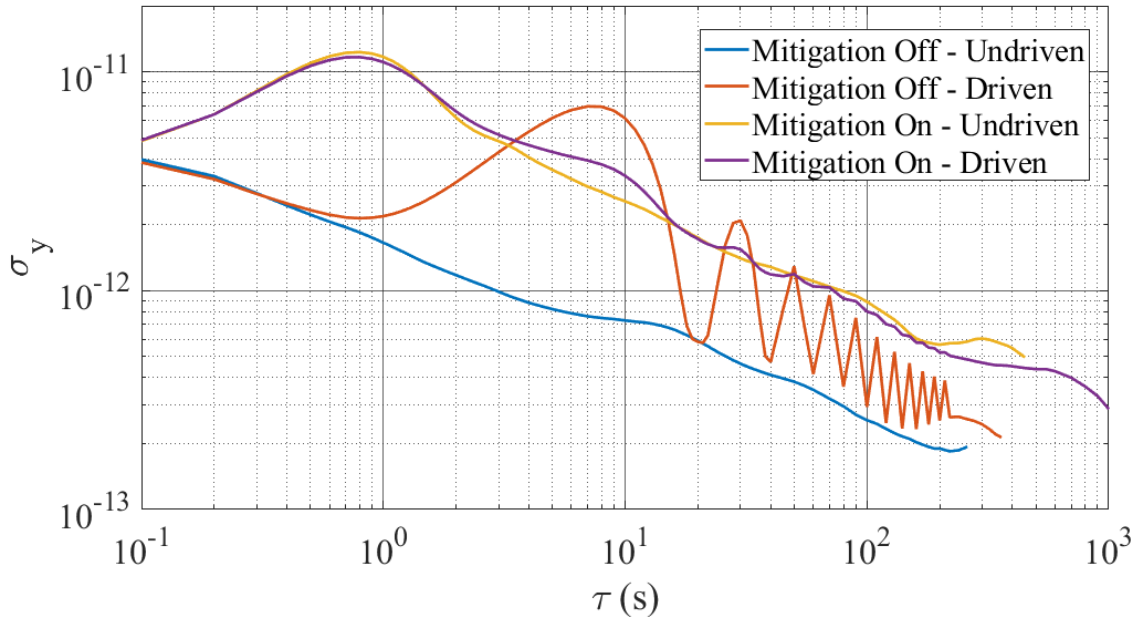


**Figure 4.17:** Allan deviation from attempted ac-Stark shift mitigation. The “Driven” samples had a sinusoidal modulation with a 20 s period applied to the intensity of the clock laser to simulate instability in intensity. “Mitigation Off” indicates that the mitigation laser was blocked, “Mitigation On” indicates that the mitigation laser was unblocked and the mitigation servo was locked.

the mitigation laser so close to the D2 transition in  $^{87}\text{Rb}$  ( $\approx 100$  GHz) may be inducing secondary effects not accounted for in this approach. Further experimental effort is required to determine whether this effect is fundamental to our mitigation scheme or whether it was an experimental artifact. If further efforts prove that the phase noise of the mitigation laser is a limitation, it is possible to derive the mitigation laser from the same frequency comb as our probe laser and benefit from the high stability thereof. If this is not a limitation, it may be lower SWaP and lower complexity to generate the mitigation light with a direct 785 nm DFB (distributed feedback) laser.

## 4.5 Overall Clock Performance

### 4.5.1 Transition linewidth

The connectorized nature of our spectroscopy setup allowed for simple comparative measurements between cw excitation and direct comb excitation without changing alignment

or other experimental parameters. One such important comparative measurement is the linewidth of our reference, which can limit the short-term frequency instability if the reference is shot-noise limited (see Eqn. 3.1). Previous efforts for hot vapor direct comb excitation have shown linewidth substantially broader than their cw equivalents, due to residual Doppler broadening [65, 104, 105]; however, direct comb excitation of laser cooled rubidium atoms has shown linewidth as low as 450 kHz [59].

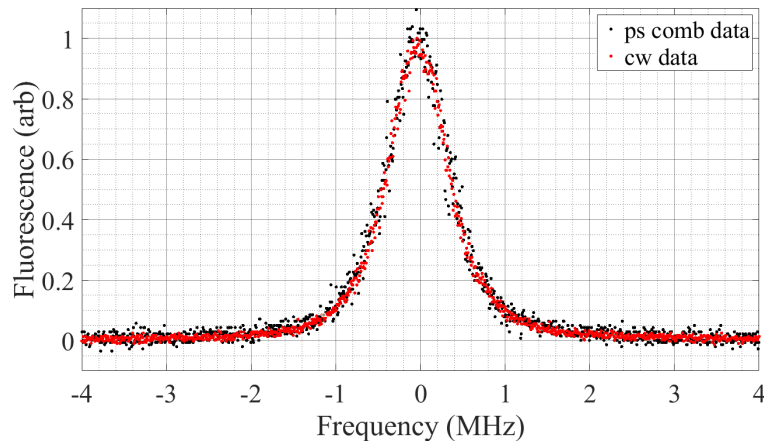


**Figure 4.18:** Comparative measurement of the linewidth for cw excitation (red) vs direct comb excitation (black). These data were normalized in intensity, since the direct comb excitation at 75 GHz bandwidth produces 25% fluorescence compared to cw. The frequency axis was calibrated via the spacing between the peaks of the  $F=2 \rightarrow 4$  and  $F=2 \rightarrow 3$  transitions.

Shown in Fig. 4.18 are the results of this comparative linewidth measurement for a 75 GHz FWHM optical spectrum at 778 nm. A Lorentzian fit to these lineshapes resulted in a FWHM linewidth of 762 kHz for cw excitation and 774 kHz for direct comb excitation. This linewidth includes contributions from the natural lifetime (330 kHz), transit-time (310 kHz for 230  $\mu\text{m}$  beam diameter at 100  $^\circ\text{C}$ ), helium collisional broadening (200 kHz given 4 mTorr He partial pressure). The contribution from rubidium collisional broadening (16 kHz) and Zeeman broadening are believed to be negligible.

#### 4.5.2 *ac-Stark shift sensitivity*

As shot-noise often limits two-photon clocks in the short-term, a common long-term source of instability is the ac-Stark shift [52, 53]. We measured the effect of the ac-Stark shift on

our clock frequency by varying the power on one clock while keeping the other clock power constant, then measuring the corresponding change in fractional frequency for the two clock relative measurement. This measurement was performed both with a cw probe and a direct comb probe, each on the same spectroscopy setup to ensure the same beam size and overlap. The results of this measurement are shown in Fig. 4.19.

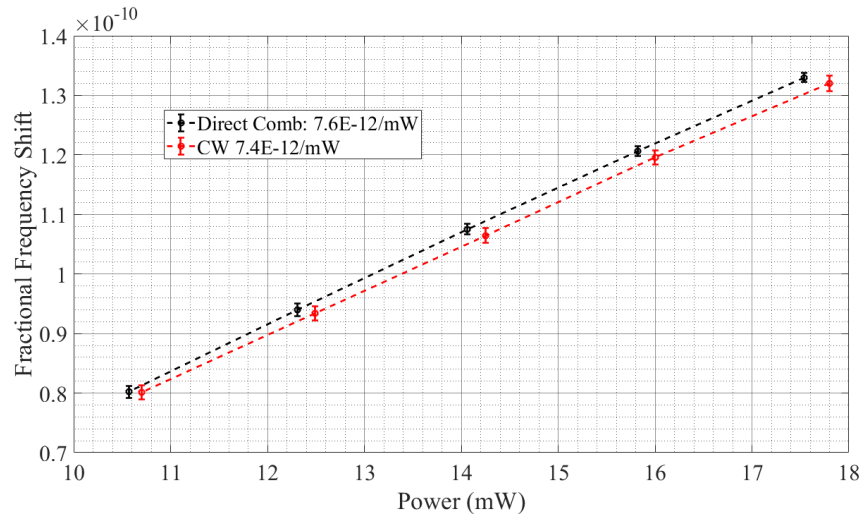


**Figure 4.19:** Comparative measurement of the ac-Stark shift for cw excitation (red) vs direct comb excitation (black). The data are shifted up to ensure their linear fit intersects the origin. Error bars indicate the standard deviation of the frequency shift at each power level.

The similarity between the measured  $7.4 \times 10^{-12}$  and  $7.6 \times 10^{-12}/\text{mW}$  Stark shift values show that it is indeed the average power of the comb pulses that determines the ac-Stark shift, not the peak power. This means that the challenges of stabilizing the ac-Stark shift in a direct comb frequency standard should not be fundamentally different from those of a cw frequency standard.

We also measured the “residual Stark shift” by changing the temperature of the FBG on one clock and tracking the change in fractional frequency (Fig. 4.20). We have measured the temperature coefficient of our FBG to be  $5.8 \text{ pm/K}$ . The residual Stark shift data shows a trend at  $4.4 \times 10^{-13}/\text{K}$ , implying a required temperature stability of below  $20 \text{ mK}$  to average below  $1 \times 10^{-14}$ . Scanning the FBG temperature from  $64$  to  $68$  degrees resulted in minimal change in fluorescence level, but over  $1 \times 10^{-12}$  change in clock frequency, meaning that stabilizing the detected fluorescence voltage would not adequately stabilize this residual

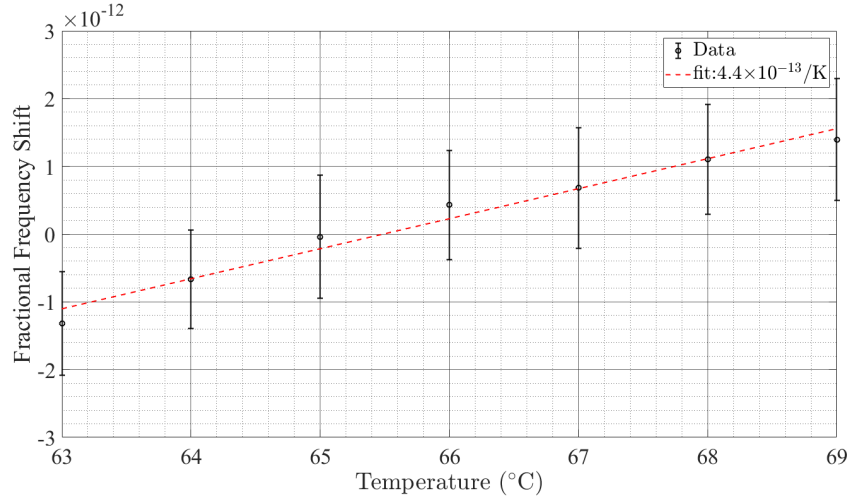


**Figure 4.20:** Measurement of the residual Stark shift via changing the center wavelength of the FBG by changing the FBG temperature.

stark shift. This effect is unique to direct comb spectroscopy, but this sensitivity need not limit clock performance, as packaged FBGs can be significantly less sensitive to thermal drift.

### 4.5.3 Instability

The Allan deviation shown in Fig. 4.21, taken between the two direct comb rubidium frequency references, is the most significant result from this research. This frequency instability rivals that shown from any previous rubidium two-photon frequency standards without the need of a cw probe laser. This instability was acquired while running both systems at an average power of 18 mW, stabilized via the intensity stabilization modules. Both clocks were set up as diagrammed in Fig. 4.7.

This measurement is a two-clock relative instability divided by  $\sqrt{2}$  to imply single clock instability. This is an accurate predictor of each clock's instability if the clocks are similarly unstable in an uncorrelated way. If instead one clock is significantly worse than the other clock at a given  $\tau$ , our estimated single-clock instability underestimates the instability in the bad clock and overestimates the instability in the better clock. This single-clock measurement represents the worst that our best clock could be.

To better understand which clock is limiting our instability, we performed a three-cornered-

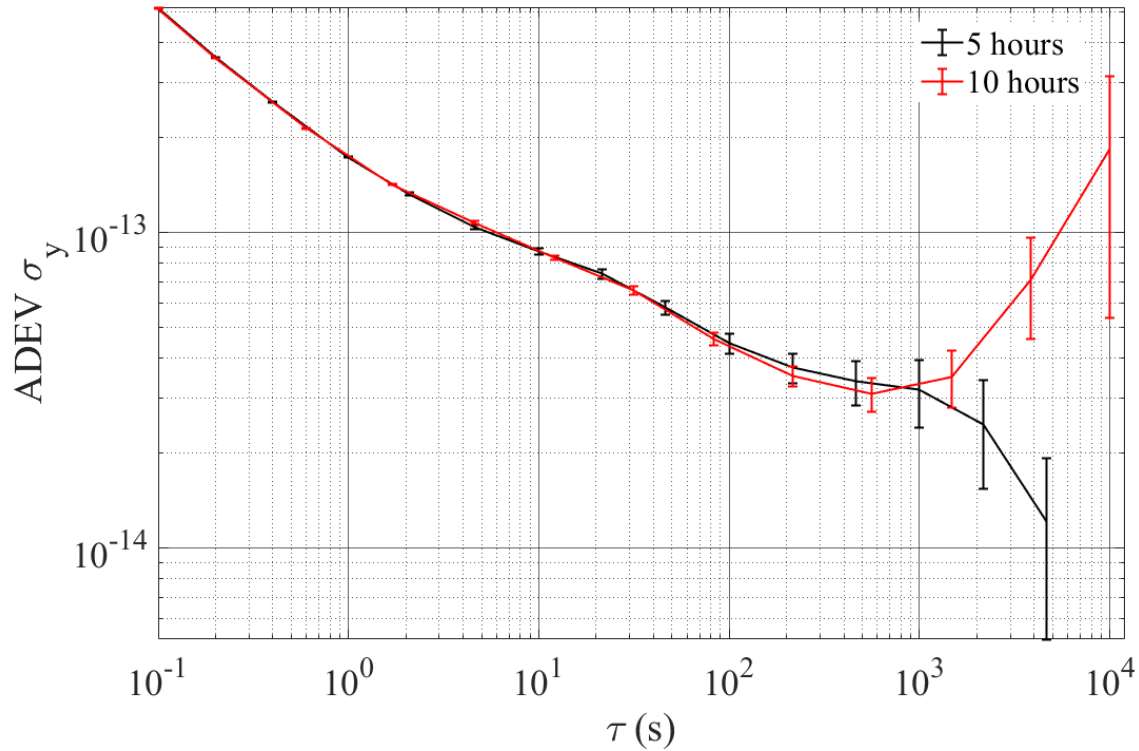


**Figure 4.21:** Allan deviation comparing two direct-comb rubidium frequency standards. In black is a 5 hour selection from the longer 10 hour run (red). The five hour selection was the portion of the frequency record with the least frequency drift. This measurement is the two-clock relative instability divided by  $\sqrt{2}$  to imply single clock instability.

hat measurement [7, §10.14] between the IMRA, Vescent, and RIO clocks. The results of this are shown in Fig. 4.22. This is a useful confirmation that, especially at short times, the frequency instability of both comb-based references are similar. Unfortunately, times longer than  $\approx 500$  s give us less information about the relative instability of each direct comb clock, as both are below the instability of the RIO. The three-cornered hat measurement of the IMRA diverges at  $10^3$  s, as the IMRA is significantly more stable than the RIO. This divergence is typical in three-cornered hat measurements and is why “it is not a substitute for a low noise reference.” [7]. To best disentangle each source of noise, it would be ideal to have a low noise reference such as a maser.



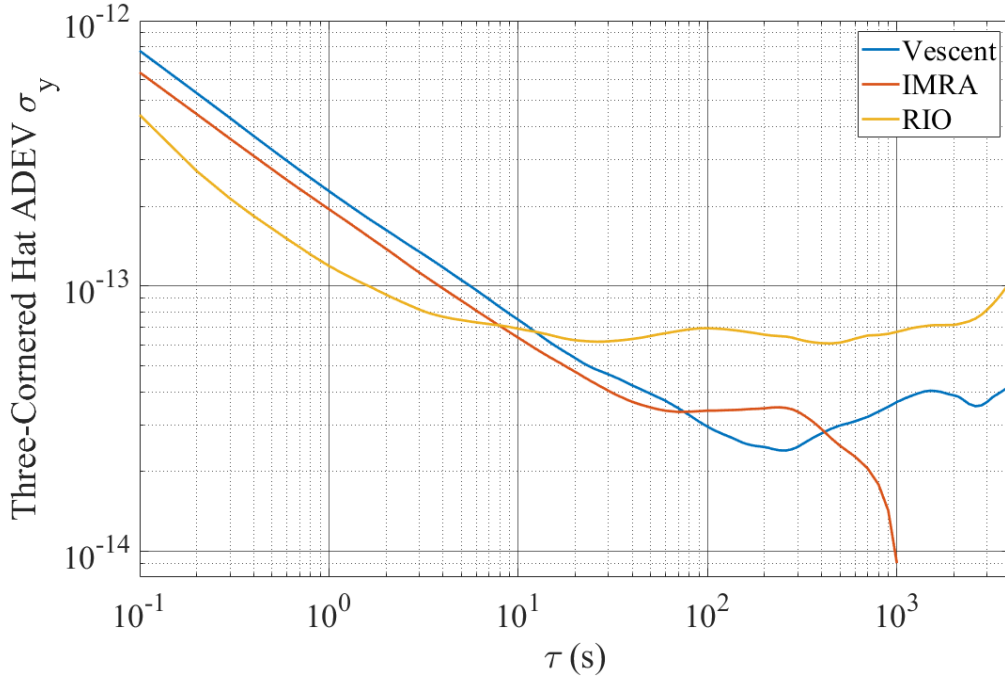


**Figure 4.22:** Three-cornered hat measurement of the three frequency references developed.

#### 4.5.4 Power Dependence of Short-Term Stability

The most likely sources of the short-term instability limit at  $1.7 \times 10^{-13} / \sqrt{\tau}$  are shot-noise or intermodulation noise. To determine whether we are shot-noise limited, we measured the 1 s Allan deviation at various probe intensities. Since we are always recording two-clock instabilities, whichever clock we did not change the intensity on was set to its highest intensity, so as to minimize the potential of that clock being shot-noise limited. Since shot-noise limited instability decreases as  $1/\sqrt{\Gamma}$  (where  $\Gamma$  is the rate of fluorescence photon detection), and  $\Gamma$  increases as  $I^2$  for probe intensity  $I$  (assuming the two-photon transition is not saturated), the short-term instability should decrease as  $1/I$  until shot-noise is not the limiting noise source.

The results of such a measurement are shown in Fig. 4.23, including the results of a fit to  $\sigma_y(I) = \sqrt{(\frac{a}{I})^2 + b^2}$  (shot-noise added in quadrature with a noise floor  $b$ ). For this particular measurement, the floor was at  $1.5 \times 10^{-13}$  and the shot-noise scaled as  $1.5 \times 10^{-12}$  divided by the power in mW. This floor is consistent across many measurements - the scaling of the shot-noise with power is dependent on alignment, collection efficiency, and

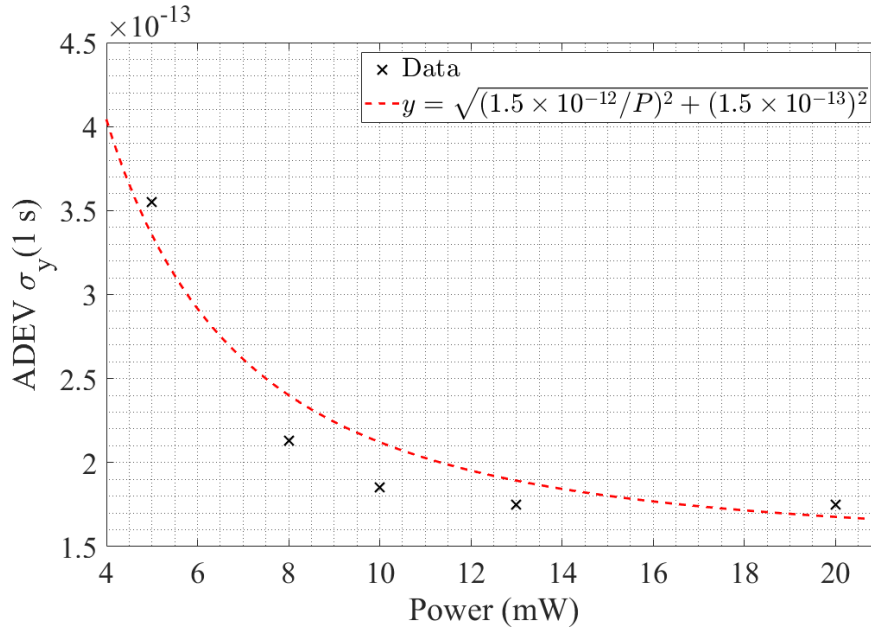


**Figure 4.23:** Measurement of the one second fractional frequency instability vs. power, to determine the cross-over where probe power no longer limits clock stability.

excitation efficiency. This measurement is done whenever major modifications are made to the spectroscopy setup to cross-over, where the short-term instability does not appreciably decrease with increasing power (for the setup pictured, this would be about 15 mW). Whereas the phase noise measurements in §4.3 imply an intermodulation limit in the low  $10^{-14}$  range, the origin of this limit at  $1.5 \times 10^{-13}$  is currently unclear. It may be a matter of optimizing the electronic detection scheme to get away from an electronic noise floor.

#### 4.5.5 Thermal Drift

The long-term frequency drift shown in Fig. 4.21 after 1000 s is undesirable but not unexpected. As the fluorescence length is small in direct comb spectroscopy, we have had to use high intensity probes to recover useable signal levels. This makes our experiment more comparable to the parameters of Newman *et. al* [53] which reports similar (albeit less severe) problems past 1000 s, as compared to larger vapor cells such as Lemke *et. al* [54] which do not report drifts on this timescale. The most likely source of this drift is from intensity instability via the ac-Stark shift. With our tightly focused probe, it would require intensity stability of our 18 mW probe to  $< 1.3 \mu\text{W}$  to surpass  $1 \times 10^{-14}$  stability (using the

slope from Fig. 4.19). While intensity stabilization at 1 part in  $10^4$  is achievable over short times, any drift in the temperature of the ISM may drift either the detector responsivity or voltage reference beyond that stability requirement. This effect can be seen in the correlation between our clock frequency, detected fluorescence level, and simultaneously recorded room temperature (Fig. 4.24).

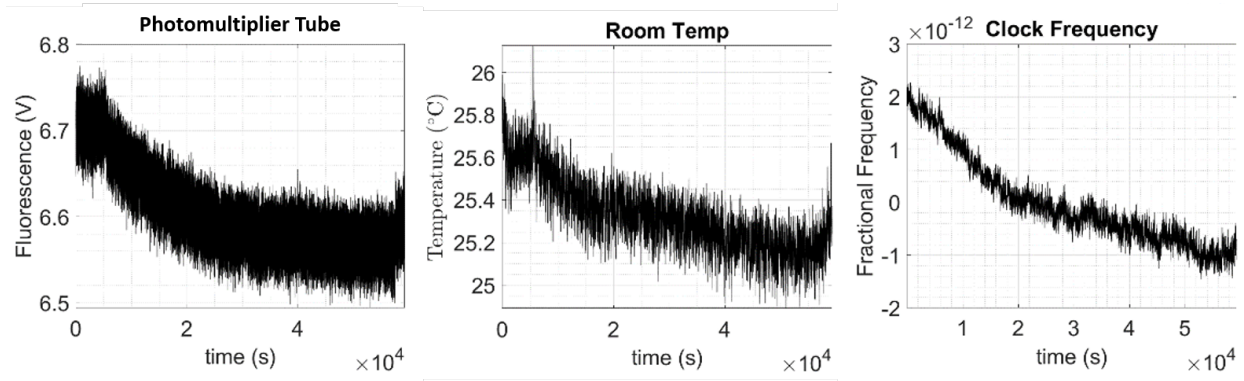


**Figure 4.24:** Measurement of fluorescence detected on a PMT, room temperature, and clock frequency during an overnight run. The correlation supports the hypothesis that the intensity of our probe is tracking the room temperature due to thermal drifts in the ISM.

While the most likely suspect for this drift is thermally dependent light-shifts, there are several other potential sources. While the vapor cell body, cold point, and FBG all measure in-loop temperature stabilities at the 1 mK level, if any of these are insufficient measures of their corresponding experimental parameter, that would explain this drift as well. All of these problems (excepting FBG temperature) are the same problems experienced by any two-photon clock and most other competitive portable frequency references. To overcome these problems will require either novel techniques (touched on in the next chapter) or skilled engineering.

## Chapter 5

### Conclusion

The direct comb spectroscopy optical frequency reference which we developed is now operating with short-term stability rivaling other rubidium two-photon clocks and it appears that long-term stability is currently limited only by engineering. The SWaP benefits from removal of a laser and increased second harmonic generation efficiency. The major drawbacks are the reduction in fluorescence due to finite Doppler-free volume and the long-term instability from the residual Stark shift. The former can be mitigated by proper selection of a narrow bandwidth FBG and is less comparatively disadvantageous as the vapor cell length decreases. The latter would be reduced by athermal packaging of the FBG, but would only be removed by active Stark shift mitigation.

It is a necessary first step to say that direct comb spectroscopy results in performance no worse than cw spectroscopy – it is significantly more interesting to consider how direct comb spectroscopy may offer performance which surpasses the cw competition. One immediate area for improvement over cw spectroscopy is in Doppler background removal. The Doppler-free fluorescence peaks in standard two-photon spectroscopy sit on top of a Doppler broadened background, seen in Fig. 5.1. This background is the effect of absorbing two photons from the same direction, rather than one from each propagation direction. Since this background is significantly broader than the linewidth of the clock transition ( $\approx 1$  GHz compared to 700 kHz) it is normally ignored as an offset; it does, however, contribute to the shot-noise and lower the system SNR.

This Doppler background can be removed in a few different ways. First, changing the transition to  $5S_{1/2} \rightarrow 7S_{1/2}$  would enable Doppler background elimination via probing in a  $\sigma_+ - \sigma_-$  scheme. Since the two-photon selection rules forbid  $\Delta m_F \neq 0$  in a  $S \rightarrow S$  transition

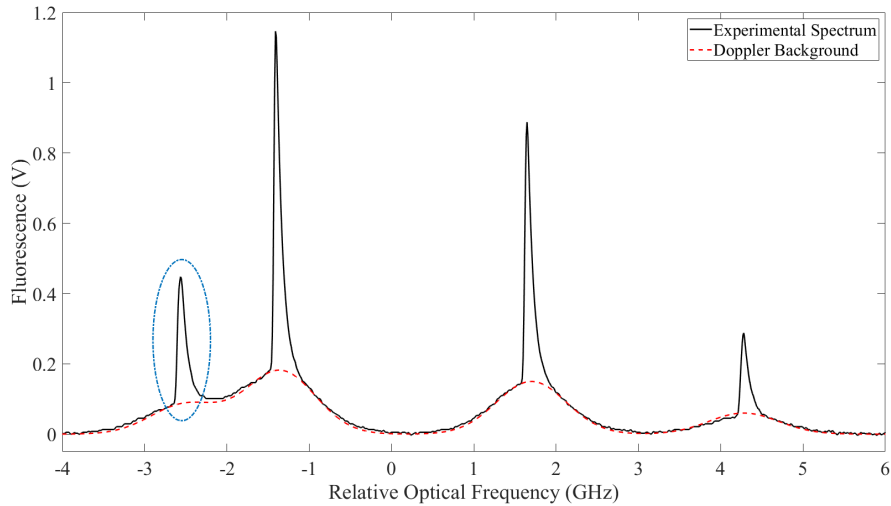


**Figure 5.1:** Scan across the two-photon  $5S_{1/2} \rightarrow 5D_{5/2}$  transitions in a vapor cell with natural abundance Rb. Narrow Doppler-free peaks can be seen in the experimental data (Black) on top of a Doppler-broadened background (Red). The clock transition in  $^{87}\text{Rb}$  is circled in blue. The scan is too fast to resolve the hyperfine excited state splitting.

[106, §5.2.2], only transitions which absorb both a  $\sigma_+$  and  $\sigma_-$  photon are excited, i.e. only the Doppler-free signal remains. Generally, the  $S \rightarrow D$  transitions are preferred to the  $S \rightarrow S$  transitions due to their narrower linewidths and smaller intermediate state detuning. The  $S \rightarrow S$  transitions do have smaller Zeeman sensitivity and proportionately smaller ac-Stark shift, so there may be worthwhile study there.

Alternatively, the Doppler background can be removed by probing the atoms with a different color from each direction, such that neither direction can independently excite the transition. Achieving this with cw excitation means adding another laser with its own amplification and SHG, then setting up a more complicated lock of the frequency comb to the sum-frequency of the two lasers [68]. Direct comb excitation can accomplish this Doppler cancellation via dichroic pulse pair generation from one frequency comb [104]. This can be done through a properly designed 778 nm FBG, which reflects two wavelength bands with the proper delay between them. In the split-pulse retroreflector (microcell) design, the delay sets the distance of the fluorescence from the reflective coating.

Doppler background removal highlights the key to why direct comb spectroscopy has future potential: many potential improvements to two-photon clocks require more than one laser

wavelength and a frequency comb can provide all of these wavelengths without the need for additional lasers. Two-color excitation has been used to remove the Doppler background [104], ac-Stark shift [68], and temperature shift [107]. Beyond these two-color schemes, there is further potential in multi-transition spectroscopy probed with the same frequency comb. By weakly probing these additional transitions, each of which has a different sensitivity to collisional shifts and to the ac-Stark shift from 778 nm light, and correlating the drifts on each, it should be possible to use their shifts as precise power meters and thermometers.

There are thus at least two directions to proceed with this two-photon direct comb frequency standard: 1) rigorous engineering work to mitigate the temperature drifts in the current design or 2) interesting exploratory work on novel concepts to root out the instabilities at their source. There are immediate advancements to be made by pursuit of the former, but both the potential long-term gains and the personal biases of the author favor the latter. Direct comb spectroscopy has shown to have at least as much potential as a compact frequency standard as cw two-photon spectroscopy, and the potentials for multi-wavelength instability mitigation provide a great direction for future work.

## GLOSSARY

### Common Scientific Symbols

$m$	atomic mass
$c$	speed of light
$k_B$	Boltzmann constant
$\hbar$	reduced Planck's constant
T	temperature (absolute)

### Experiment Specific Symbols

$f_{rep}$	comb repetition rate
$f_{ceo}$	comb carrier-envelope offset frequency
$\sigma_y$	fractional frequency Allan deviation
Q	quality factor
$S_y$	fractional frequency noise power spectral density

### Acronyms

CBT	cesium beam tube
cRb	cold rubidium clock
CSAC	chip-scale atomic clock
DCS	dual-comb spectroscopy
FWHM	full-width at half-max
NALM	nonlinear amplifying loop mirror
NOLM	nonlinear optical loop mirror

O-RAFS	optical rubidium atomic frequency standard
PLL	phase-locked loop
PMT	photo-multiplier tube
RAFS	rubidium atomic frequency standard
RAM	residual amplitude modulation
RF	radio frequency
RMS	root-mean-squared amplitude
SESAM	semiconductor saturable absorber mirror
VCO	voltage controlled oscillator
VIPA	virtually imaged phased array

This dissertation maintains the practice of representing radio-frequencies with  $f$  and optical frequencies with  $\omega$  or  $\nu$ . While the beauty of a frequency comb is its bridging of this gap, the distinct notation is helpful for legibility.

There is some disagreement about whether the frequency standard discussed within this dissertation is properly called a clock. The arguments against clock designation are thus: 1. this system is stable but not accurate (i.e. systematic offsets are not quantified) and 2. the phase counter does not include an offset for starting time so that it may be compared to SI time. My response is this: neither are cold-atom fountains clocks; they are timepieces, as clocks must audibly sound out the hours per their Latin root *clocca*, which means “bell”. The posture which responds to novelty with “technically, that word doesn’t apply here, it only applies to *my* technology” is a posture opposed to progress. But if it comforts the reader, mentally substitute “frequency standard” each time “clock” is written.



## References

- [1] W. Thomson and P. G. Tait, *Treatise on Natural Philosophy*. Cambridge University Press, 1879, vol. 1.1.
- [2] H. Ball, W. D. Oliver, and M. J. Biercuk, “The role of master clock stability in quantum information processing,” *npj Quantum Information*, vol. 2, 1 2016. DOI: [10.1038/npjqi.2016.33](https://doi.org/10.1038/npjqi.2016.33).
- [3] J. Xuereb, P. Erker, F. Meier, M. T. Mitchison, and M. Huber, “Impact of imperfect timekeeping on quantum control,” *Phys. Rev. Lett.*, vol. 131, p. 160 204, 16 Oct. 2023. DOI: [10.1103/PhysRevLett.131.160204](https://doi.org/10.1103/PhysRevLett.131.160204). [Online]. Available: <https://link.aps.org/doi/10.1103/PhysRevLett.131.160204>.
- [4] B. L. S. Marlow and D. R. Scherer, “A review of commercial and emerging atomic frequency standards,” *IEEE Transactions on Ultrasonics, Ferroelectrics, and Frequency Control*, vol. 68, no. 6, pp. 2007–2022, 2021. DOI: [10.1109/TUFFC.2021.3049713](https://doi.org/10.1109/TUFFC.2021.3049713).
- [5] S. M. Brewer *et al.*, “ $^{27}\text{Al}^+$  Quantum-logic clock with a systematic uncertainty below  $10^{-18}$ ,” *Phys. Rev. Lett.*, vol. 123, p. 033 201, 3 Jul. 2019. DOI: [10.1103/PhysRevLett.123.033201](https://doi.org/10.1103/PhysRevLett.123.033201). [Online]. Available: <https://link.aps.org/doi/10.1103/PhysRevLett.123.033201>.
- [6] E. Oelker *et al.*, “Demonstration of  $4.8 \times 10^{-17}$  stability at 1 s for two independent optical clocks,” *Nature Photonics*, vol. 13, pp. 714–719, 2019.
- [7] W. J. Riley, *Handbook of Frequency Stability Analysis*. 2008.
- [8] H. Schnatz, B. Lipphardt, J. Helmcke, F. Riehle, and G. Zinner, “First phase-coherent frequency measurement of visible radiation,” *Physical Review Letters*, vol. 76, no. 1, pp. 18–21, 1996.

- [9] M. J. Martin, S. M. Foreman, T. R. Schibli, and J. Ye, “Testing ultrafast mode-locking at microhertz relative optical linewidth,” *Opt. Express*, vol. 17, no. 2, pp. 558–568, Jan. 2009. DOI: [10.1364/OE.17.000558](https://doi.org/10.1364/OE.17.000558). [Online]. Available: <https://opg.optica.org/oe/abstract.cfm?URI=oe-17-2-558>.
- [10] J. Kim and Y. Song, “Ultralow-noise mode-locked fiber lasers and frequency combs: Principles, status, and applications,” *Adv. Opt. Photon.*, vol. 8, no. 3, pp. 465–540, Sep. 2016. DOI: [10.1364/AOP.8.000465](https://doi.org/10.1364/AOP.8.000465). [Online]. Available: <https://opg.optica.org/aop/abstract.cfm?URI=aop-8-3-465>.
- [11] R. N. Bracewell, *The Fourier transform and its applications*, 3rd ed. McGraw-Hill, 1986.
- [12] M. Kourogi, K. Nakagawa, and M. Ohtsu, “Wide-span optical frequency comb generator for accurate optical frequency difference measurement,” *IEEE Journal of Quantum Electronics*, vol. 29, no. 10, pp. 2693–2701, 1993. DOI: [10.1109/3.250392](https://doi.org/10.1109/3.250392).
- [13] M. Zhang *et al.*, “Broadband electro-optic frequency comb generation in a lithium niobate microring resonator,” *Nature*, vol. 568, 2019.
- [14] P. W. Milonni and J. H. Eberly, *Lasers*. John Wiley & Sons, Inc., 1988.
- [15] A. L. Gaeta, M. Lipson, and T. J. Kippenberg, “Photonic-chip-based frequency combs,” *Nature Photonics*, vol. 13, pp. 158–169, 2019.
- [16] B. R. Washburn, W. C. Swann, and N. R. Newbury, “Response dynamics of the frequency comb output from a femtosecond fiber laser,” *Opt. Express*, vol. 13, no. 26, pp. 10 622–10 633, Dec. 2005. DOI: [10.1364/OPEX.13.010622](https://doi.org/10.1364/OPEX.13.010622). [Online]. Available: <https://opg.optica.org/oe/abstract.cfm?URI=oe-13-26-10622>.
- [17] H. Telle, B. Lipphardt, and J. Stenger, “Kerr-lens, mode-locked lasers as transfer oscillators for optical frequency measurements,” *Appl Phys B*, vol. 74, pp. 1–6, 2002.
- [18] L. E. Hargrove, R. L. Fork, and M. A. Pollack, “LOCKING OF He-Ne LASER MODES INDUCED BY SYNCHRONOUS INTRACAVITY MODULATION,” *Applied Physics Letters*, vol. 5, no. 1, pp. 4–5, Jul. 1964, ISSN: 0003-6951. DOI: [10.1063/1.1759881](https://doi.org/10.1063/1.1759881).

- 1.1754025. eprint: [https://pubs.aip.org/aip/apl/article-pdf/5/1/4/18417146/4\\\_1\\\_online.pdf](https://pubs.aip.org/aip/apl/article-pdf/5/1/4/18417146/4\_1\_online.pdf). [Online]. Available: <https://doi.org/10.1063/1.1754025>.
- [19] A. J. DeMaria, D. A. Stetser, and H. Heynau, “SELF MODE-LOCKING OF LASERS WITH SATURABLE ABSORBERS,” *Applied Physics Letters*, vol. 8, no. 7, pp. 174–176, Apr. 1966, ISSN: 0003-6951. DOI: [10.1063/1.1754541](https://doi.org/10.1063/1.1754541). eprint: [https://pubs.aip.org/aip/apl/article-pdf/8/7/174/18418700/174\\\_1\\\_online.pdf](https://pubs.aip.org/aip/apl/article-pdf/8/7/174/18418700/174\_1\_online.pdf). [Online]. Available: <https://doi.org/10.1063/1.1754541>.
- [20] H. Telle, G. Steinmeyer, A. Dunlop, J. Stenger, D. Sutter, and U. Keller, “Carrier-envelope offset phase control: A novel concept for absolute optical frequency measurement and ultrashort pulse generation,” *Applied Physics B*, vol. 69, pp. 327–332, 1999.
- [21] J. Reichert, R. Holzwarth, T. Udem, and T. Hänsch, “Measuring the frequency of light with mode-locked lasers,” *Optics Communications*, vol. 172, no. 1, pp. 59–68, 1999, ISSN: 0030-4018. DOI: [https://doi.org/10.1016/S0030-4018\(99\)00491-5](https://doi.org/10.1016/S0030-4018(99)00491-5). [Online]. Available: <https://www.sciencedirect.com/science/article/pii/S0030401899004915>.
- [22] D. J. Jones *et al.*, “Carrier-envelope phase control of femtosecond mode-locked lasers and direct optical frequency synthesis,” *Science*, vol. 288, pp. 635–639, 2000.
- [23] A. Tourigny-Plante, V. Michaud-Belleau, N. Bourbeau Hébert, H. Bergeron, J. Genest, and J.-D. Deschênes, “An open and flexible digital phase-locked loop for optical metrology,” *Review of Scientific Instruments*, vol. 89, no. 9, p. 093 103, Sep. 2018, ISSN: 0034-6748. DOI: [10.1063/1.5039344](https://doi.org/10.1063/1.5039344). eprint: [https://pubs.aip.org/aip/rsi/article-pdf/doi/10.1063/1.5039344/15992294/093103\\\_1\\\_online.pdf](https://pubs.aip.org/aip/rsi/article-pdf/doi/10.1063/1.5039344/15992294/093103\_1\_online.pdf). [Online]. Available: <https://doi.org/10.1063/1.5039344>.
- [24] N. Picqué and T. W. Hänsch, “Frequency comb spectroscopy,” *Nature Photonics*, vol. 13, pp. 146–157, 3 2019. [Online]. Available: <https://doi.org/10.1038/s41566-018-0347-5>.
- [25] R. Rockmore, R. Gibson, J. V. Moloney, and R. J. Jones, “Vecsel-based virtually imaged phased array spectrometer for rapid gas phase detection in the mid-infrared,”

- Opt. Lett.*, vol. 45, no. 20, pp. 5796–5799, Oct. 2020. DOI: [10.1364/OL.405192](https://doi.org/10.1364/OL.405192). [Online]. Available: <https://opg.optica.org/ol/abstract.cfm?URI=ol-45-20-5796>.
- [26] S. Schiller, “Spectrometry with frequency combs,” *Opt. Lett.*, vol. 27, no. 9, pp. 766–768, May 2002. DOI: [10.1364/OL.27.000766](https://doi.org/10.1364/OL.27.000766). [Online]. Available: <https://opg.optica.org/ol/abstract.cfm?URI=ol-27-9-766>.
- [27] F. Keilmann, C. Gohle, and R. Holzwarth, “Time-domain mid-infrared frequency-comb spectrometer,” *Opt. Lett.*, vol. 29, no. 13, pp. 1542–1544, Jul. 2004. DOI: [10.1364/OL.29.001542](https://doi.org/10.1364/OL.29.001542). [Online]. Available: <https://opg.optica.org/ol/abstract.cfm?URI=ol-29-13-1542>.
- [28] I. Coddington, N. Newbury, and W. Swann, “Dual-comb spectroscopy,” *Optica*, vol. 3, no. 4, pp. 414–426, Apr. 2016. DOI: [10.1364/OPTICA.3.000414](https://doi.org/10.1364/OPTICA.3.000414). [Online]. Available: <https://opg.optica.org/optica/abstract.cfm?URI=optica-3-4-414>.
- [29] R. R. D. Weeks, “Dual-comb spectroscopy of laser-produced plasmas,” Ph.D. dissertation, University of Arizona, 2023.
- [30] L. C. Sinclair *et al.*, “Invited Article: A compact optically coherent fiber frequency comb,” *Review of Scientific Instruments*, vol. 86, no. 8, p. 081301, Aug. 2015, ISSN: 0034-6748. DOI: [10.1063/1.4928163](https://doi.org/10.1063/1.4928163). eprint: [https://pubs.aip.org/aip/rsi/article-pdf/doi/10.1063/1.4928163/14051684/081301\\_1\\_online.pdf](https://pubs.aip.org/aip/rsi/article-pdf/doi/10.1063/1.4928163/14051684/081301_1_online.pdf). [Online]. Available: <https://doi.org/10.1063/1.4928163>.
- [31] E. Baumann, F. R. Giorgetta, J. W. Nicholson, W. C. Swann, I. Coddington, and N. R. Newbury, “High-performance, vibration-immune, fiber-laser frequency comb,” *Opt. Lett.*, vol. 34, no. 5, pp. 638–640, Mar. 2009. DOI: [10.1364/OL.34.000638](https://doi.org/10.1364/OL.34.000638). [Online]. Available: <https://opg.optica.org/ol/abstract.cfm?URI=ol-34-5-638>.
- [32] J. Deschenes, <https://github.com/jddes/Frequency-comb-DPLL>.
- [33] N. R. Newbury, I. Coddington, and W. Swann, “Sensitivity of coherent dual-comb spectroscopy,” *Opt. Express*, vol. 18, no. 8, pp. 7929–7945, Apr. 2010. DOI: [10.1364/OE.18.007929](https://doi.org/10.1364/OE.18.007929). [Online]. Available: <https://opg.optica.org/oe/abstract.cfm?URI=oe-18-8-7929>.

- [34] A. Asahara and K. Minoshima, “Development of ultrafast time-resolved dual-comb spectroscopy,” *APL Photonics*, vol. 2, no. 4, p. 041301, Feb. 2017, ISSN: 2378-0967. DOI: [10.1063/1.4976730](https://doi.org/10.1063/1.4976730). eprint: [https://pubs.aip.org/aip/app/article-pdf/doi/10.1063/1.4976730/14111146/041301%5C%5C\\_online.pdf](https://pubs.aip.org/aip/app/article-pdf/doi/10.1063/1.4976730/14111146/041301%5C%5C_online.pdf). [Online]. Available: <https://doi.org/10.1063/1.4976730>.
- [35] J. Bergevin *et al.*, “dual-comb spectroscopy of laser-induced plasmas’,” *Nature Communications*, vol. 9, p. 1273, 1 2018. DOI: [10.1038/s41467-018-03703-0](https://doi.org/10.1038/s41467-018-03703-0).
- [36] R. R. Weeks, M. C. Phillips, Y. Zhang, S. S. Harilal, and R. J. Jones, “Measurement of neutral gadolinium oscillator strengths using dual-comb absorption spectroscopy in laser-produced plasmas,” *Spectrochimica Acta Part B: Atomic Spectroscopy*, vol. 181, p. 106199, 2021, ISSN: 0584-8547. DOI: <https://doi.org/10.1016/j.sab.2021.106199>. [Online]. Available: <https://www.sciencedirect.com/science/article/pii/S0584854721001567>.
- [37] Y. Zhang *et al.*, “Time-resolved dual-comb measurement of number density and temperature in a laser-induced plasma,” *Opt. Lett.*, vol. 44, no. 14, pp. 3458–3461, Jul. 2019. DOI: [10.1364/OL.44.003458](https://doi.org/10.1364/OL.44.003458). [Online]. Available: <https://opg.optica.org/ol/abstract.cfm?URI=ol-44-14-3458>.
- [38] R. R. D. Weeks, Y. Zhang, S. S. Harilal, M. C. Phillips, and R. J. Jones, “Multi-species temperature and number density analysis of a laser-produced plasma using dual-comb spectroscopy,” *Journal of Applied Physics*, vol. 131, no. 22, p. 223103, Jun. 2022, ISSN: 0021-8979. DOI: [10.1063/5.0094213](https://doi.org/10.1063/5.0094213). eprint: [https://pubs.aip.org/aip/jap/article-pdf/doi/10.1063/5.0094213/16506507/223103%5C%5C\\_online.pdf](https://pubs.aip.org/aip/jap/article-pdf/doi/10.1063/5.0094213/16506507/223103%5C%5C_online.pdf). [Online]. Available: <https://doi.org/10.1063/5.0094213>.
- [39] R. T. Rhoades *et al.*, “Dual-comb absorption spectroscopy of molecular ceo in a laser-produced plasma,” *Opt. Lett.*, vol. 47, no. 10, pp. 2502–2505, May 2022. DOI: [10.1364/OL.455237](https://doi.org/10.1364/OL.455237). [Online]. Available: <https://opg.optica.org/ol/abstract.cfm?URI=ol-47-10-2502>.
- [40] A. Nishiyama *et al.*, “Doppler-free dual-comb spectroscopy of rb using optical-optical double resonance technique,” *Opt. Express*, vol. 24, no. 22, pp. 25894–25904, Oct.

2016. DOI: [10.1364/OE.24.025894](https://doi.org/10.1364/OE.24.025894). [Online]. Available: <https://opg.optica.org/oe/abstract.cfm?URI=oe-24-22-25894>.
- [41] N. Kuse, A. Ozawa, I. Ito, and Y. Kobayashi, “Dual-comb saturated absorption spectroscopy,” in *CLEO: 2013*, Optica Publishing Group, 2013, CTu2I.1. DOI: [10.1364/CLEO\\_SI.2013.CTu2I.1](https://doi.org/10.1364/CLEO_SI.2013.CTu2I.1). [Online]. Available: [https://opg.optica.org/abstract.cfm?URI=CLEO\\_SI-2013-CTu2I.1](https://opg.optica.org/abstract.cfm?URI=CLEO_SI-2013-CTu2I.1).
- [42] L. Vasilenko, V. Chebotaev, and A. Shishaev, “Line shape of two-photon absorption in a standing-wave field in a gas,” *JETP Letters*, vol. 12, no. 3, pp. 113–116, 1970. [Online]. Available: [http://jetpletters.ru/ps/1728/article\\_26264.shtml](http://jetpletters.ru/ps/1728/article_26264.shtml).
- [43] F. Biraben, B. Cagnac, and G. Grynberg, “Experimental evidence of two-photon transition without doppler broadening,” *Phys. Rev. Lett.*, vol. 32, pp. 643–645, 12 Mar. 1974. DOI: [10.1103/PhysRevLett.32.643](https://doi.org/10.1103/PhysRevLett.32.643). [Online]. Available: <https://link.aps.org/doi/10.1103/PhysRevLett.32.643>.
- [44] M. D. Levenson and N. Bloembergen, “Observation of two-photon absorption without doppler broadening on the  $3S - 5S$  transition in sodium vapor,” *Phys. Rev. Lett.*, vol. 32, pp. 645–648, 12 Mar. 1974. DOI: [10.1103/PhysRevLett.32.645](https://doi.org/10.1103/PhysRevLett.32.645). [Online]. Available: <https://link.aps.org/doi/10.1103/PhysRevLett.32.645>.
- [45] T. W. Hänsch, S. A. Lee, R. Wallenstein, and C. Wieman, “Doppler-free two-photon spectroscopy of hydrogen  $1S - 2S$ ,” *Phys. Rev. Lett.*, vol. 34, pp. 307–309, 6 Feb. 1975. DOI: [10.1103/PhysRevLett.34.307](https://doi.org/10.1103/PhysRevLett.34.307). [Online]. Available: <https://link.aps.org/doi/10.1103/PhysRevLett.34.307>.
- [46] B. de Beauvoir *et al.*, “Metrology of the hydrogen and deuterium atoms: Determination of the rydberg constant and lamb shifts,” *Eur. Phys. J. D*, vol. 12, pp. 61–93, 2000.
- [47] S. A. Lee, J. Helmcke, J. L. Hall, and B. P. Stoicheff, “Doppler-free two-photon transitions to rydberg levels: Convenient, useful, and precise reference wavelengths for dye lasers,” *Opt. Lett.*, vol. 3, no. 4, pp. 141–143, Oct. 1978. DOI: [10.1364/OL.3.000141](https://doi.org/10.1364/OL.3.000141). [Online]. Available: <https://opg.optica.org/ol/abstract.cfm?URI=ol-3-4-141>.

- [48] S. Chu and A. P. Mills, “Excitation of the positronium  $1^3S_1 \rightarrow 2^3S_1$  two-photon transition,” *Phys. Rev. Lett.*, vol. 48, pp. 1333–1337, 19 May 1982. DOI: [10.1103/PhysRevLett.48.1333](https://doi.org/10.1103/PhysRevLett.48.1333). [Online]. Available: <https://link.aps.org/doi/10.1103/PhysRevLett.48.1333>.
- [49] S. Chu, A. P. Mills, A. G. Yodh, K. Nagamine, Y. Miyake, and T. Kuga, “Laser excitation of the muonium  $1S - 2S$  transition,” *Phys. Rev. Lett.*, vol. 60, pp. 101–104, 2 Jan. 1988. DOI: [10.1103/PhysRevLett.60.101](https://doi.org/10.1103/PhysRevLett.60.101). [Online]. Available: <https://link.aps.org/doi/10.1103/PhysRevLett.60.101>.
- [50] F. Nez, F. Biraben, R. Felder, and Y. Millerioux, “Optical frequency determination of the hyperfine components of the  $5s_{1/2}$ - $5d_{3/2}$  two-photon transitions in rubidium,” *Optics Communications*, vol. 102, no. 5, pp. 432–438, 1993, ISSN: 0030-4018. DOI: [https://doi.org/10.1016/0030-4018\(93\)90417-4](https://doi.org/10.1016/0030-4018(93)90417-4). [Online]. Available: <https://www.sciencedirect.com/science/article/pii/0030401893904174>.
- [51] Hilico, L., Felder, R., Touahri, D., Acef, O., Clairon, A., and Biraben, F., “Metrological features of the rubidium two-photon standards of the bnm-lptf and kastler brossel laboratories,” *Eur. Phys. J. AP*, vol. 4, no. 2, pp. 219–225, 1998. DOI: [10.1051/epjap:1998263](https://doi.org/10.1051/epjap:1998263). [Online]. Available: <https://doi.org/10.1051/epjap:1998263>.
- [52] K. W. Martin *et al.*, “Compact optical atomic clock based on a two-photon transition in rubidium,” *Phys. Rev. Appl.*, vol. 9, p. 014019, 1 Jan. 2018. DOI: [10.1103/PhysRevApplied.9.014019](https://doi.org/10.1103/PhysRevApplied.9.014019). [Online]. Available: <https://link.aps.org/doi/10.1103/PhysRevApplied.9.014019>.
- [53] Z. L. Newman *et al.*, “High-performance, compact optical standard,” *Opt. Lett.*, vol. 46, no. 18, pp. 4702–4705, Sep. 2021. DOI: [10.1364/OL.435603](https://doi.org/10.1364/OL.435603). [Online]. Available: <https://opg.optica.org/ol/abstract.cfm?URI=ol-46-18-4702>.
- [54] N. D. Lemke, K. W. Martin, R. Beard, B. K. Stuhl, A. J. Metcalf, and J. D. Elgin, “Measurement of optical rubidium clock frequency spanning 65 days,” *Sensors*, vol. 22, no. 5, 2022, ISSN: 1424-8220. DOI: [10.3390/s22051982](https://doi.org/10.3390/s22051982). [Online]. Available: <https://www.mdpi.com/1424-8220/22/5/1982>.

- [55] G. C. Bjorklund, M. D. Levenson, W. Lenth, and C. Ortiz, “‘frequency modulation (fm) spectroscopy’,” *Applied Physics B*, vol. 32, pp. 145–152, 3 1983. DOI: [10.1007/BF00688820](https://doi.org/10.1007/BF00688820). [Online]. Available: <https://doi.org/10.1007/BF00688820>.
- [56] M. Snadden, R. Clarke, and E. Riis, “Fm spectroscopy in fluorescence in laser-cooled rubidium,” *Optics Communications*, vol. 152, no. 4, pp. 283–288, 1998, ISSN: 0030-4018. DOI: [https://doi.org/10.1016/S0030-4018\(97\)00709-8](https://doi.org/10.1016/S0030-4018(97)00709-8). [Online]. Available: <https://www.sciencedirect.com/science/article/pii/S0030401897007098>.
- [57] Y. V. Baklanov and V. P. Chebotayev, “Narrow resonances of two-photon absorption of super-narrow pulses in gas,” *Applied Physics*, vol. 12, pp. 97–99, 1976.
- [58] R. Teets, J. Eckstein, and T. Hänsch, “Coherent two-photon excitation by multiple light pulses,” *Physical Review Letters*, vol. 38, no. 14, pp. 760–764, 1976.
- [59] M. Snadden, A. Bell, E. Riis, and A. Ferguson, “Two-photon spectroscopy of laser-cooled rb using a mode-locked laser,” *Optics Communications*, vol. 125, no. 1, pp. 70–76, 1996, ISSN: 0030-4018. DOI: [https://doi.org/10.1016/0030-4018\(95\)00711-3](https://doi.org/10.1016/0030-4018(95)00711-3). [Online]. Available: <https://www.sciencedirect.com/science/article/pii/0030401895007113>.
- [60] D. Meshulach and Y. Silberberg, “Coherent quantum control of two-photon transitions by a femtosecond laser pulse,” *Nature*, vol. 396, pp. 239–242, 6708 Nov. 1998. DOI: [10.1038/24329](https://doi.org/10.1038/24329).
- [61] T. H. Yoon, A. Marian, J. L. Hall, and J. Ye, “Phase-coherent multilevel two-photon transitions in cold rb atoms: Ultrahigh-resolution spectroscopy via frequency-stabilized femtosecond laser,” *Phys. Rev. A*, vol. 63, p. 011 402, 1 Dec. 2000. DOI: [10.1103/PhysRevA.63.011402](https://doi.org/10.1103/PhysRevA.63.011402). [Online]. Available: <https://link.aps.org/doi/10.1103/PhysRevA.63.011402>.
- [62] B. Chatel, J. Degert, S. Stock, and B. Girard, “Competition between sequential and direct paths in a two-photon transition,” *Phys. Rev. A*, vol. 68, p. 041 402, 4 Oct. 2003. DOI: [10.1103/PhysRevA.68.041402](https://doi.org/10.1103/PhysRevA.68.041402). [Online]. Available: <https://link.aps.org/doi/10.1103/PhysRevA.68.041402>.



- [63] M. C. Stowe, A. Pe'er, and J. Ye, "Control of four-level quantum coherence via discrete spectral shaping of an optical frequency comb," *Phys. Rev. Lett.*, vol. 100, p. 203 001, 20 May 2008. DOI: [10.1103/PhysRevLett.100.203001](https://doi.org/10.1103/PhysRevLett.100.203001). [Online]. Available: <https://link.aps.org/doi/10.1103/PhysRevLett.100.203001>.
- [64] A. Grinin *et al.*, "Two-photon frequency comb spectroscopy of atomic hydrogen," *Science*, vol. 370, no. 6520, pp. 1061–1066, 2020. DOI: [10.1126/science.abc7776](https://doi.org/10.1126/science.abc7776). eprint: <https://www.science.org/doi/pdf/10.1126/science.abc7776>. [Online]. Available: <https://www.science.org/doi/abs/10.1126/science.abc7776>.
- [65] S. Zhang *et al.*, "Direct frequency comb optical frequency standard based on two-photon transitions of thermal atoms," *Scientific Reports*, vol. 5, p. 15 114, Oct. 2015. DOI: <https://doi.org/10.1038/srep15114>. [Online]. Available: <https://www.nature.com/articles/srep15114>.
- [66] A. Ozawa and Y. Kobayashi, "Chirped-pulse direct frequency-comb spectroscopy of two-photon transitions," *Phys. Rev. A*, vol. 86, p. 022 514, 2 Aug. 2012. DOI: [10.1103/PhysRevA.86.022514](https://doi.org/10.1103/PhysRevA.86.022514). [Online]. Available: <https://link.aps.org/doi/10.1103/PhysRevA.86.022514>.
- [67] S. Erickson, <https://github.com/setherickson72/TwoPhotonModeling>.
- [68] V. Gerginov and K. Beloy, "Two-photon optical frequency reference with active ac stark shift cancellation," *Phys. Rev. Appl.*, vol. 10, p. 014 031, 1 Jul. 2018. DOI: [10.1103/PhysRevApplied.10.014031](https://doi.org/10.1103/PhysRevApplied.10.014031). [Online]. Available: <https://link.aps.org/doi/10.1103/PhysRevApplied.10.014031>.
- [69] Z. L. Newman *et al.*, "Architecture for the photonic integration of an optical atomic clock," *Optica*, vol. 6, no. 5, pp. 680–685, May 2019. DOI: [10.1364/OPTICA.6.000680](https://doi.org/10.1364/OPTICA.6.000680). [Online]. Available: <https://opg.optica.org/optica/abstract.cfm?URI=optica-6-5-680>.
- [70] C. Zhang *et al.*, "Tunable vuv frequency comb for 229mth nuclear spectroscopy," *Opt. Lett.*, vol. 47, no. 21, pp. 5591–5594, Nov. 2022. DOI: [10.1364/OL.473006](https://doi.org/10.1364/OL.473006). [Online]. Available: <https://opg.optica.org/ol/abstract.cfm?URI=ol-47-21-5591>.

- [71] *Quantum and Atom Optics*. 2007.
- [72] E. Rubiola, *Phase Noise and Frequency Stability in Oscillators*. Cambridge University Press, 2009.
- [73] C. Audoin, V. Candelier, and N. Diamarcq, “A limit to the frequency stability of passive frequency standards due to an intermodulation effect,” *IEEE Transactions on Instrumentation and Measurement*, vol. 40, no. 2, pp. 121–125, 1991. DOI: [10.1109/TIM.1990.1032896](https://doi.org/10.1109/TIM.1990.1032896).
- [74] E. A. Whittaker, C. M. Shum, H. Grebel, and H. Lotem, “Reduction of residual amplitude modulation in frequency-modulation spectroscopy by using harmonic frequency modulation,” *J. Opt. Soc. Am. B*, vol. 5, no. 6, pp. 1253–1256, Jun. 1988. DOI: [10.1364/JOSAB.5.001253](https://doi.org/10.1364/JOSAB.5.001253). [Online]. Available: <https://opg.optica.org/josab/abstract.cfm?URI=josab-5-6-1253>.
- [75] F. du Burck and O. Lopez, “Correction of the distortion in frequency modulation spectroscopy,” *Measurement Science and Technology*, vol. 15, no. 7, p. 1327, Jun. 2004. DOI: [10.1088/0957-0233/15/7/015](https://doi.org/10.1088/0957-0233/15/7/015). [Online]. Available: <https://dx.doi.org/10.1088/0957-0233/15/7/015>.
- [76] N. C. Wong and J. L. Hall, “Servo control of amplitude modulation in frequency-modulation spectroscopy: Demonstration of shot-noise-limited detection,” *J. Opt. Soc. Am. B*, vol. 2, no. 9, pp. 1527–1533, Sep. 1985. DOI: [10.1364/JOSAB.2.001527](https://doi.org/10.1364/JOSAB.2.001527). [Online]. Available: <https://opg.optica.org/josab/abstract.cfm?URI=josab-2-9-1527>.
- [77] L. Li, F. Liu, C. Wang, and L. Chen, “Measurement and control of residual amplitude modulation in optical phase modulation,” *Review of Scientific Instruments*, vol. 83, no. 4, p. 043111, Apr. 2012, ISSN: 0034-6748. DOI: [10.1063/1.4704084](https://doi.org/10.1063/1.4704084). eprint: [https://pubs.aip.org/aip/rsi/article-pdf/doi/10.1063/1.4704084/15667057/043111\\\_1\\\_online.pdf](https://pubs.aip.org/aip/rsi/article-pdf/doi/10.1063/1.4704084/15667057/043111\_1\_online.pdf). [Online]. Available: <https://doi.org/10.1063/1.4704084>.
- [78] W. Zhang *et al.*, “Reduction of residual amplitude modulation to  $1 \times 10^{-6}$  for frequency modulation and laser stabilization,” *Opt. Lett.*, vol. 39, no. 7, pp. 1980–1983, Apr. 2014. DOI: [10.1364/OL.39.001980](https://doi.org/10.1364/OL.39.001980). [Online]. Available: <https://opg.optica.org/ol/abstract.cfm?URI=ol-39-7-1980>.

- [79] N. D. Zamoski, G. D. Hager, C. J. Erickson, and J. H. Burke, “Pressure broadening and frequency shift of the  $5s1/2 \rightarrow 5d5/2$  and  $5s1/2 \rightarrow 7s1/2$  two photon transitions in  $85\text{rb}$  by the noble gases and  $n_2$ ,” *Journal of Physics B: Atomic, Molecular and Optical Physics*, vol. 47, no. 22, p. 225 205, Oct. 2014. DOI: [10.1088/0953-4075/47/22/225205](https://doi.org/10.1088/0953-4075/47/22/225205). [Online]. Available: <https://dx.doi.org/10.1088/0953-4075/47/22/225205>.
- [80] J. F. Kielkopf, “On the precise evaluation of the complete semiclassical spectral line shape for pressure-broadened atomic spectral lines,” *Journal of Physics B: Atomic and Molecular Physics*, vol. 9, no. 9, p. 1601, Jun. 1976. DOI: [10.1088/0022-3700/9/9/023](https://doi.org/10.1088/0022-3700/9/9/023). [Online]. Available: <https://dx.doi.org/10.1088/0022-3700/9/9/023>.
- [81] M. E. Henry and R. M. Herman, “Collisional broadening of rydberg atom transitions by rare gas perturbers,” *Journal of Physics B: Atomic, Molecular and Optical Physics*, vol. 35, no. 2, p. 373, Jan. 2002. DOI: [10.1088/0953-4075/35/2/313](https://doi.org/10.1088/0953-4075/35/2/313). [Online]. Available: <https://dx.doi.org/10.1088/0953-4075/35/2/313>.
- [82] M. E. Henry, “Collisional broadening of rydberg atoms by ground state neutral perturbers,” Ph.D. dissertation, Pennsylvania State University, 1998.
- [83] A. T. Dellis, V. Shah, E. A. Donley, S. Knappe, and J. Kitching, “Low helium permeation cells for atomic microsystems technology,” *Opt. Lett.*, vol. 41, no. 12, pp. 2775–2778, Jun. 2016. DOI: [10.1364/OL.41.002775](https://doi.org/10.1364/OL.41.002775). [Online]. Available: <https://opg.optica.org/ol/abstract.cfm?URI=ol-41-12-2775>.
- [84] D. A. Steck, available online at <http://steck.us/alkalidata> (revision 2.3.2, 10 September 2023).
- [85] K. W. Martin *et al.*, “Frequency shifts due to stark effects on a rubidium two-photon transition,” *Phys. Rev. A*, vol. 100, p. 023 417, 2 Aug. 2019. DOI: [10.1103/PhysRevA.100.023417](https://doi.org/10.1103/PhysRevA.100.023417). [Online]. Available: <https://link.aps.org/doi/10.1103/PhysRevA.100.023417>.
- [86] H. J. Metcalf and P. van der Straten, *Laser Cooling and Trapping*. Springer, 1999.

- [87] J. Mitroy, M. S. Safronova, and C. W. Clark, “Theory and applications of atomic and ionic polarizabilities,” *Journal of Physics B: Atomic, Molecular and Optical Physics*, vol. 43, no. 20, p. 202 001, Oct. 2010. DOI: [10.1088/0953-4075/43/20/202001](https://doi.org/10.1088/0953-4075/43/20/202001). [Online]. Available: <https://dx.doi.org/10.1088/0953-4075/43/20/202001>.
- [88] K. Martin, “Compact optical frequency standards for future applications beyond the laboratory,” Ph.D. dissertation, University of New Mexico, 2019.
- [89] P. Barakhshan, A. Marrs, A. Bhosale, B. Arora, R. Eigenmann, and M. S. Safronova, *Portal for High-Precision Atomic Data and Computation* (version 2.0). University of Delaware, Newark, DE, USA. URL: <https://www.udel.edu/atom> [February 2022].
- [90] M. Xue, C. Gao, L. Niu, S. Zhu, and C. Sun, “Influence of amplified spontaneous emission on laser linewidth in a fiber amplifier,” *Appl. Opt.*, vol. 59, no. 8, pp. 2610–2614, Mar. 2020. DOI: [10.1364/AO.383507](https://doi.org/10.1364/AO.383507). [Online]. Available: <https://opg.optica.org/ao/abstract.cfm?URI=ao-59-8-2610>.
- [91] D. Strickland and G. Mourou, “Compression of amplified chirped optical pulses,” *Optics Communications*, vol. 56, no. 3, pp. 219–221, 1985, ISSN: 0030-4018. DOI: [https://doi.org/10.1016/0030-4018\(85\)90120-8](https://doi.org/10.1016/0030-4018(85)90120-8). [Online]. Available: <https://www.sciencedirect.com/science/article/pii/0030401885901208>.
- [92] U. Keller, *Ultrafast Lasers*. Springer, 2021.
- [93] W. Demtröder, *Laser Spectroscopy Vol. 1: Basic Principles*, 4th ed. Springer, 2008.
- [94] V. Maurice *et al.*, “Miniaturized optical frequency reference for next-generation portable optical clocks,” *Opt. Express*, vol. 28, no. 17, pp. 24 708–24 720, Aug. 2020. DOI: [10.1364/OE.396296](https://doi.org/10.1364/OE.396296). [Online]. Available: <https://opg.optica.org/oe/abstract.cfm?URI=oe-28-17-24708>.
- [95] A. Hati *et al.*, “Ultra-low-noise regenerative frequency divider for high-spectral-purity rf signal generation,” in *2012 IEEE International Frequency Control Symposium Proceedings*, 2012, pp. 1–4. DOI: [10.1109/FCS.2012.6243683](https://doi.org/10.1109/FCS.2012.6243683).
- [96] R. W. P. Drever *et al.*, “Laser phase and frequency stabilization using an optical resonator,” *Applied Physics B*, vol. 31, pp. 97–105, 2 1983. DOI: [10.1007/BF00702605](https://doi.org/10.1007/BF00702605).

- [97] S. Schilt *et al.*, “Frequency discriminators for the characterization of narrow-spectrum heterodyne beat signals: Application to the measurement of a sub-hertz carrier-envelope-offset beat in an optical frequency comb,” *Review of Scientific Instruments*, vol. 82, no. 12, p. 123 116, Dec. 2011, ISSN: 0034-6748. DOI: [10.1063/1.3670357](https://doi.org/10.1063/1.3670357). eprint: [https://pubs.aip.org/aip/rsi/article-pdf/doi/10.1063/1.3670357/15705065/123116\\_1\\_online.pdf](https://pubs.aip.org/aip/rsi/article-pdf/doi/10.1063/1.3670357/15705065/123116_1_online.pdf). [Online]. Available: <https://doi.org/10.1063/1.3670357>.
- [98] G. D. Domenico, S. Schilt, and P. Thomann, “Simple approach to the relation between laser frequency noise and laser line shape,” *Appl. Opt.*, vol. 49, no. 25, pp. 4801–4807, Sep. 2010. DOI: [10.1364/AO.49.004801](https://doi.org/10.1364/AO.49.004801). [Online]. Available: <https://opg.optica.org/ao/abstract.cfm?URI=ao-49-25-4801>.
- [99] W. Loh *et al.*, “Dual-microcavity narrow-linewidth brillouin laser,” *Optica*, vol. 2, no. 3, pp. 225–232, Mar. 2015. DOI: [10.1364/OPTICA.2.000225](https://doi.org/10.1364/OPTICA.2.000225). [Online]. Available: <https://opg.optica.org/optica/abstract.cfm?URI=optica-2-3-225>.
- [100] S. Gundavarapu *et al.*, “Sub-hertz fundamental linewidth photonic integrated brillouin laser,” *Nature Photonics*, vol. 13, pp. 60–67, 1 Jan. 2019. DOI: [10.1038/s41566-018-0313-2](https://doi.org/10.1038/s41566-018-0313-2). [Online]. Available: <https://doi.org/10.1038/s41566-018-0313-2>.
- [101] W. Loh, S. Yegnanarayanan, F. O’Donnell, and P. W. Juodawlkis, “Ultra-narrow linewidth brillouin laser with nanokelvin temperature self-referencing,” *Optica*, vol. 6, no. 2, pp. 152–159, Feb. 2019. DOI: [10.1364/OPTICA.6.000152](https://doi.org/10.1364/OPTICA.6.000152). [Online]. Available: <https://opg.optica.org/optica/abstract.cfm?URI=optica-6-2-152>.
- [102] G. Moille *et al.*, “Kerr-induced synchronization of a cavity soliton to an optical reference,” *Nature*, vol. 624, pp. 267–274, 7991 Dec. 2023. DOI: [10.1038/s41586-023-06730-0](https://doi.org/10.1038/s41586-023-06730-0).
- [103] V. Yudin *et al.*, “General methods for suppressing the light shift in atomic clocks using power modulation,” *Phys. Rev. Appl.*, vol. 14, p. 024 001, 2 Aug. 2020. DOI: [10.1103/PhysRevApplied.14.024001](https://doi.org/10.1103/PhysRevApplied.14.024001). [Online]. Available: <https://link.aps.org/doi/10.1103/PhysRevApplied.14.024001>.

- [104] I. Barmes, S. Witte, and K. S. E. Eikema, “High-precision spectroscopy with counter-propagating femtosecond pulses,” *Phys. Rev. Lett.*, vol. 111, p. 023 007, 2 Jul. 2013. DOI: [10.1103/PhysRevLett.111.023007](https://doi.org/10.1103/PhysRevLett.111.023007). [Online]. Available: <https://link.aps.org/doi/10.1103/PhysRevLett.111.023007>.
- [105] J. Wu, D. Hou, Z. Qin, Z. Zhang, and J. Zhao, “Observation of rb two-photon absorption directly excited by an erbium-fiber-laser-based optical frequency comb via spectral control,” *Phys. Rev. A*, vol. 89, p. 041 402, 4 Apr. 2014. DOI: [10.1103/PhysRevA.89.041402](https://doi.org/10.1103/PhysRevA.89.041402). [Online]. Available: <https://link.aps.org/doi/10.1103/PhysRevA.89.041402>.
- [106] G. Grynberg and B. Cagnac, “Doppler-free multiphotonic spectroscopy,” *Reports on Progress in Physics*, vol. 40, no. 7, p. 791, Jul. 1977. DOI: [10.1088/0034-4885/40/7/002](https://doi.org/10.1088/0034-4885/40/7/002). [Online]. Available: <https://dx.doi.org/10.1088/0034-4885/40/7/002>.
- [107] T. N. Nguyen and T. R. Schibli, “Temperature-shift-suppression scheme for two-photon two-color rubidium vapor clocks,” *Phys. Rev. A*, vol. 106, p. 053 104, 5 Nov. 2022. DOI: [10.1103/PhysRevA.106.053104](https://doi.org/10.1103/PhysRevA.106.053104). [Online]. Available: <https://link.aps.org/doi/10.1103/PhysRevA.106.053104>.